NAVAL POSTGRADUATE SCHOOL

MONTEREY, CALIFORNIA

THESIS

THE DESIGN, OPTIMIZATION, CONSTRUCTION, AND TESTING OF A KINOVA 7DOF ROBOTIC ARM FLOATING VEHICLE

by

Katherine J. Lupo

June 2023

Thesis Advisor: Jennifer Hudson
Second Reader: Marcello Romano

THIS PAGE INTENTIONALLY LEFT BLANK

REPORT DOCUMENTATION PAGE	*Form Approved OMB No. 0704-0188*

1. AGENCY USE ONLY *(Leave blank)*	**2. REPORT DATE** June 2023	**3. REPORT TYPE AND DATES COVERED** Master's thesis

4. TITLE AND SUBTITLE THE DESIGN, OPTIMIZATION, CONSTRUCTION, AND TESTING OF A KINOVA 7DOF ROBOTIC ARM FLOATING VEHICLE	**5. FUNDING NUMBERS**
6. AUTHOR(S) Katherine J. Lupo	
7. PERFORMING ORGANIZATION NAME(S) AND ADDRESS(ES) Naval Postgraduate School Monterey, CA 93943-5000	**8. PERFORMING ORGANIZATION REPORT NUMBER**
9. SPONSORING / MONITORING AGENCY NAME(S) AND ADDRESS(ES) N/A	**10. SPONSORING / MONITORING AGENCY REPORT NUMBER**

11. SUPPLEMENTARY NOTES The views expressed in this thesis are those of the author and do not reflect the official policy or position of the Department of Defense or the U.S. Government.

12a. DISTRIBUTION / AVAILABILITY STATEMENT Approved for public release. Distribution is unlimited.	**12b. DISTRIBUTION CODE** A

13. ABSTRACT (maximum 200 words)

As space exploration and technology continue to advance, there is an expanding interest in robotic on-orbit servicing (OOS) to conduct repairs, refueling, or debris removal of damaged spacecraft. The development of OOS relies on ground testing facilities as they simulate the conditions and dynamics of space in a controlled environment, useful for testing and validating new technologies and procedures. Given the significance of both ground testing facilities and the development of OOS technology, this thesis endeavors to design, optimize, and construct a floating spacecraft simulator (FSS) with an attached seven degrees of freedom robotic arm. A CAD model was used to create the final version of the FSS, which incorporated all hardware necessary for the power and subsystem control. This included the onboard computer, reaction wheel, thrusters, air bearings, and the robotic arm. The design was then constructed and an accompanying assembly guide and electronic schematic of the FSS system were formulated. During the functionality trial conducted on one of the NPS Space Robotics Laboratory granite tables, the final product successfully demonstrated its capability to operate the thruster, air bearings, and robotic arm operations.

14. SUBJECT TERMS floating vehicle, optimization, construction, robotic arm, CAD, 7 degrees of freedom	**15. NUMBER OF PAGES** 173
	16. PRICE CODE

17. SECURITY CLASSIFICATION OF REPORT Unclassified	**18. SECURITY CLASSIFICATION OF THIS PAGE** Unclassified	**19. SECURITY CLASSIFICATION OF ABSTRACT** Unclassified	**20. LIMITATION OF ABSTRACT** UU

NSN 7540-01-280-5500

Standard Form 298 (Rev. 2-89)
Prescribed by ANSI Std. 239-18

THIS PAGE INTENTIONALLY LEFT BLANK

Approved for public release. Distribution is unlimited.

THE DESIGN, OPTIMIZATION, CONSTRUCTION, AND TESTING OF A KINOVA 7DOF ROBOTIC ARM FLOATING VEHICLE

Katherine J. Lupo
Ensign, United States Navy
BS, United States Naval Academy, 2022

Submitted in partial fulfillment of the
requirements for the degree of

MASTER OF SCIENCE IN ASTRONAUTICAL ENGINEERING

from the

NAVAL POSTGRADUATE SCHOOL
June 2023

Approved by: Jennifer Hudson
Advisor

Marcello Romano
Second Reader

Brian S. Bingham
Chair, Department of Mechanical and Aerospace Engineering

THIS PAGE INTENTIONALLY LEFT BLANK

ABSTRACT

As space exploration and technology continue to advance, there is an expanding interest in robotic on-orbit servicing (OOS) to conduct repairs, refueling, or debris removal of damaged spacecraft. The development of OOS relies on ground testing facilities as they simulate the conditions and dynamics of space in a controlled environment, useful for testing and validating new technologies and procedures. Given the significance of both ground testing facilities and the development of OOS technology, this thesis endeavors to design, optimize, and construct a floating spacecraft simulator (FSS) with an attached seven degrees of freedom robotic arm. A CAD model was used to create the final version of the FSS, which incorporated all hardware necessary for the power and subsystem control. This included the onboard computer, reaction wheel, thrusters, air bearings, and the robotic arm. The design was then constructed and an accompanying assembly guide and electronic schematic of the FSS system were formulated. During the functionality trial conducted on one of the NPS Space Robotics Laboratory granite tables, the final product successfully demonstrated its capability to operate the thruster, air bearings, and robotic arm operations.

THIS PAGE INTENTIONALLY LEFT BLANK

Table of Contents

THIS PAGE INTENTIONALLY LEFT BLANK

List of Figures

List of Tables

THIS PAGE INTENTIONALLY LEFT BLANK

List of Acronyms and Abbreviations

ABF air bearing floor

ABV air-bearing vehicle

ARGOS Active Response Gravity Offload System

CAD computer-aided design

COG center of gravity

COM center of mass

CSA Canadian Space Agency

DARPA Defense Advanced Research Projects Agency

DoF degree of freedom

EAC European Astronaut Center

ERA European Robotics Arm

ESA European Space Agency

EVA Astronaut Extravehicular Activity

FRL Flight Robotics Laboratory

FSS Floating Spacecraft Simulator

GEO Geosynchronous Earth Orbit

GNC guidance, navigation, and control

HEO high Earth orbit

I2C inter-integrated circuit

ISS International Space Station

JEMEF Japanese Experiment Module Exposed Facility

JEMRMS Japanese Experiment Module Remote Manipulator System

JPL Jet Propulsion Laboratory

LEO low Earth orbit

MEO medium Earth orbit

MED momentum exchange devices

NASA National Aeronautics and Space Administration

NBF neutral buoyancy facilities

NBL Neutral Buoyancy Laboratory

NPS Naval Postgraduate School

OOS on-orbit servicing

ORBIT Orbital Robotics Bench for Integrated Technology

ORION Orbital Robotic Integration, On-Orbit servicing, and Navigation

OSAM-1 On-orbit Servicing, Assembly, and Manufacturing 1

RSGS Robotic Servicing of Geosynchronous Satellites

SDA serial data line

SCL serial clock line

SMBus system management bus

SRL Space Robotics Lab

SRMS Shuttle Remote Manipulator System

SPIDER Space Infrastructure Dexterous Robot

SSAG Space System Academic Group

SysML system model language

THIS PAGE INTENTIONALLY LEFT BLANK

Acknowledgments

I would first like to thank my thesis advisor, Dr. Jennifer Hudson, for her guidance and encouragement during this thesis process. I appreciate that you have taken time out of your already busy schedule to provide valuable feedback.

Thank you to Dr. Carson Vogt for his assistance with the endless material requests for this project. I applaud anyone who can successfully order anything though the government.

Thank you to the technicians in the Space Systems Academic Group laboratory, especially Ron Phelps, for your help developing the reaction wheel electronic hardware. Your assistance was greatly appreciated.

Thank you to my housemates, the “Ladies of Destruction," for the never-ending adventures—more soon to come.

Thank you to the sharks that did not eat me during my unsolicited drown-proofing practices (surfing) at Asilomar beach and Lover’s Point .

And finally, thank you to the space systems engineering cohort for their mentorship and endless jokes.

THIS PAGE INTENTIONALLY LEFT BLANK

CHAPTER 1:
Introduction

1.1 Research Motivation

Interest in space is expanding, whether it be space exploration, new space system technologies, or recent missions into space. Many are curious about discovering what secrets lay beyond our planet. This curiosity is simultaneously fueled and quenched by ongoing research of space—and to make progress in research, we must be constantly evolving old technologies or inventing new ideas. One such area in constant development is the idea of robotic on-orbit servicing (OOS).

Space is expensive, difficult for humans to reach, and has a distinct lack of resources at its disposal. In order to make headway in space exploration and technology, more focus must be put on future space systems, not worrying about past systems. Unfortunately, these past systems, often damaged and old satellites, provide vital information to future systems. Current OOS requires a large amount of dangerous human involvement in repair and refueling, assuming the system is close enough to Earth and chosen to be repaired at all. With the advancement in robotic OOS, the need for human involvement will be dismissed, saving time and money, while additionally extending the mission life of investments in space.

Because of the dangers and expenses of outer space, ground testing facilities are often used to replicate the conditions of space and provide a controlled environment for testing and validating new technologies and procedures related to satellite and spacecraft operations. These facilities play a critical role in the research and development of OOS. They enable researchers and engineers to simulate the harsh conditions of space and test various systems and equipment, such as robotic arms, propulsion systems, and communication devices, to ensure they can operate efficiently in space. By using ground testing facilities, researchers and engineers can conduct experiments and collect data that can be used to improve the performance and reliability of these critical missions. Ground testing facilities help identify and address potential issues before they occur in space, ultimately increasing the chances

of success for these missions.

1.2 Research Objectives

This research has five primary objectives, which will contribute to the development of Kinova 7 degree of freedom (DoF) Robotic Arm Floating Spacecraft Simulator (FSS).

1.2.1 Finalize and Optimize Design of a FSS

A partial computer-aided design (CAD) design of the FSS was provided by prior researchers. The design is to be improved and completed. The research seeks to determine how to optimize the design by exploring three distinct improvement options: lowering the center of mass (COM), upgrading the battery component, and refining the material of the structural components of the floating vehicle prototype. The electronic components tasked with controlling the thrusters, reaction wheel, and robotic arm also must be selected and explored to ensure the FSS is capable of being controlled remotely.

1.2.2 Assemble the FSS

The assembly of FSS will be constructed from the completed CAD model. The model will provide a better understanding of the electronic hardware and pneumatics implemented. Once the floating vehicle construction is completed, a Kinova 7 DoF Robotic Arm will be attached to the top of the vehicle, allowing the NPS Space Robotics Lab (SRL) to have its first FSS with a 7DoF robotic arm.

1.2.3 Create an Assembly Guide

There is currently no documentation on how to construct an FSS of this size, and how to incorporate a Kinova Robotic Arm. This process will be completed via reverse engineering the past FSS' construction guides to apply to a larger FSS. The guide will provide clear and concise instructions for each electronic hardware and pneumatic system, complete with pictures of each step.

1.2.4 Trial Functionality on NPS's POSEIDYN Testbed

After the robotic arm is mounted upon the FSS, the completed subsystems will be tested for performance. The air bearings and thrusters will be tested to ensure they can adequately support the weight of the FSS and offer frictionless motion. The robotic arm will be commanded into a variety of positions to ensure the FSS maneuvers as predicted by the control trajectory provided by ENS Mathew Tungett.

1.2.5 Future Work

Instructions and schematics will be provided for the next steps to make the FSS fully functional. Due to time constraints, not all electronic components were able to be received to deliver a complete and maneuverable FSS. The Jetson Nano has not been updated and has yet to be configured to be accessed wirelessly. The Python code to send and receive commands to the reaction wheel as well as the thrusters has yet to be implemented.

THIS PAGE INTENTIONALLY LEFT BLANK

CHAPTER 2:
Background

This chapter showcases a variety of spacecraft simulators with examples and uses of each. It also establishes the historical background of on-orbit servicing and robotic manipulators in space to provide a basic understanding of the importance of spacecraft simulators and the future of robotic on-orbit servicing.

2.1 Discussion of Kinematic and Dynamic Simulators

Spacecraft simulators are used to replicate motions in a spacecraft and are typically used for research, development, and testing. They can be split into two separate simulated motion types: kinematic and dynamic simulators. Kinematic simulators do not use the spacecraft's actuators intended for space flight. They utilize various forces and torques to impose translational and rotational motion on the spacecraft, from outside actuators [1]. Figure 2.1 shows a small kinematic simulator at the Orbital Robotic Integration, On-Orbit servicing, and Navigation (ORION) laboratory at Florida Institute of Technology. ORION includes a 6 DoF kinematic simulator that incorporates a 2 DoF motion table on a gantry, a 2 DoF pan-tilt mechanism to which the test vehicle can be mounted, and a second 2 DoF pan-lilt mechanism that is mounted on the gantry [2].

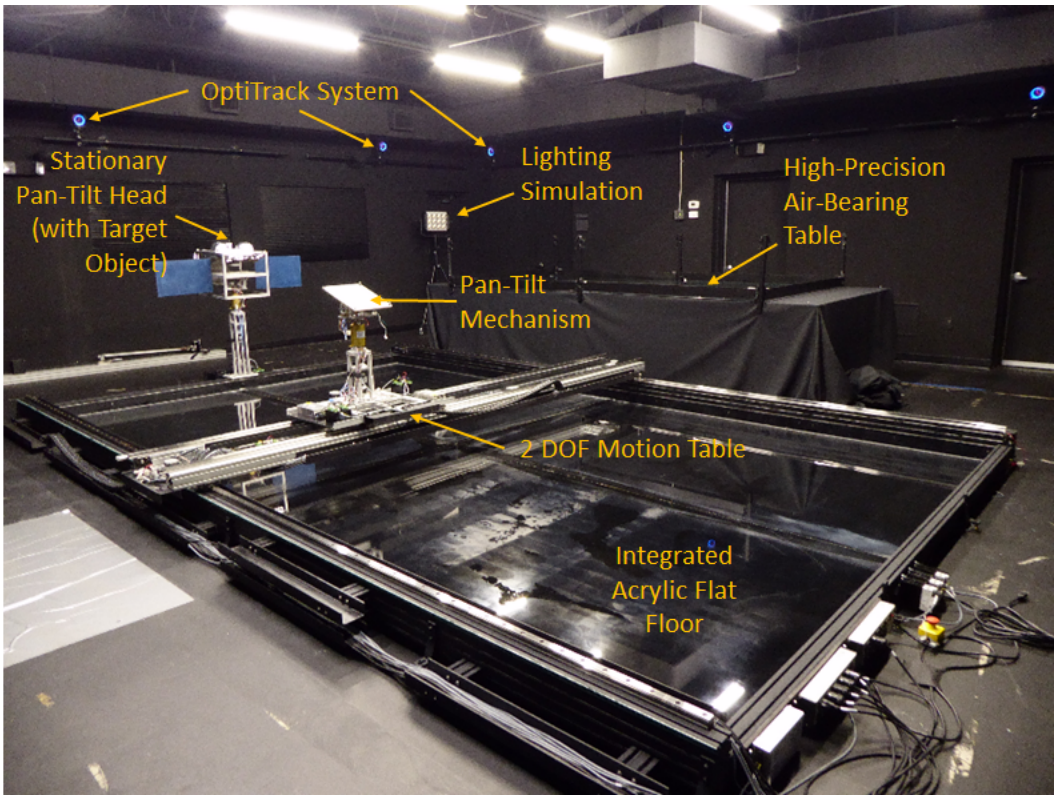

Figure 2.1. FIT'S ORION Laboratory with labeled elements. Source: [3].

Instead of the thrusters a spacecraft would normally maneuver with, the spacecraft can be mounted to the pan-lilt mechanism and could reproduce the 3D geometry of formation flight, fly around, and capture approaches [1]. Kinematic simulators are primarily employed to test sensor performance and navigation methods, and to train space mission crew members and operators of spacecraft [1]. Since kinematic simulators are prohibitively expensive and the goal of the thesis is to develop a system that can be used for research on spacecraft dynamics, a kinematic simulator was not suitable for this research project. Instead, this thesis focuses on the commercial-off-the-shelf–and therefore more economical–option: the dynamic simulator. As a result, most detail will be awarded to dynamic simulation.

A dynamic spacecraft simulator replicates the motion from forces and torques produced by the actuators used in real space flight [1]. The direct effects of gravity and ground-reaction forces on the vehicle must be negated by the use of a chosen method of suspension, to ensure the system simulates not only the kinematic aspects of motion but some of the dynamics

as well [1]. The simplest and most common solution to the spacecraft's suspension is the use of a cylindrical joint with an air bearing with a low-friction granite surface. Another popular solution is magnetic suspension. Freeing the system of gravity and ground reaction forces provides quasi free-friction rotation, unlike the kinematic simulator, and can be utilized to investigate other actuators' performances such as a reaction wheel. Dynamic simulators are primarily employed to test actuator performance and steering logic, test contact dynamics, verify models with multi-body systems (i.e., Robotic manipulators), evaluate docking and capture mechanism performance, and validate guidance, navigation, and control methods [4].

In order to separate the simulation vehicle's dynamics from relying on their surrounding environment and create negligible interaction, the vehicle must be controlled and powered by onboard sources. The motion must be managed by onboard computers and actuators, the power supplied by batteries on board, and the communication wireless [1]. This is required to reproduce the behavior of the vehicle in an actual space environment with no attachments or wire to anchor them to the ground [5]. The accessibility of the dynamic system depends on which of the five class systems are used in the development of the vehicle. These five classes are orbital microgravity, suborbital microgravity, neutral buoyancy, air bearing, and suspension systems [1].

An orbital microgravity system provides experimentation in 6 DoF propulsion and control in a pressurized orbital facility. 6 DoF includes three transitional and three rotational motions. The only system that exists in this class of dynamic simulation is aboard the International Space Station (ISS). The Astrobee robotic test facility, displayed in Figure 2.2, allows the free-flying small mass and diameter Astrobees to maneuver via electric fans throughout the interior of the ISS. The simulator provides low-risk, low-cost, long-term research; but, the amount of time scheduled for the astronaut crew is severely limited [6].

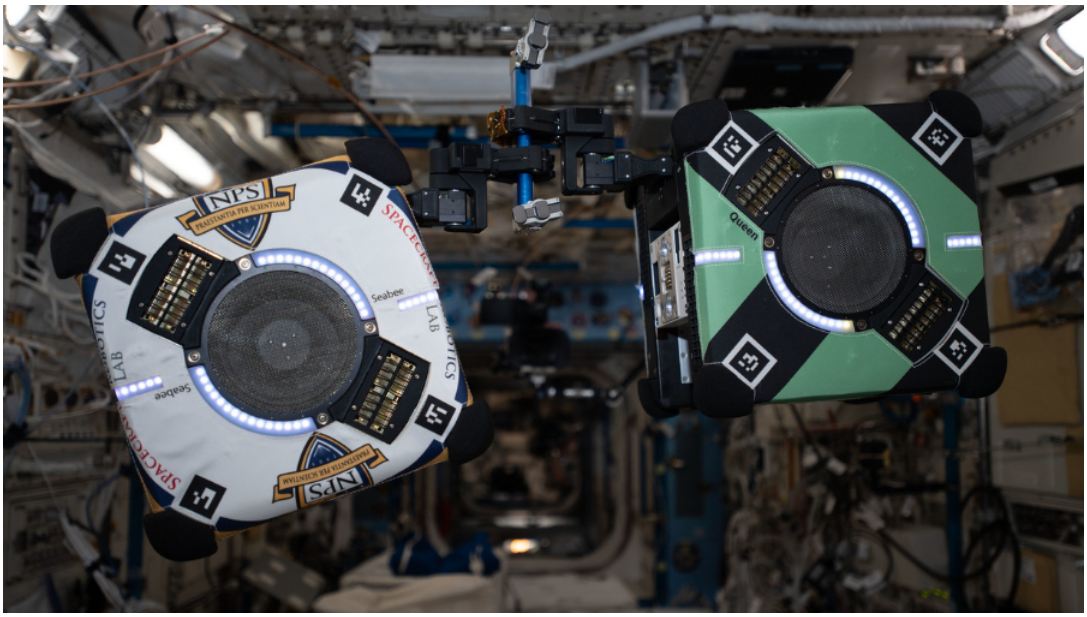

Figure 2.2. Two Astrobee robots performing flight maneuvers aboard the International Space Station. Source: [6].

The second class of dynamic simulators is a suborbital microgravity system. Suborbital systems encompass spaceflight in which a vehicle appear to be weightless, but its trajectory does not free itself from the atmosphere and gravitating body from which it was originated. The system simulates 6 DoF and is limited to a few minutes of active testing. Three types of suborbital microgravity systems exist: sounding rockets, drop towers, and parabolic flights [1]. Sounding rockets are experimental payload-carrying rockets launched in a sub-orbital trajectory. After the launch and the engine cut-off in the final stage, the experiment experiences minutes of vacuum and microgravity. The extent of time spent in this phase depends on the apogee altitude of the rocket trajectory. After testing, the payload then returns via parachute where it is retrieved for further analysis. Due to vibrations, intense temperature changes, and impact from touchdown after testing, sounding rockets are not the preferred method of testing sensitive spacecraft systems. National Aeronautics and Space Administration (NASA) often uses this dynamic simulation to test attitude control systems, robotics, and deployment mechanisms. Additionally, the low mission cost and short time span make this method a great tool for students to conduct high-quality research [7]. An image of a sounding rocket launch is provided in Figure **??**.

Figure 2.3. NASA sounding rocket program launch from the Wallops Flight Facility. Source: [7].

Drop towers, or drop shafts, are the next type of suborbital microgravity system simulators. Experiments are dropped from a tall structure to experience near-weightlessness before a cushioned landing. The European Space Agency (ESA) uses the Zarm drop tower in Bremen, Germany to conduct testing for space robotic systems. The tower's drop tube is separated from the outer structure, freeing experiments from external vibrations. Air drag in the drop tube is also reduced by evacuating the inside air. Zarm delivers 110 meters of free fall and 4.74 seconds of weightlessness [8]. A look into the interior of the Zarm drop tower is provided in Figure 2.4.

Figure 2.4. Interior of the ECA's Zarm drop tower in Bremen, GER. Source: [8].

Parabolic flights reproduce microgravity by flying in alternating arcs in an aircraft. Space and commercial agencies across the world, including NASA and the ESA, offer these flight campaigns. A glance into an ECA flight is provided in Figure 2.5. The time spent in microgravity for each flown parabola is roughly 20 seconds, repeated in multiple cycles for minutes of reduced gravity for each flight. Lunar and Martian gravity can be also simulated by adjusting the attack angle on the aircraft. Experiments aboard parabolic flights allow for hands-on tests with researchers in the aircraft with the payload; however, the experimental system cannot be modified on the scene due to safety concerns [9]. Parabolic flights can be used as a stepping stone for space systems to be tested in weightlessness before being exposed to the rigorous environment of space.

Figure 2.5. Interior view of the ESA's Zero-G A300 Airbus during parabolic flight. Source: [9].

neutral buoyancy facilities (NBF) are the next class of dynamic simulators. They consist of deep-water tanks often large enough to fit whole spacecraft and space station models for simulation in a microgravity situation [1]. NBFs offer 6 DoF, but they are imperfect simulators due to the dynamic exchange between the objects and the surrounding water [1]. The buoyancy properties of each submerged object limit the degrees of freedom and rotational motion. NBF simulations are also limited to the size of the tank and can become increasingly complex as the vehicles and objects must be designed to be water submersible. Water must not damage any of the mechanical systems, underwater propulsion, and navigation systems are required, and the buoyancy properties must be well defined [1]. Due to the number of modifications required for objects to be tested underwater, NBFs are not as common as other dynamic simulators, but they still have important uses.

NBFs are most commonly used to train astronauts for human space flights and test space robotic systems. NASA operates the most famous NBF, the Neutral Buoyancy Laboratory (NBL) at the Johnson Space Center in Houston, Texas (Figure 2.6). The ESA also has one of its own in Cologne, Germany at the European Astronaut Center (EAC). These respective facilities are largely used for space flight training [10]. The University of Maryland Space Systems Laboratory uses its buoyancy tank for space robotic systems. It has been leading the way in space robotic ingenuity to be tested in NBFs. Its most recent research in 2021

has been in the design and development of a roving vehicle for the Artemis missions [11].

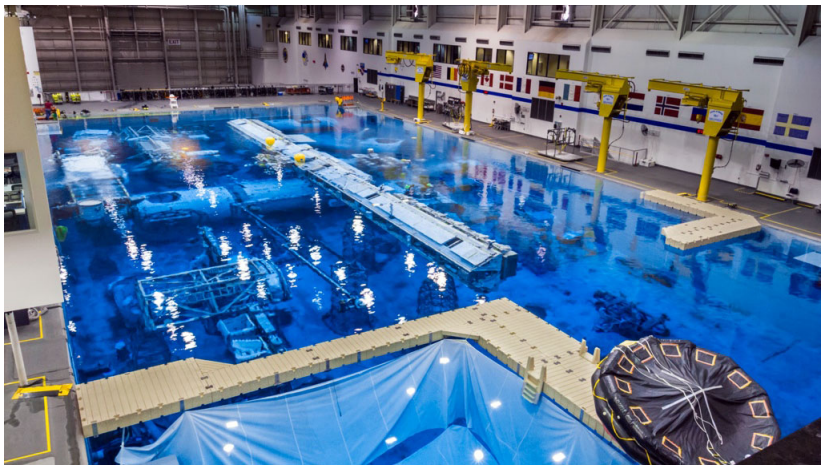

Figure 2.6. . Overhead view of the life-size mock-up of the ISS in NASA's Neutral Buoyancy Laboratory. Source: [12].

Of all dynamic simulator types, air-bearing systems are the most utilized. They are employed for spacecraft flight dynamics and control research such as autonomous rendezvous, capture, and self-assembly. Air-bearing systems consist of a flat floor or table that uses air-bearings on the testing vehicle, or air-bearing vehicle (ABV), to provide 3 DoF, two transitional and one rotational. The air bearings on the vehicle create a very thin layer of gas between the ABV and the flat surface that eliminates the friction between the two. The ABVs can then float similarly to spacecraft with the help of cold-gas thrusters and momentum exchange devices (MED). The flat surfaces often range from $\pm 3\mu$m to $\pm 46\mu$m, with the material usually consisting of epoxy, granite, or glass [1]. The air bearing system's surface must be as flat as possible, as any small indentation can affect the motion of the ABV and therefore the quality of the simulation. Two sub-divisions of air-bearing table systems currently exist: passive and active floor/table systems.

Passive floor air bearing systems consist of vehicle-supplied air bearings acting on the table. For larger dimensioned floors, epoxy is used due to its ease of construction. NASA houses two large epoxy air bearing floors, the air bearing floor (ABF) at Johnson Space Center and the Flight Robotics Laboratory Flight Robotics Laboratory (FRL) at Marshall Space Flight Center [4]. The ESA also operates its own at the Orbital Robotics Bench for Integrated Technology (ORBIT), pictured in Figure 2.7. These test beds are accessible enough that

many universities carry them for their use, but one drawback is that the epoxy can easily be marked and create inconsistencies in the flatness [4].

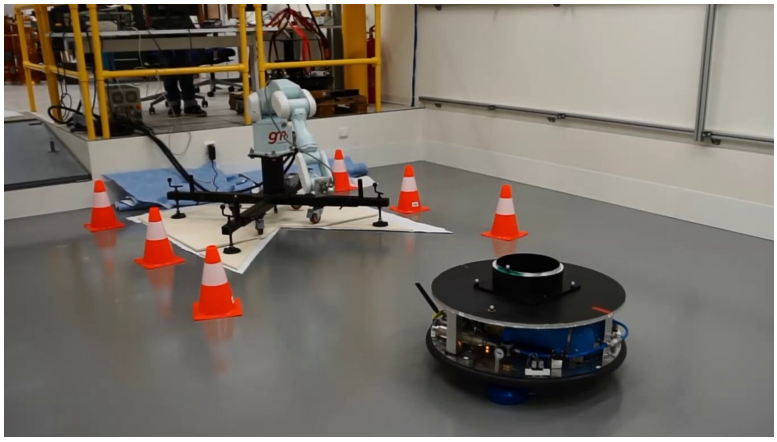

Figure 2.7. The ORBIT Laboratory at ESA's ESTEC technical center in the Netherlands. Source: [13].

Granite is a more accurate but increasingly expensive table material. Granite tables can be smoothed to a flatter surface but are limited by the extent of a team's budget. In addition to the expense of the granite block, the cost of transportation and installation is high because the granite can weigh many tons. The Gravity Offset Table at the Naval Research Laboratory in Washington, DC, is one such example, having an area of 6.1m x 7.3m and a mass of 34,000 kg [1]. Other granite tables include the TEAMS formation flying testbed at the German Aerospace Center (DLR) in Bremen, Germany, and the Robotic Manipulator System Testbed at the Shenzhen Space Technology Development Center (SSTC) in China [1]. The Naval Postgraduate School houses its table in the Spacecraft Robotic Laboratory: the POSEIDYN Floating Spacecraft Simulator test bed, pictured in Figure 2.8. This air-bearing table measures 4mx4mx0.3m, with a mass of 15,2000 kg [1].

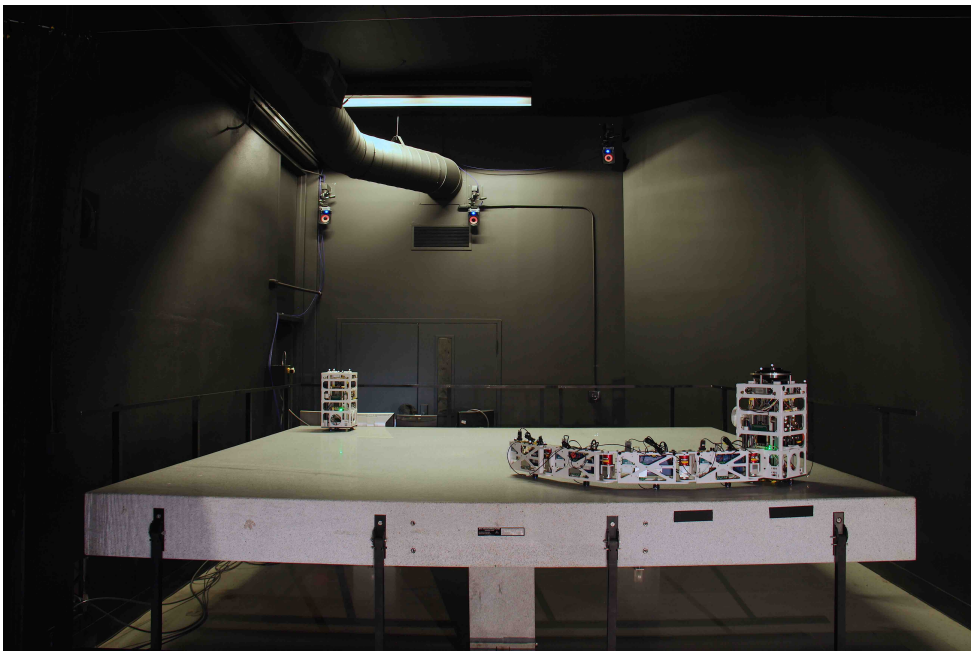

Figure 2.8. NPS's POSEIDYN Floating Spacecraft Simulator test bed in Monterey, CA. Source: [14].

A third type of air-bearing table utilizes a glass surface. Optical benches are usually paired with these glass-top tables to control the platform's vibration. Like granite tables, glass tables are limited to the size of a single glass piece, but it is possible to create larger tables out of multiple glass pieces. But, smoothing the transition between glass pieces has proven to be challenging. The largest glass air bearing table is currently the Formation Control Testbed (FTC) in the Jet Propulsion Laboratory (JPL) at Pasadena, California, with an area of 254 m^2 [15].

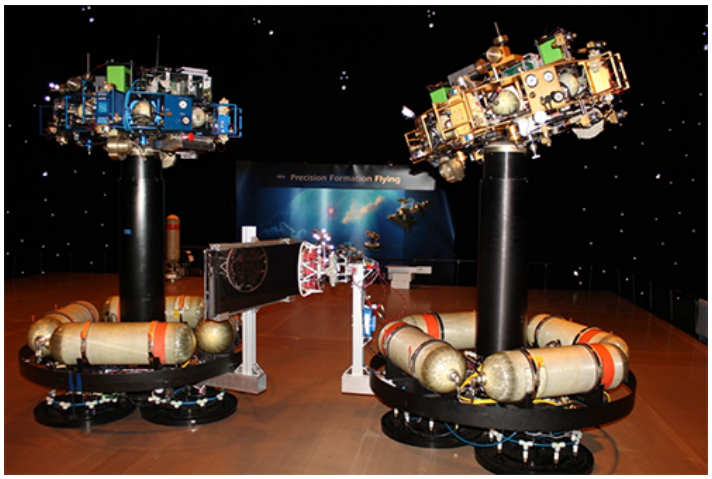

Figure 2.9. The Formation Control Testbed (or "Robodome") at the JPL. Source: [15].

Active table systems reverse the task of supplying the air between the floor and the vehicle. Instead of the vehicles requiring air bearings, the table generates the air film through porous carbon strips. One such table is the Falcon Air-Bearing test bed at Surrey Space Center in the UK [16].

The last type of dynamic simulator to be discussed is suspension systems. They support the vehicle's joints and appendage so that the force on the said components is zero, and the actuators are also not providing torques and forces [1]. By doing this, any external force on the system will cause the vehicles to move just as they would in the microgravity conditions of space. Active, passive, and hybrid suspension systems exist to create this force equilibrium on the vehicles appendages. Passive systems utilize pulleys, springs, and counterweights to counter the vehicle's mass [1]. Active systems utilize motors to supply the counterbalance forces, which allows the suspension system to reproduce simulations for varying masses, gravity conditions, and object motions. Hybrid systems employ motors to refine both the stability of the passive counterbalance system and the adaptability of the active systems. Suspension systems are typically used to test space robotics systems; namely, maneuver and capture simulations. One such example of an active suspension system is NASA's Active Response Gravity Offload System (ARGOS) at the Johnson Space Center, pictured in Figure 2.10 [17].

Figure 2.10. An engineer testing an astronaut suit using ARGOS. Source: [17].

2.2 Discussion of On-Orbit Servicing

One of the many applications of dynamic simulators is their use to simulate spacecraft OOS. OOS requires one orbiting spacecraft to move in extreme proximity to another and is historically difficult to both replicate in simulation, and perform in actuality. There consists of three reasons behind this difficulty: the first reason being all servicing requires the spacecraft to operate in close proximity to each other in an accelerated reference frame. This causes the centers of mass of the bodies to undergo relative trajectories that are different than typical trajectories in a uniform gravity field. Another reason is the maneuvers occur in quasi free-friction space, causing the movement of the objects to be primarily influenced by their inertia, in all 6 DoF. Any small force or torque on the objects will create movement. The last reason is that the lighting conditions of space consist of the intense disparity between shadow and light. It is difficult to recreate these lighting conditions in computer simulations. The guidance, navigation, and control (GNC) architecture must be carefully designed with space's lighting conditions in mind, as well as any actuators and sensors to

ensure the spacecraft can operate effectively [1]. OOS may be difficult to perform, but its benefits outweigh its drawbacks.

Successful OOS can provide benefits such as extended lifetimes for satellites and space stations, and in the case of robotic OOS, replace the astronaut manpower traditionally needed to build or make repairs. These replacements would reduce the budget and time allotted for repairing past missions, allowing for resources to be placed toward future missions in the exploration of space. Past OOS missions include rendezvous, berthing, space station assembly, formation flight, and capturing. Until 2007, all notable missions have been completed in low Earth orbit (LEO) by Astronaut Extravehicular Activity (EVA)s. Since these EVAs are restricted to LEO, any satellites operating in medium Earth orbit (MEO), Geosynchronous Earth Orbit (GEO), and high Earth orbit (HEO) are not accessible for replenishment or repair [18]. This is all subject to change with further application of robotic manipulators. Some of the future missions hope to include space debris removal, telescope assembly, robotic exploration of asteroids, and assist in the exploration of Mars [1].

2.3 Discussion on Robotic Manipulators

As our planet continues to advance in space technologies and explore the space domain, it is becoming more apparent that the solution to OOS is space robotic arms. The first ever robotic arm in space was the Shuttle Remote Manipulator System (SRMS), better known as the "Canadarm", in 1981 [19]. Developed by the Canadian Space Agency (CSA) for NASA space shuttle flights, Canadarm served its use until 2011 when NASA grounded its space shuttle flights. CSA has long been a significant contributor to space robotics and has dedicated space robotics as a great percentage of their contribution to the ISS [20]. The Canadarm established the feasibility of robotic arms in space and proved their usefulness for space operations. Canadarm 2, established in 2001, is currently operational and has taken over as the U.S. side of the ISS's primary robotic arm for assembly and operations. A visualization is provided in Figure 2.11.

Figure 2.11. Canadaarm 2 attached outside the ISS. Source: [20].

Other robotic manipulators currently in space worth noting include the Japanese Experiment Module Remote Manipulator System (JEMRMS) and the European Robotics Arm (ERA). JEMRMS is a 6 DoF robotic manipulator attached to the Japanese Experiment Module Exposed Facility (JEMEF) of the ISS in 2008. It consists of an 11-meter main arm and a 4-meter small fine arm intended for finer servicing in microgravity experiments [21].

The ERA is a "compass-shaped" 7 DoF robotic manipulator of length 11.3 meters built for use on the Russian segment of the ISS (see Figure 2.12). It has the ability to anchor, move forward and back by itself, and move hand-over-hand between fixed points—the first robot on the ISS to "walk" around. The ERA was launched and attached to the ISS in July 2021 [22]. The arm can be operated by the crew from both inside and outside the ISS, but also is fully programmable to be autonomous. Current missions include installing, removing, transferring, and replacing experiment payloads in and out through the Russian airlock, as well as transporting cosmonauts from one external working site to another [22].

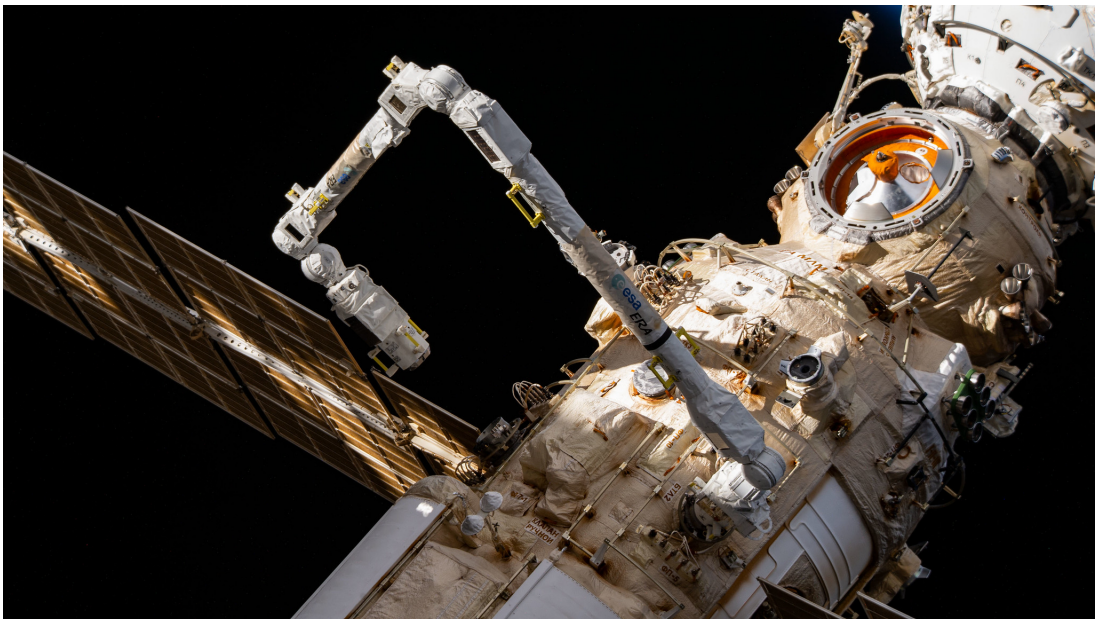

Figure 2.12. The ERA operating on the Russian side of the ISS. Source: [22].

Since the initial establishment of the first robotic arm in space, the Canadarm, robotic arms have increased their usefulness by demonstrating they can be attached to floating vehicles. One such example is NASA and the Defense Advanced Research Projects Agency (DARPA)'s Orbital Express program. Orbital Express consisted of a base spacecraft mounted with a 6 DoF robotic arm. It launched in 2007 to rendezvous with an on-orbit satellite to repair batteries and supply propellant [23]. The successful Orbital Express program proved that robotic arm manipulation attached to a floating base was possible.

A more recent development by NASA hopes to take the Orbital Express' mission a step further. On-orbit Servicing, Assembly, and Manufacturing 1 (OSAM-1) is NASA's newest spacecraft designed for not only OOS, but to deploy a separate payload called Space Infrastructure Dexterous Robot (SPIDER) to demonstrate in-space assembly by building a communications antenna. The program was initialized under the name Restore-L in 2016 with its only mission to refuel Landsat 7 with hydrazine fuel, but in 2020, it was reorganized to add the SPIDER payload and renamed OSAM-1 [24]. A digital portrayal of OSAM-1 repairing Landsat 7 can be found in Figure 2.13.

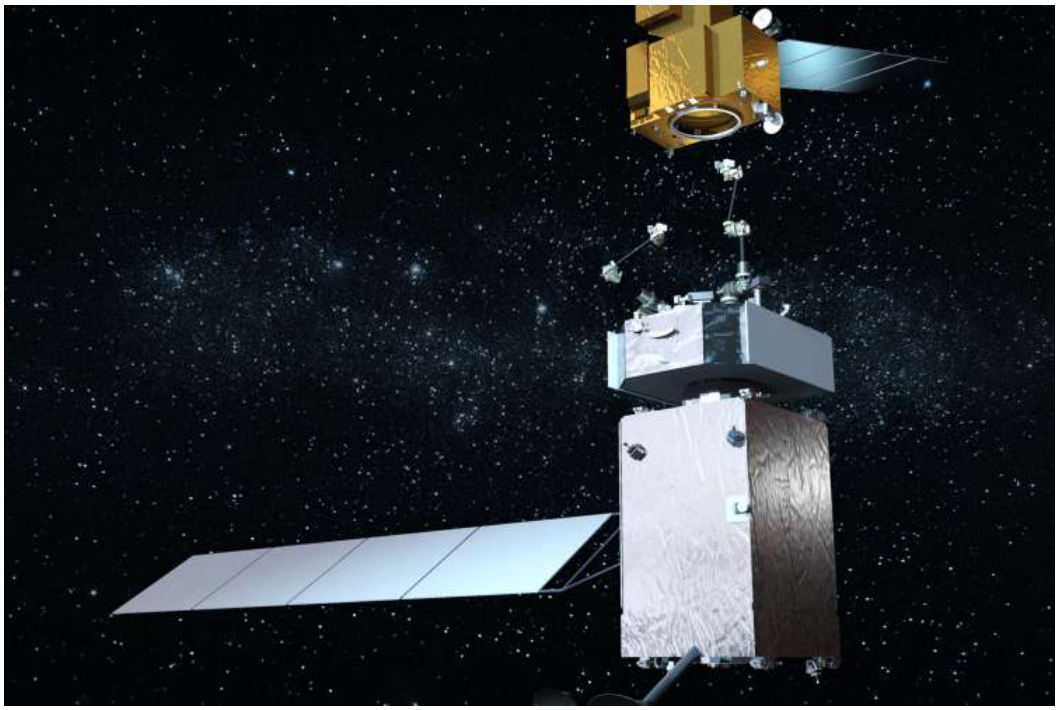

Figure 2.13. Digital representation of OSAM-1 repairing Landsat 7. Source: [25].

OSAM-1 currently consists of a spacecraft bus, which includes two robotic arms to grapple the target satellite, the servicing payload with 16 subsystems, and the SPIDER payload. The project has completed its critical design review of March 2022 and is currently undergoing manufacturing. OSAM-1 will be prepared for launch no earlier than 2025 [25].

While OSAM-1 is primarily focused on assembling a payload in space, DARPA's new Robotic Servicing of Geosynchronous Satellites (RSGS) program aims to enable the inspection and repair of satellites in GEO orbit. The RSGS robotics payload will consist of two robotic arms, checkout and calibration equipment, avionics boxes capable of executing robotics control flight software, cameras, and various robotic tools to assist in operating on malfunctioning satellites. The robotic payload testing is nearly finished, and on track for the program's scheduled to launch in 2024 [26].

CHAPTER 3:
Initial Design

A FSS with with a 7DoF robotic arm attached is a valuable tool for ground testing in OOS. Developing and testing the technology for OOS is crucial for extending the life of existing satellites, reducing the cost, and enabling future missions. The FSS can simulate microgravity conditions, allowing researchers to test the performance and reliability of on-orbit servicing equipment in a controlled environment before applying the technology in space.

The program used to make the 3D design of the FSS was Siemens NX [27]. All the components were initially created separately in part files and then uploaded to an assembly part file to fit together. All part dimensions are accurately represented in the model. A screen capture of the initial model is found in Figure 3.1.

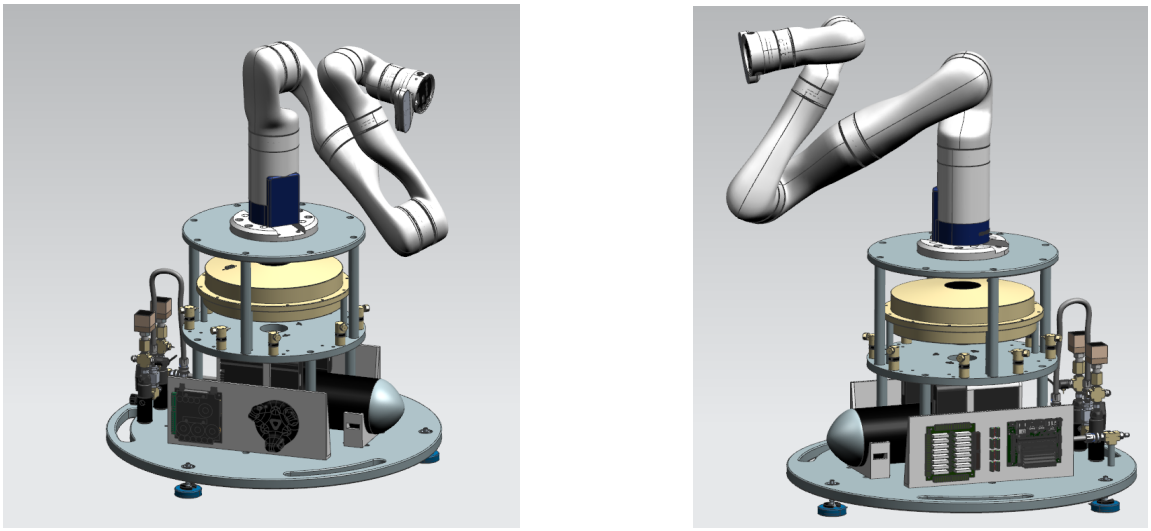

(a) FSS front view. (b) FSS back view.

Figure 3.1. Views of the Initial CAD Model in NX.

Table 5.1 presents the following major components in the initial NX model in no particular order.

Table 3.1. Major Components included in Initial CAD model

Component Name	Number Used
Reaction Wheel	1
NVIDIA Jetson Nano	1
Gem Sensors' Solenoid values	8
50mm Flat Air bearings	3
Inspired Energy "N" Series NH3054HD34	4
Industrial PC/104 Relay Board	1
Fatty Stabilizer CO2 Air Pneumatic Regulator	2
Ninja Ultralite Adjustable Tank Regulator – 4500 PSI	1
Ashcroft GC31 Ultra-Compact Digital Pressure Sensor	2
Kinova Robotic Arm Gen3	1
HTC VIVE Virtual Reality System Tracker 2018	1
TRI-M HPS3524 PC/104 Power Supply Unit	1
Air Nozzles (Custom)	8
Ninja SL2 4500 psi/45cu Air Tank	1

To visualize how the preliminary FSS operates, a proposed block diagram consisting of the pneumatic system that powers the air bearings and thrusters is presented, as well as an electronic system block diagram that shows how the battery, Jetson Nano, and other major electronic components pass data and power. Figure 3.2 displays the pneumatic schematic of the initial design.

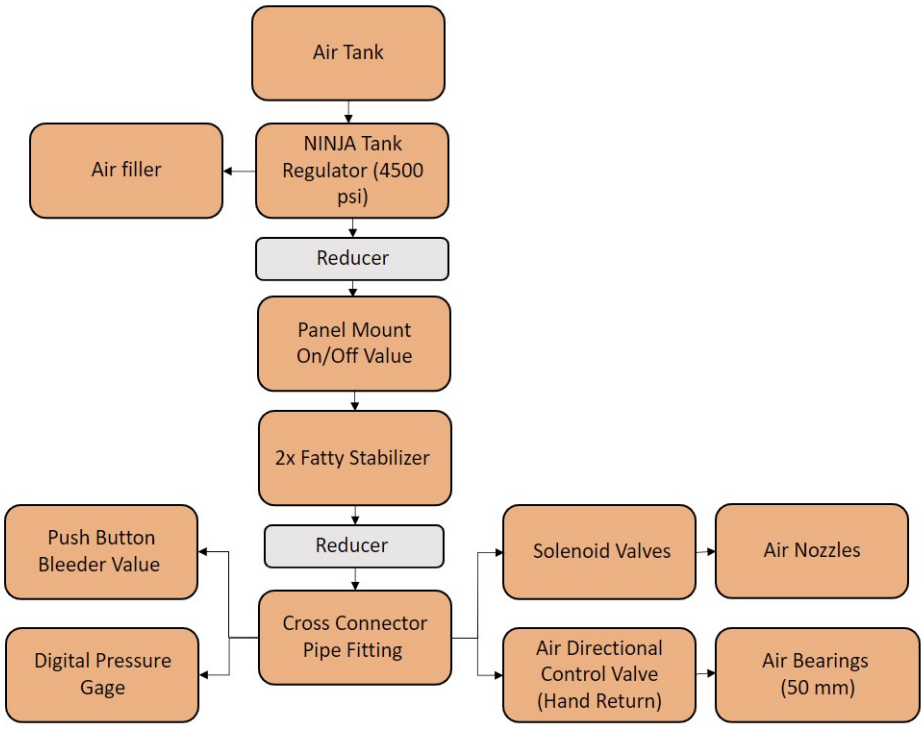

Figure 3.2. Proposed FSS Pneumatic Schematic

Figure 3.3 displays the proposed electronic schematic of the FSS.

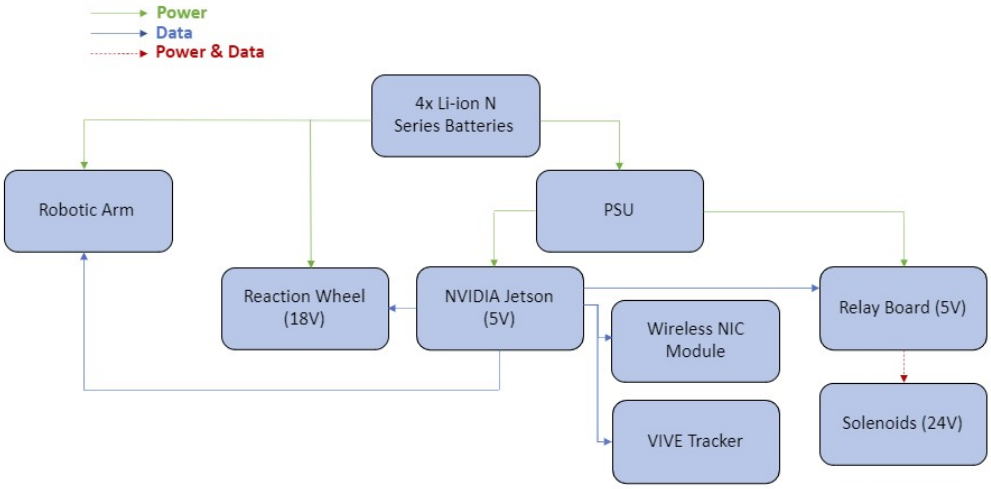

Figure 3.3. Proposed FSS Electrical Schematic

There are a variety of issues that arose up-front within the initial FSS design, particularly in the electrical schematic. One of the primary issues was the "N" series batteries which each provide 14.4 V. They do not provide nearly enough voltage to power both the robotic arm and the reaction wheel, and therefore, a new battery was in need of selection. An introduction of a new battery will require the voltage regulation of each of the primary components to be re-evaluated.

In addition, there was a lack of hardware for controlling the reaction wheel. The wheel requires an analog signal input for control, but the NVIDIA Jetson Nano is only capable of providing a digital signal. Further research was required to develop a solution for the conversion of a digital signal into an analog signal.

CHAPTER 4:
Design Modifications

This chapter explores the modifications made the initial design of the FSS. The intention is to introduce, replace, or upgrade a variety of components to present a finalized design. An effort to shift the COM is also discussed to help manage the weight distribution of the FSS.

4.1 Component Selection

A majority of the components from the initial FSS design remain the same, but a few components were to ensure the FSS can function properly both electronically and pneumatically. Components were selected for this design by first identifying if the manufacturer of a component on the initial FSS had an applicable version. If not, an internet search was conducted to find the commercially available product. All components were added to an updated CAD assembly appropriately.

4.1.1 Battery Selection

The battery component of the design, while present in the initial CAD model, needed to be selected for the final design. A Lithium-ion (Li-ion) battery was the primary type of battery for consideration, as they are utilized for space applications. Li-ion batteries contain a high energy efficiency, energy density, and wide temperature operating range [28]. For the application to the FSS, a battery that is capable of fast charge, smart battery management, and easy installation is favorable to be comparable to an actual floating spacecraft. Table 4.1 contains the requirements from the FSS components to be connected to the battery. This table assisted in narrowing down battery options, as a voltage of at least 24 V and a minimum of 5A were required to support both the Kinova arm and the reaction wheel.

Table 4.1. Battery requirements of major components.

Item	**Voltage (V)**	**Current (A)**	**Power (W)**
Kinova Arm	24	1.5	36
Thrusters	24	0.1667	4
Reaction Wheel	18	5	16.5
Jetson Nano	5	2	10
Total Required	**24**	**5**	**36**

The battery selected was the Inspired Energy's PH2059HD34, a rechargeable smart Li-ion battery pack capable of supplying 28.8V [29]. The PH2059HD34 was also one of the few smaller-sized Li-ion batteries capable of fitting in between the middle and bottom metal plates of the FSS and satisfies the other components' requirements noted in Table 4.1. The battery fits within the NPS safety requirements.

All "P" series battery packs from Inspired Energy come with an EB429 ideal diode board. These directly connected diodes limit the flow of current to one direction, outward from the battery. This prevents any damage to both the Li-ion battery and any electronic component connected.

4.1.2 DC-DC Voltage Regulator

With the voltage provided by the battery source changing from 14.4V to 28.8V, the input voltage was simply too high for the 18V design limit of the reaction wheel. A step-down voltage regulator had to be introduced to lower the input voltage to a safe 18V for the reaction wheel. It was determined the chosen regulator would need to be a buck-switching regulator. A switching regulator is required over a linear regulator because the power dissipation of the wheel, a value of up to 80 watts, is too high of an output power capacity for most linear regulators to handle and would most likely cause overheating. Additionally, switching regulators provides higher output efficiency. They waste less power as heat dissipation results in longer battery life for the connected power source. The efficiency of a switching regulator is typically between 85–95%, while a linear regulator is 30–40% [30]. The use of a step-

down switching regulator in the application of an FSS is optimal to provide power to the reaction wheel for the longest period with limited battery power waste.

The chosen commercially bought DC-DC regulator was the ACEIRMC 300W Step Down Buck Converter with Adjustable DC 6–40V to 1.2–36 V. The regulator is capable of handling the 28.8V voltage input from the battery and the power dissipation requirements of both the connected Li-ion battery and the reaction wheel at 95% efficiency [31].

4.1.3 Reaction Wheel Shunt

When the reaction wheel accelerates to control the orientation of the FSS, it is eventually going to need to decelerate to return to its initial state. The motor reversal returns the energy stored in the rotating flywheel to the reaction wheel's power supply in a process called regeneration. Regeneration causes current to flow in the opposite direction and back to the power source which can damage the reaction wheel, power supply, and any equipment connected to the system. To prevent this damage, a load must be connected to the wheel to absorb all the regenerative energy in the form of a dummy load or other system assemblies [32]. The chosen way to deal with regeneration on the FSS is through a shunt attached to the switching DC regulator. The shunt works by clamping the battery's supply voltage to 18V and dissipating the stored energy as heat.

A shunt capable of dissipating up to 80 watts is deceptively hard to find available commercially. After hours of searching failed to provide a suitable shunt for this reaction wheel, the option to build one from scratch became the only option. With the help of the technicians in the Space System Academic Group (SSAG) Laboratory here at NPS, a shunt capable of dissipating 80 watts to heat was built to be connected to both the switching voltage regulator and the reaction wheel. The details will be provided in later chapters.

4.1.4 AD/DA Board

The reaction wheel is to be controlled with commands from a Jetson Nano device. But, one issue stands in the way of the nano being simply connected to the wheel to issue commands: the reaction wheel is an analog device, and the Jetson Nano is a digital device. An analog signal uses voltage or current that continuously varies over time to convey information, while a digital signal uses non-continuous binary digits, or bits, to convey information.

The two signals are not directly compatible and must be converted between each other to communicate. Since the Jetson Nano does not have an AD/DA function on its GPIO interface, a compatible board must be introduced to do just that. The selected analog-to-digital board was Waveshare's High-Precision AD/DA Expansion Board. The board provides an eight-channel 24-bit analog-to-digital conversion with a 30 ksps sampling rate, and a 2-channel 16-bit digital-to-analog conversion [33].

4.1.5 Air Bearing Selection

Supply issues prevented the use of New Way's 50mm flat round air bearings. The replacement was New Way's next size available, the flat round 65mm air bearings. The 65mm bearings still function within the limits of the FSS, but unfortunately not to the same ideal level as the 50mm. The FSS was provided with a 4500 psi, 45 cu (737.4 cm^3) air tank. The air tank supplies compressed air to the air bearings; each air bearing has a specific flow rate depending on the size. The flow rate and size of the air tank determine the float time; a longer float time is ideal. The float time calculations are provided in Table 4.2.

Table 4.2. Float time calculations based on air bearing size.

Air Bearing Size	**Flow (NLPM)**	**Input Pressure (MPa)**	**Flow (LPM)**	**Float Time (min)**
50	1.1	0.41	5.77e-3	127.64
65	1.4	0.41	7.35e-3	100.28

The ideal load of the air bearing is the approximate force on the bearing where it functions the best based on the amount of lift. The estimated total weight of the FSS is 900 N (202.3 lbf). Between three air bearings, approximately 300 N (67.43 lbf) is applied to each. The ideal loads for the 50mm and 65mm air bearings are 355 N (80 lbf) and 666 N (150 lbs), respectively [34]. The ideal load of the 50 mm air bearing exists closer to the load applied, so 50mm is preferable. But, due to supply chain issues, the 65mm air bearings are acceptable.

4.1.6 Digital Pressure Sensors

The digital pressure sensors attached to the pneumatic system were upgraded from Ashcroft GC31 Ultra-Compact Digital Pressure Sensor to the ProSense DPG1 digital pressure gauge. The DPG1 provides the same information as the previous option but at a higher accuracy at ±0.5% and is more readily available commercially [35].

4.1.7 Materials Selection

The material for the standoff rods and top, middle, and bottom plates of the FSS was selected for both strength and lightweight characteristics. The strength of the plate enables it to withstand the weight of the heavy reaction wheel and Kinova arm without vulnerability to bending. The FSS's structure's design prevents any unnecessary weight from preventing the air bearings from lifting the FSS off the granite table, as well to assist in its transportation.

The selected material of the standoff rods needed to support the top and middle plates was 6061-T651 Aluminum. The same material again was selected for the middle and top plates at a ½ inch thickness. A greater thickness for the bottom plate was desired to support the entirety of the FSS on top; T304 Stainless Steel at a ¾ inch thickness. Unfortunately, an ordering issue prevented the stainless steel from arriving within a reasonable amount of time, so the base plate will consist of the same material as the top and middle plates. The material and thickness of the bottom plate should not affect the overall functioning of the FSS.

Once all the different FSS components were determined, the material properties of the FSS assembly in NX needed to be assigned. Setting the materials of the various parts enables mass properties to be calculated by NX. For example, in an NX part file, the bottom metal plate was set to stainless steel, and the cross-connector pipe fittings were set to brass. Some pieces, such as the battery and relay board, are not fabricated from one consistent material. In this case, one single material to represent the whole non-homogeneous piece was selected. Usually, the material selected already makes up a great percentage of the part or provides a similar weight to the part. For example, the materials for lithium batteries and relay board were graphite and aluminum, respectively.

4.2 Weight Distribution

It can be assumed from the initial CAD model that the robotic arm will cause the vehicle to shift every time the arm is moved. However, the current Kinova arm features a seventh joint that is kinematically redundant and, thus, capable of complex configurations and operations [20]. Therefore, the arm must possess a more intricate control algorithm to handle the dynamic shift of the vehicle every time the arm moves. To further improve the CAD design and provide support in writing the control algorithm, efforts were made to limit the effect the robotic arm has on the rest of the vehicle.

The Cartesian coordinate system of the CAD assembly was originally in the center of the bottom plate. For ease of visualization and to simplify for future use in the FSS's control algorithm, the system's origin was shifted down to the same plane as the lowest part of the air bearings.

The original intent to stabilize the FSS was to shift the COM down further toward the bottom plate. The COM is the point at which the distribution of mass is equal in all directions. A term often associated with COM is center of gravity (COG)— the average location of the weight of an object. In a uniform gravitational field like the one that envelops the Earth, the COM is the same as the COM, and the terms are therefore synonymous. A body with a low COM in comparison to a higher one in this system brings the benefit of balance. When a force acts upon the body with a low COM, the system allows greater angular displacement within the bounds of the base support. The Kinova arm operating on top of the FSS will be the source of the movement shifting the floating system's stability. A low COM minimizes any negative stability shifting and will help prevent tipping over when the robotic arm picks up a heavy object.

After some dissection of the current FSS build within NX, it was determined the COM of the system could not be shifted further downwards from its current position. The bulk of the electronic and pneumatic systems are already mounted to the base, leaving the only main components on the middle platform to be the reaction wheel and the air thrusters. The reaction wheel, providing a large percentage of the mass of the system, could not be shifted down as there would be no room for the batteries and air tank. In addition, the placement of the reaction wheel is already optimal for correctional torque on the system. Its placement above the rest of the system allows the wheels to apply less amount of torque for a greater

reaction on the system, so the moments created by the Kinova arm are correctable without much power from the reaction wheel.

Utilizing NX's "Mass Property" tools after assigning all parts a material, the COM was calculated by the system, as shown in Figure 4.1. Note that this simulation was done without including the Kinova robotic arm. Other calculations are included in the figure for supplementation.

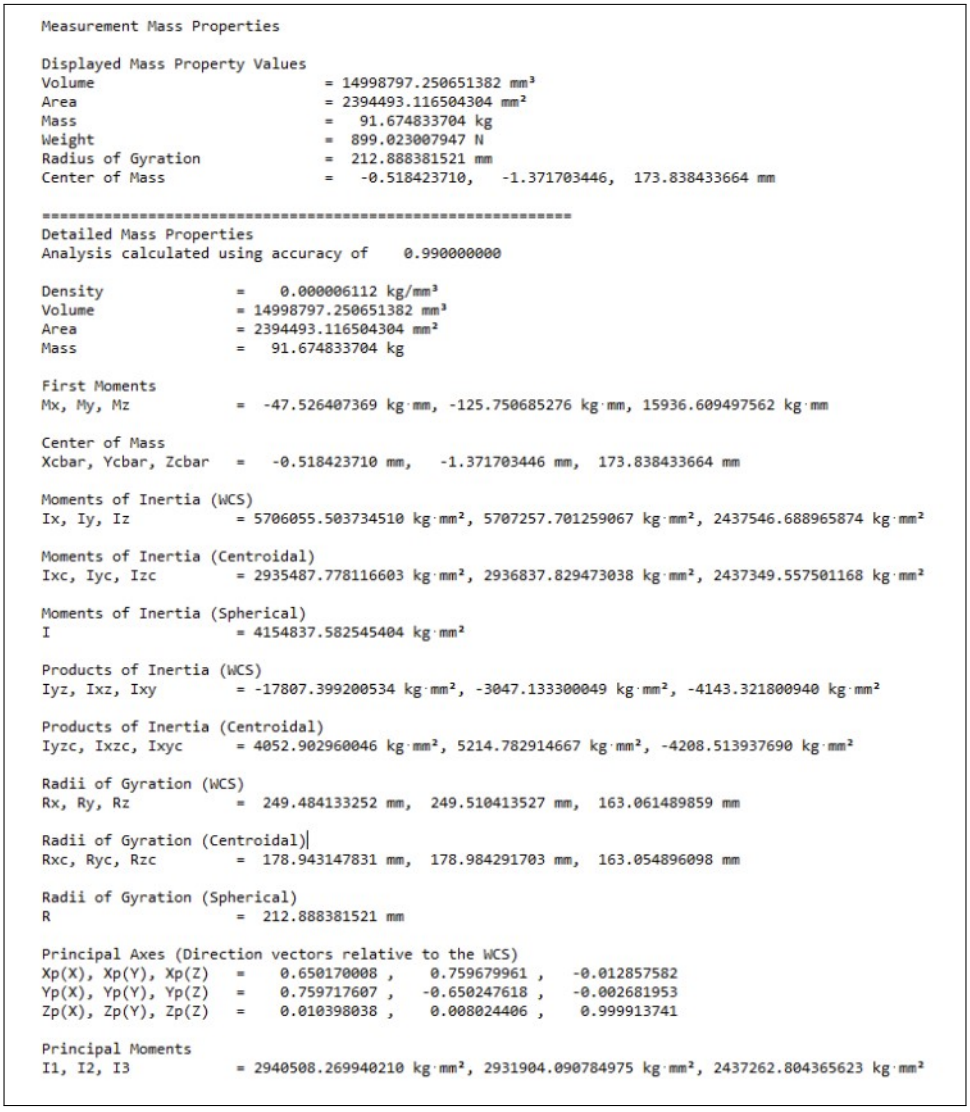

```
Measurement Mass Properties

Displayed Mass Property Values
Volume                          = 14998797.250651382 mm³
Area                            = 2394493.116504304 mm²
Mass                            =   91.674833704 kg
Weight                          =  899.023007947 N
Radius of Gyration              =  212.888381521 mm
Center of Mass                  =   -0.518423710,   -1.371703446,  173.838433664 mm

============================================================
Detailed Mass Properties
Analysis calculated using accuracy of    0.990000000

Density              =    0.000006112 kg/mm³
Volume               = 14998797.250651382 mm³
Area                 = 2394493.116504304 mm²
Mass                 =   91.674833704 kg

First Moments
Mx, My, Mz           =  -47.526407369 kg·mm, -125.750685276 kg·mm, 15936.609497562 kg·mm

Center of Mass
Xcbar, Ycbar, Zcbar  =   -0.518423710 mm,   -1.371703446 mm,  173.838433664 mm

Moments of Inertia (WCS)
Ix, Iy, Iz           = 5706055.503734510 kg·mm², 5707257.701259067 kg·mm², 2437546.688965874 kg·mm²

Moments of Inertia (Centroidal)
Ixc, Iyc, Izc        = 2935487.778116603 kg·mm², 2936837.829473038 kg·mm², 2437349.557501168 kg·mm²

Moments of Inertia (Spherical)
I                    = 4154837.582545404 kg·mm²

Products of Inertia (WCS)
Iyz, Ixz, Ixy        = -17807.399200534 kg·mm², -3047.133300049 kg·mm², -4143.321800940 kg·mm²

Products of Inertia (Centroidal)
Iyzc, Ixzc, Ixyc     = 4052.902960046 kg·mm², 5214.782914667 kg·mm², -4208.513937690 kg·mm²

Radii of Gyration (WCS)
Rx, Ry, Rz           =  249.484133252 mm,  249.510413527 mm,  163.061489859 mm

Radii of Gyration (Centroidal)
Rxc, Ryc, Rzc        =  178.943147831 mm,  178.984291703 mm,  163.054896098 mm

Radii of Gyration (Spherical)
R                    =  212.888381521 mm

Principal Axes (Direction vectors relative to the WCS)
Xp(X), Xp(Y), Xp(Z)  =    0.650170008 ,    0.759679961 ,   -0.012857582
Yp(X), Yp(Y), Yp(Z)  =    0.759717607 ,   -0.650247618 ,   -0.002681953
Zp(X), Zp(Y), Zp(Z)  =    0.010398038 ,    0.008024406 ,    0.999913741

Principal Moments
I1, I2, I3           = 2940508.269940210 kg·mm², 2931904.090784975 kg·mm², 2437262.804365623 kg·mm²
```

Figure 4.1. FSS mass properties generated by NX analysis.

The current calculated COM is not perfectly in the origin of the x and y axis, leaning more heavily in the +y direction due to part of the pneumatic system in front of the air tank.

While the COM could not be relocated, several edits were made to the FSS CAD assembly. Both side support walls were repositioned 20 mm outward. This provided more room for the wiring not present in the current CAD assembly. A collection of screw holes was additionally added to fasten segments. The holes to secure the air tank were extended, which allowed the tank to slide forward and back during construction. Holes were also added to secure the side supports, battery holders and standoffs for the middle and top plates.

All modifications and component edits where both integrated into the CAD design and applicably ordered for use in the construction of the FSS.

CHAPTER 5:
Final Design

The final design successfully incorporated the selected components and materials from the prior chapter. The CAD parts of the model were updated to reflect the components to be utilized in the build. The height of the FSS is 0.435 meters without the arm and has a bottom diameter of 0.303 meters. Due to its varying extendibility, the height calculations do not include the robotic arm. The total mass of the FSS, based on the final design in NX, is 101.2 kg (approximately 223.11 lb). The final CAD design for the FSS after all modifications are displayed in Figure 5.1 and 5.2. Though the model does not include any fasteners, electronic wiring, or pneumatic tubes, appropriate space has been allotted for those components.

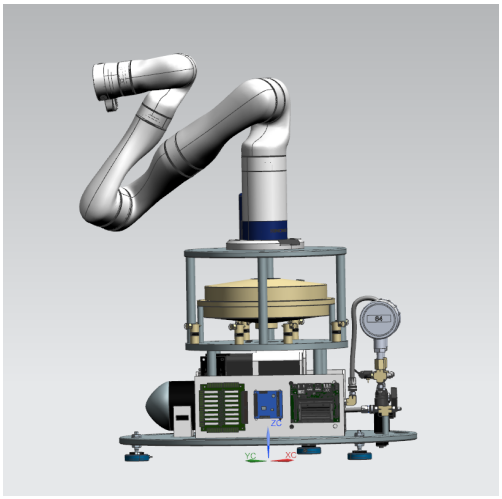

(a) FSS left view.

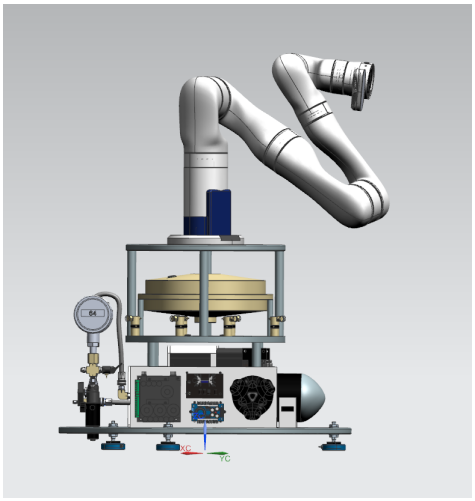

(b) FSS right view.

Figure 5.1. F

Left and right views of the final CAD model in NX.

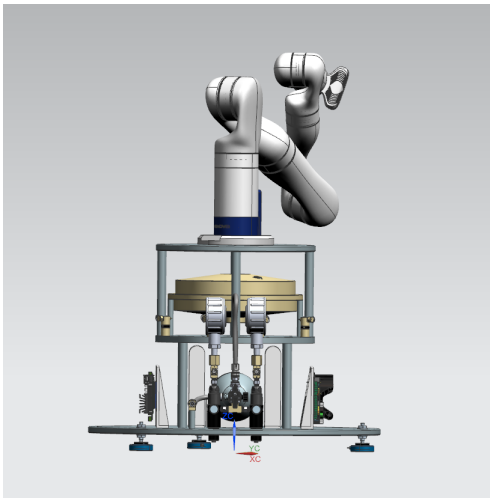

(a) FSS front view.

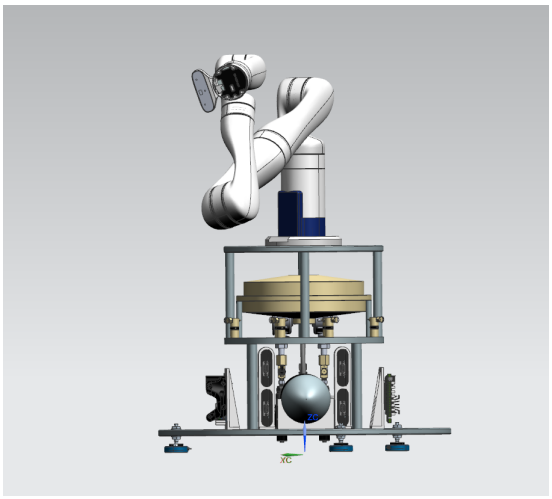

(b) FSS back view.

Figure 5.2. Front and back views of the final CAD model in NX.

Table 5.1. Major Components included in Final CAD model

Component Name	Number Used
Reaction Wheel	1
NVIDIA Jetson Nano	1
Gem Sensors' Solenoid values	8
65mm Flat Air bearings	3
Inspired Energy PH2059HD34 Battery	4
TRI-M IR104 PC/104 Industrial Relay Board	1
Fatty Stabilizer CO2 Air Pneumatic Regulator	2
Ninja Ultralite Adjustable Tank Regulator – 4500 PSI	1
Kinova Robotic Arm Gen3	1
HTC VIVE Virtual Reality System Tracker 2018	1
EB429 Ideal Diode Board for Inspired Energy "P" Series Battery Packs	4
TRI-M HPS3524 PC/104 Power Supply Unit	1
Air Nozzles (Custom)	8
Ninja SL2 4500 psi/45cu Air Tank	1
ProSense Digital Pressure Gage (DPG1-200)	2
Step-Down Switching Voltage Regulator Module	1
Reaction Wheel Shunt	1
Waveshare High-Precision AD/DA Expansion Board	1
Geekworm Jetson Nano WiFi Adapter for 3.0 USB	1

5.1 System Models

In order to comprehensively depict the functioning of the FSS, three distinct models are presented. The first two are block diagrams, which provide a detailed breakdown of the pneumatic and electronic subsystems respectively. These diagrams offer a granular view of the internal workings of these sub-components. In addition to these block diagrams, a comprehensive system model language (SysML) model has been developed to provide a holistic view of the entire system. The SysML model connects and visualizes the various

components of the FSS, allowing for a better understanding of how the subsystems interact and work together as a whole.

5.1.1 Pneumatic Block Diagram

Figure 5.3 displays the final pneumatic schematic of the FSS. The air is sourced from the 4500 psi air tank where it immediately passes through the 4500 psi tank regulator that adjusts the pressure to 800 psi. A reducer funnels the air to the panel mount value that is utilized to turn on/off the pressurized air to both the air nozzles and the air bearings. This valve should be closed at all times when the tank is connected, except when operating the FSS. The pressurized air is then split and fed through two separate stabilizers that reduce the pressure from 800 psi to 60 psi. Each of the two stabilizers is connected to a digital pressure gauge to ensure the air pressure is reduced to 60 psi and a push-button bleeder valve to vent the system when required. Of the two sides connected to the stabilizers, one is utilized for the air thruster system and one is utilized for the air bearings. The air thruster system consists of eight solenoid valves to which an air nozzle is attached. The air bearing system consists of a hand return valve to further control the flow to the thrusters and three air bearings attached to the base plate of the FSS.

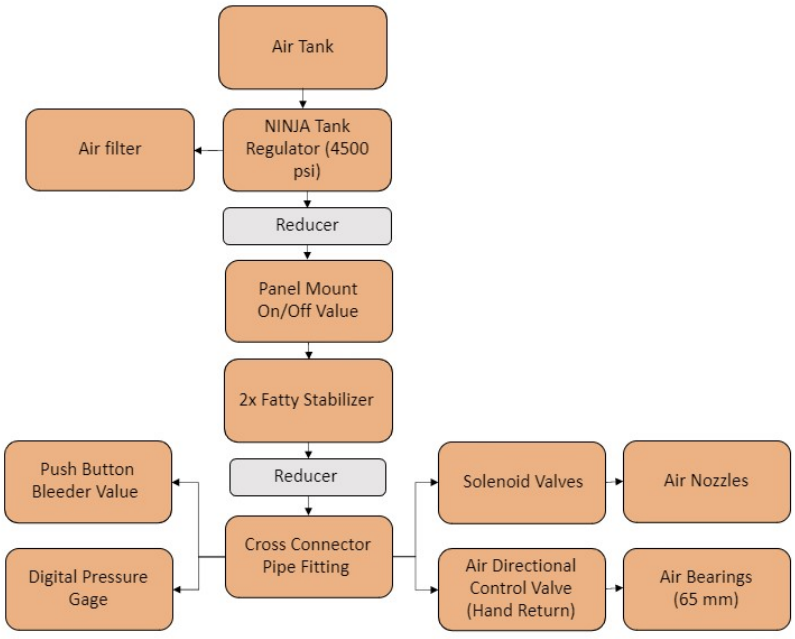

Figure 5.3. Final FSS Pneumatic Schematic

5.1.2 Electronic Block Diagram

Figure 5.4 displays the final electronic schematic of the FSS. All power to the FSS is sourced from four Li-ion batteries coupled to four diode boards. The first battery is connected to the robotic arm via a custom power cord. The second battery tasked with powering the reaction wheel is first connected to a DC-DC step-down switching voltage regulator. The DC-DC regulator is tasked with dropping the voltage along the path from 28.8 V to 18V. A shunt attached between the regulator and the reaction wheel provides additional support to the regulator, monitoring the voltage so that it does not exceed the acceptable limit and preventing any regenerative current from impacting the reaction wheel. The third and fourth batteries are connected to the power supply unit. The power supply unit reduces the voltage from both the 28.8V batteries to 5 V and 24 V, respectively. The 5V output is redirected to the Jetson Nano module and the 24 V is redirected to the relay module in charge of powering the eight solenoids.

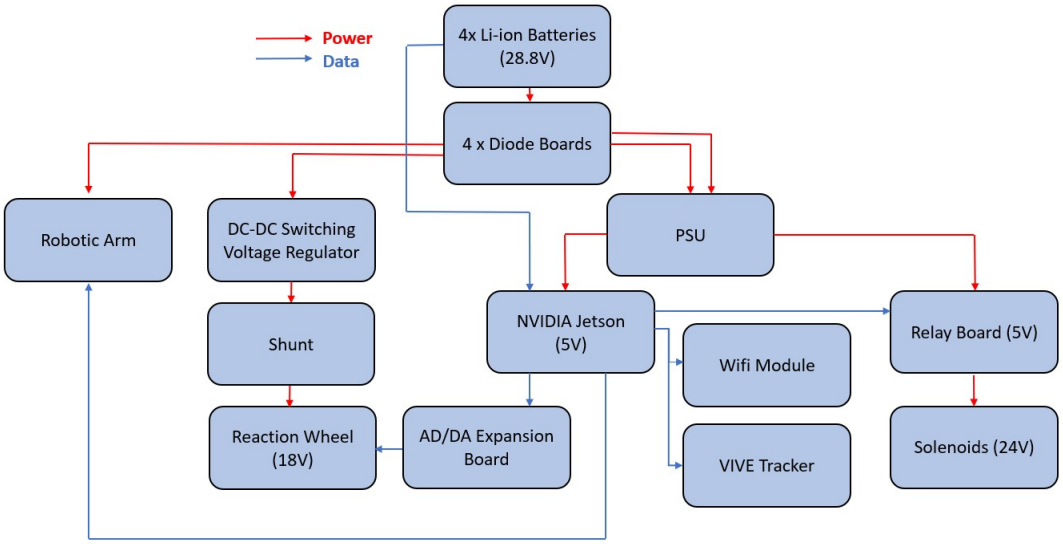

Figure 5.4. Final FSS Electrical Schematic

The NVIDIA Jetson Nano is tasked with controlling the FSS as a whole. The Nano communicates to control the robotic arm, reaction wheel, and relay module. An Ethernet cord connects the robotic arm to the Jetson Nano. The reaction wheel is managed through the AD/DA board that converts the analog and digital signals between the two devices. The Nano also sends commands to the relay board to open and close airflow through the solenoids.

Both the relay board and the AD/DA board are linked to the Nano via GPIO pins. A wifi module is essential to enable the Jetson Nano to communicate with the user wirelessly. It is connected via one of the four 3.0 USB ports. A VIVE tracker is wirelessly connected to the Nano as well to convey the current position of the FSS. The smart battery features of the Li-ion batteries are intended to be employed by linking to the Nano via I2C pins. This connection will provide the user updates on the current battery charge.

5.1.3 SysML Model

A SysML has been employed to depict the FSS sub-systems in a comprehensible visual format. The Magic Systems of Systems Architect software was utilized to create the model [36]. The physical components of the FSS design are represented by individual "blocks," which are interconnected through arrows that illustrate their associations, whether physical or wireless. The block definition diagram featured in Figure 5.5 incorporates only four reoccurring "valueTypes," which are current, voltage, power, and pressure.

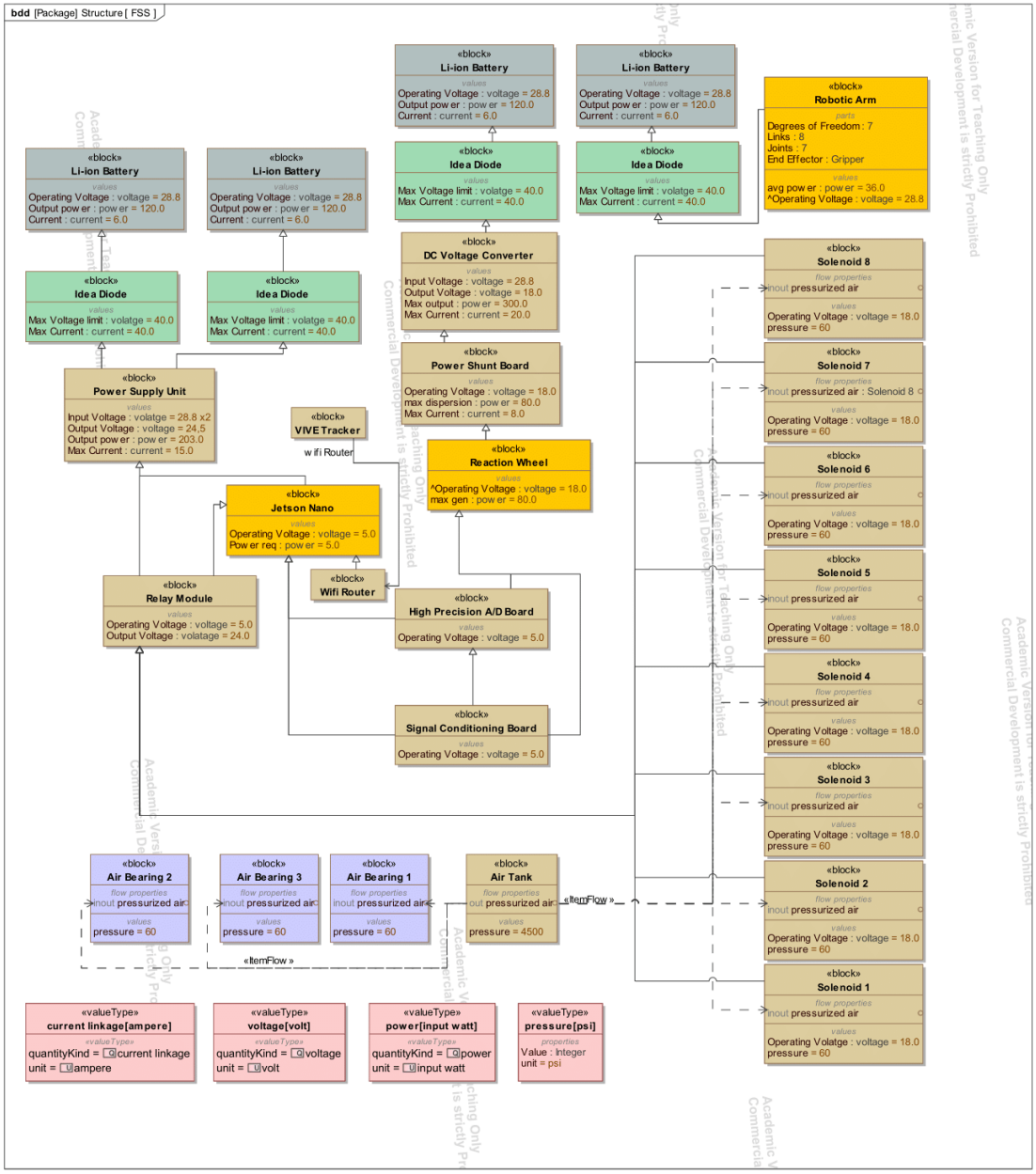

Figure 5.5. SysML model of FSS.

THIS PAGE INTENTIONALLY LEFT BLANK

CHAPTER 6:
Major Electrical Components

This chapter describes the electronic components of the FSS, which play the crucial role of providing power and a means of control to the FSS. These components include the onboard computer, the batteries and their means to distribute power, the reaction wheel and its complementary elements, solenoids, the VIVE tracker, the wireless router, and finally, the robotic arm. The following major electrical components and their specifications are included in the FSS.

6.1 NVIDIA Jetson Nano reComputer

The NVIDIA Jetson Nano acts as the FSS's onboard computer. It supports multiple sensors and electronic components and is the primary way the FSS operator interacts with and controls the FSS. A picture of the Nano can be found in Figure 6.1. The Jetson Nano runs a Linux4Tigra operating system and is capable of running both Python 3.0 and the 3D dynamic simulator, Gazebo. The Nano draws 5V through a DC power jack from the power supply unit, so there is no need to charge it external to the FSS. The Nano offers multiple ports for external connections: HDMI, Ethernet, USB 3.0, micro USB, a camera serial interface, a button header, and a 40-pin expansion header. Not all of these ports are used in the FSS but can provide a segue to be explored in later applications. For the ports and connectors employed by the FSS, a wireless router is attached to one of the USB 3.0 ports, the Ethernet cord spans between the Nano and the Kinova robotic arm, and a variety of GPIO pins of the 40-pin header are utilized. The utilized GPIO pins are used to transfer data between the Nano and the high-precision AD/DA board, relay board, and reaction wheel battery. These pins provide an avenue to control and monitor each module, and therefore the functioning of the FSS. Listed below are the specifications of the computer [37]:

- OS: Ubuntu (Linux4Tigra distribution)
- GPU: NVIDIA Maxwell architecture with 128 NVIDIA CUDA® cores
- CPU: Quad-core ARM Cortex-A57 MPCore processor
- Memory: 4 GB 64-bit LPDDR4, 1600MHz 25.6 GB/s

- Storage: 16 GB
- Display: HDMI 2.0 and eDP 1.4
- USB: 4x USB 3.0, USB 2.0 Micro-B
- Capable of running Python 3.0, Gazebo

Figure 6.1. NVIDIA Jetson Nano reComputer with case removed.

6.2 Inspired Energy Li-ion Battery

Inspired Energy's PH2059HD34 rechargeable smart lithium battery provides power to the entire FSS system. Four packs are utilized, which provides a maximum of 28.8 V to each connected component. Two batteries are connected to the PSU as the primary and secondary sources. One battery is connected to the reaction wheel, and one is connected to the Kinova robotic arm. An ideal diode board is connected to each battery to aid current flow in only one direction. The batteries are easily rechargeable and have a capacity of 3.4 Ah. If the battery discharges its maximum current at 6A throughout its use, it is expected to provide a charge to a system for 34 minutes. A picture of of one of the batteries used on the FSS is found in Figure 6.2. A summary of the Li-ion battery characteristics is provided below [38]:

- Voltage: 28.8 V
- Capacity: 3.4 Ah

- Current: 6.0 A
- Power: 120 W
- Weight: 0.45 kg
- Dimensions: 163.32 mm x 27.18 mm x 81.27 mm

Figure 6.2. Inspired Energy PH2059HD34 Li-ion battery.

Figure 6.3 displays a diagram of the terminal found on each of the batteries used for power and data transfer.

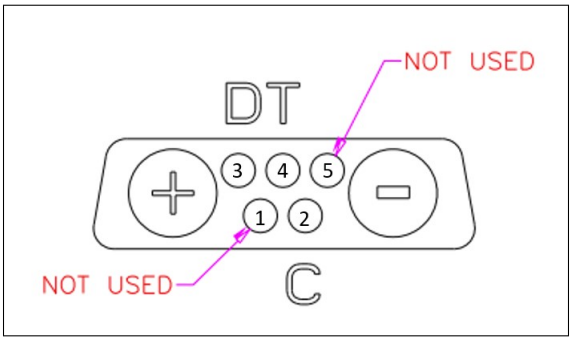

Figure 6.3. Li-ion battery terminal.

Table 6.1 provides a further description of each pin and its function.

Table 6.1. Battery Terminal Specifications

Terminal	***Description***
A1	Positive side of battery
2	SMBus Clock
3	SMBus Data
4	300 Ω ±5% resistor connected between (4) and (A2)
A2	Negative side of battery

The battery terminal includes system management bus (SMBus) pins for data transfer. SMBus is a subset of the inter-integrated circuit (I2C). I2C is a serial communication protocol that transfers data between devices in a system connected to a computer. The protocol consists of a serial data line (SDA) and a serial clock line (SCL) [38]. The SMBus clock terminal, the SCL wire in this case, is the signal connection for the SMBus protocol to synchronize and coordinate the data transfer from the battery to the computer system, which in this case is the Jetson Nano. The SMBus data terminal, the SDA wire, is the signal connection for the SMBus protocol to transfer the hard data from the battery to the Jetson Nano. The SMBus wires from the batteries will be connected to the nano's expansion header in the allotted pins labeled SDA and SCL to be later used to monitor the charge of the chosen battery while the FSS operates [38].

6.3 Ideal Diode Board

The EB429 Ideal Diode Board for Inspired Energy "P" Series battery packs allows paralleling batteries passing 5–40VDC up to 40A in one direction. A diode board is attached to each of the Li-ion batteries to prevent reverse currents and damage to both the batteries and nearby sensitive components. A picture is found in Figure 6.4. The diode fits a battery with a 7W2 D-sub DB male 90-degree connector and has a 7W2 D-sub DB female 90-degree connector output. The connectors include seven pins total: two for power supply and five in the middle for data transfer. The ideal diode kit includes male pins to fit the diode's female output in which all components are connected to the batteries. Listed below are the specifications of the diode board [29]:

- Weight: 30 g.
- Dimensions: 7.62 cm x 5 cm
- Connectors: 7W2 D-sub DB, 90-degree
- Forward voltage limits: 5–40 VDC
- Max rated forward current: 40A

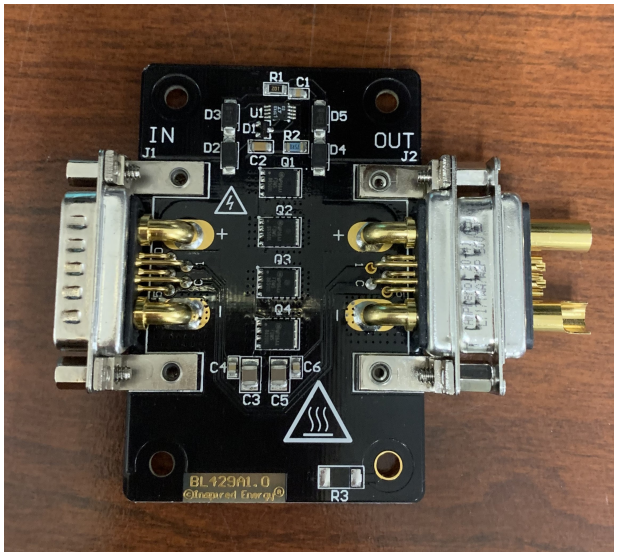

Figure 6.4. Inspired Energy EB429 ideal diode board.

6.4 Reaction Wheel

The space-rated reaction wheel was obtained from Ball Aerospace. It assists in stabilizing the FSS during the robotic arms motion. The wheel is a momentum exchange device consisting of rotating wheel, in which the wheel impart a torque, or angular momentum, in an equal and opposite direction from the robotic arm moving the FSS.

The 20.3 N-m-s reaction wheel requires an 18 VDC external input capable of supplying at least 5 A. To receive power from the Li-ion batteries, the voltage must first pass through the DC switching voltage regulator to step down from 18.8V to 18V. Then, current passes through the shunt in case of regeneration from the wheel, that may cause a return of stored energy and damage to both the wheel and battery. Finally, a twisted quad provides voltage to the wheel. The wheel cannot operate by only applying a voltage. It is an analog mechanism,

so to request torque, an analog command must be received by the wheel. A digital signal is issued by the Jetson Nano, passes through both the AD/DA board and the custom signal conditioning board, and then a torque request is received by the wheel and executed. The wheel provides a return analog signal with the current torque.

The full layout of the wheels interface is found in Table 6.2.

Table 6.2. Reaction wheel electrical interface connections. Source: [32].

Pin	***Signal Name***	***Comments***
1,6 2,7	+18 VDC Bus Input +18 VDC Bus Return	Twisted Quad
3	Chassis Ground Return	Single Return
14 15	Motor Torque Command Motor Torque Command Return	Twisted Pair
4	Motor Disable	-
13	No connect	-
11 12	Motor Torque Feedback Motor Torque Feedback Return	Twisted Pair
8 9 10 5	Hall Phase A Output Hall Phase B Output Hall Phase C Output Hall Return	Twisted Quad

The bus input and output (pins 1-2, 6-7) provide power to the wheel, as mentioned previously. The motor torque commands (pins 14-15) provide the analog torque command signal with an amplitude of +/- 2V, corresponding to a motor torque of 0.106 N-m. A positive torque signal causes the actuator to rotate in the positive direction (counter-clockwise). The motor disable command (pin 4) yields the option to turn off the reaction wheel's drive signals to the motor. This is accomplished by connecting pin 4 to either the hall return signal (pin 5) or the motor torque feedback return (pin 12). If the motor disable pin is left unconnected, the motor torque control is available to receive the necessary torque commands to operate the wheel.

The chassis ground return (pin 3) is connected within the wheel to its mechanical housing to ensure an electrical connection between them. The motor torque feedback (pins 11-12) is an output analog signal that represents the current motor torque. The output range is +/- 5V, which again corresponds to a motor torque of 0.106 N-m. Hall phase outputs (pins 8-10,5) are utilized for reversing the direction of the three-phase brushless direct-drive motor inside the wheel. A brushless direct drive motor is a type of electric motor that uses electronic commutation to switch the current direction. They provide precise speed control and high reliability, which is often required in aerospace applications. The three hall phases –A, B, and C– are 120 electrical degrees apart in phasing, placing them at 240, 120, and 0 degrees, respectively. Four cycles are output per each mechanical revolution of the flywheel [32]. A summary of the reaction wheel's characteristics is provided below, with a picture found in Figure 6.5.

- Input Voltage: 18 VDC
- Power: 16.5 W nominal, 80 W peak
- Angular momentum: 20.3 Nms
- Speed range: +/- 2500 rpm
- Command/Telemetry Interface: Analog
- Weight: 9.07 kg
- Diameter: 28.2 cm

Figure 6.5. 20.3 N-m-s reaction wheel mounted on the middle plate.

6.5 AMEIRMC Switching Step-Down Voltage Regulator

The voltage regulator reduces the 28.8V battery voltage to 18V for the design limit of the reaction wheel. After the current passes through the battery, it is routed through the regulator, and then to the custom shunt. A ripple voltage of less than 50mV ripple is noted on the product's datasheet but was found to be incorrect after in-house testing with an oscilloscope. Roughly 65 mV is the recorded value for a test voltage of 28.8V in and 18V out at 4.2A. The ripple and noise both increase with an increase in input voltage. Using the same oscilloscope, we measured the noise to be about 400kHz, which is a relatively high value. However, the voltage passes through a Zener diode in the shunt before reaching the reaction wheel, which is expected to filter a portion of this noise. A picture of the regulator can be found in Figure 6.6, and the specifications are listed below [31].

- Input Voltage Range: 6–40V
- Adjustable Output Voltage Range: 1.2–36 V
- Current Range: 0–20A
- Max Output Power: 300W
- Efficiency: (up to) 95
- Size: 60 x 53 x 27mm

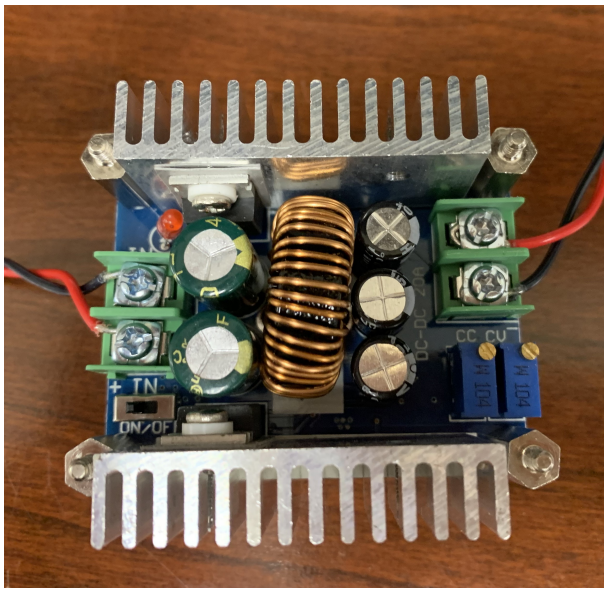

Figure 6.6. AMEIRMC switching step-Down buck voltage regulator.

6.6 Custom Shunt

A shunt was required in between the switching voltage regulator and the reaction wheel to absorb regenerative energy generated during the motor reversal of the flywheel. After an extensive search to find a commercially available shunt with a rating capable of dispersing 80W at the wheel's voltage rating was found to be inconclusive, a custom design was engineered by an SSAG technician for the demanded rating. Figure 6.7 displays a schematic of the design.

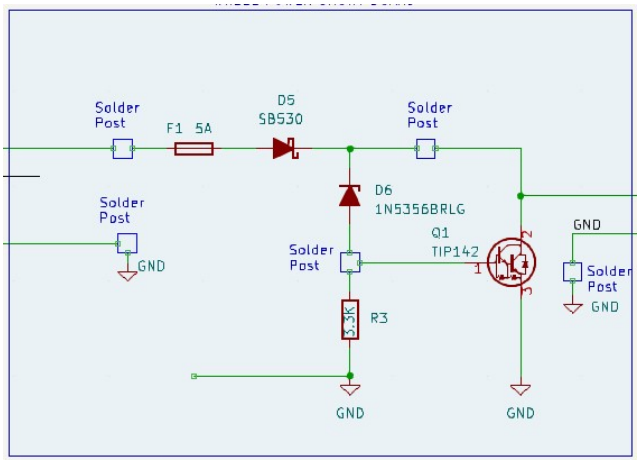

Figure 6.7. Shunt design in KiCad software.

The design consists of a Schottky diode (D5), Zener diode (D6), 3.3K resistor (R3), bipolar transistor (Q1), and a heat sink (F1) soldered onto a breadboard. Solder posts are used in the design to attach the wires coming from the 18V reaction wheel and the switching voltage regulator. The shunt characteristics are summed up below, and a picture of the final product is found in Figure 6.8.

- Power dispersion: 80 W
- Max voltage rating: 20 V
- Max current rating: 8 A

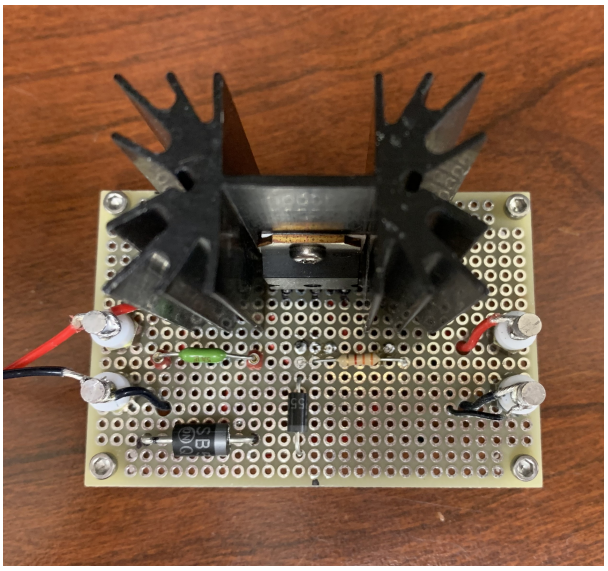

Figure 6.8. Final product of the custom shunt design.

6.7 Waveshare High Precision AD/DA Board

The commands to control the reaction wheel are intended to be sent from the Jetson Nano, but an issue presents itself as the Jetson Nano is a digital signal device and the wheel requires an analog signal. To overcome this issue, an analog-to-digital/digital-to-analog board is introduced into the system. The analog-to-digital converter built into the board works by first sampling the analog signal and then quantifying the sample into binary values based on the amplitude. For the reverse conversion, digital to analog, the binary samples of the digital signal are first decoded into a sample of a fixed number of bits. The bits represent the resolution of the sample. The sample is then reconstructed into a continuous waveform that approximates the original resolution and numerical values. The AD/DA board connects directly to the Jetson Nano GPIO interface (40-pin connector) and offers a screw terminal for input on the analog side. A snapshot of the board can be found in Figure 6.9, and the characteristics are listed below [33]:

- Analog to digital conversion: 24-bit high precision DAS, 8 channels.
- Sampling Rate: 30 kps
- Digital to analog conversion: 16bit high-precision DAC, 2 channels.

- Power supply: 3.3V or 5V

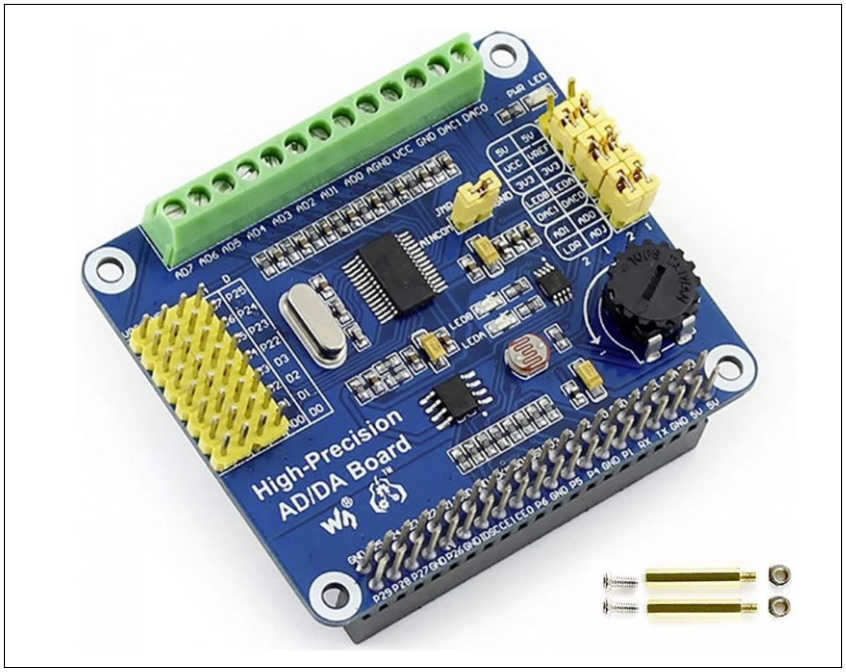

Figure 6.9. High precision AD/DA board. Source: [33].

6.8 Custom Signal Conditioning Board

A signal conditioning board is necessary to condition the motor torque command signals received and accepted by the reaction wheel to be compatible with the AD/DA board. The characteristics of the reaction wheel deliver the command motor torque analog signal at a +/- 2V range, but to be received by the AD/DA board, the analog and digital inputs must be a positive value between 0 – 4V. To deal with the polarity of the +/- 2V signals necessary to control the reaction wheel's torque commands, a custom board with a charge pump switching regulator (U1), voltage reference (U2), inverting gain amplifier(U3), instrumentation amplifier (U4), and a no-inverting buffer (U5) as the main components were designed by an SSAG technician. The board design is displayed in Figure 6.10.

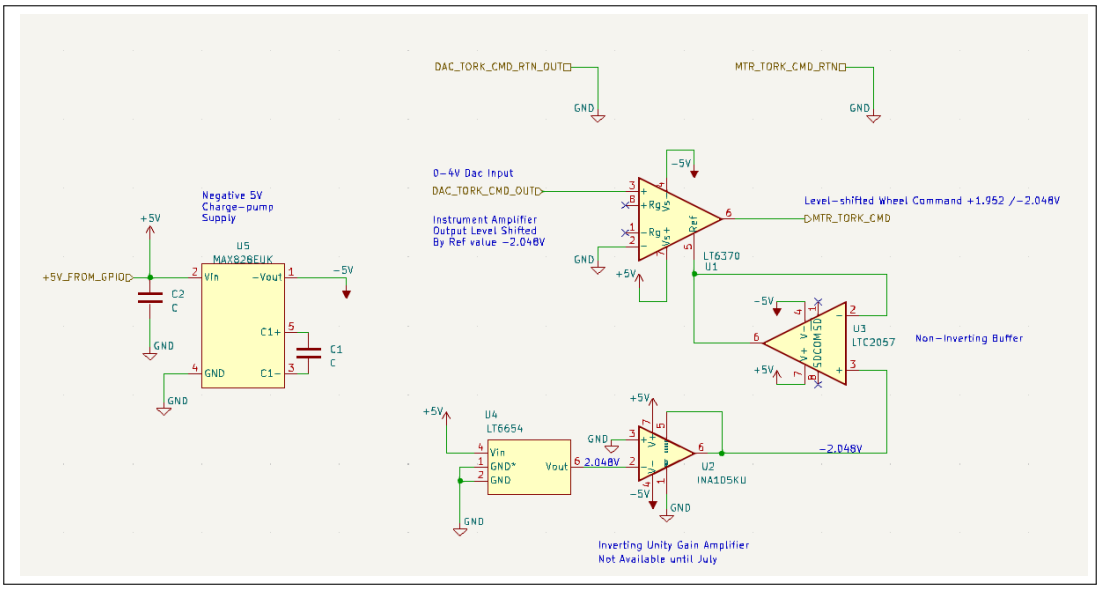

Figure 6.10. Custom signal conditioning board design in KiCad.

The board requires an +5V input from the Jetson Nano's GPIO interface to operate and interacts only with the motor torque command twisted pair from the reaction wheel. No other wires from the reaction wheel are required to be routed through the conditioning board. The actual construction of this custom board will not be initiated during the timespan of this thesis due to the availability of the inverting gain amplifier.

6.9 HPS3524 Power Supply Unit

The PC104 power supply unit (PSU) supplies and manages power to the Jetson Nano and through the relay module to the solenoids as a glorified voltage regulator. A picture of the board is found in Figure 6.11.It includes a flash-based microcontroller and an RS232 serial port designed for a system requiring a wide input power range. The microcontroller and serial port will not be used in this application. The DC inputs to the PSU include both main and secondary power sources, both of which are Li-ion batteries. The primary source is intended to power the +24V. The secondary source is intended to power the +5V. The PSU supplies a +3.3V, +5V, and +24V output, over an extended temperature range, -40 to +85 °C. The +5V terminal powers the Jetson Nano via a DC power jack. The +24V terminal connects via wire to each of the eight relays to power the eight connected solenoids. There

is an opportunity to connect more devices to the PSU in future applications, as only two of the six output terminals are utilized. Green LEDs on the PSU light up when the device is powered on. Listed below are the specifications of the PSU [39]:

- Outputs: +3.3V output 10A, +5 output 15A, +24V output 2.5A, +5VSB output 7A, all terminal are rated for 8 A
- Maximum output power: 203 W
- Input Voltage: 6–40 VDC
- Efficiency: 90
- Mechanical Shock & Vibration: MIL-STD-810 levels
- Size (W x L x H): 3.55” x 3.775” x 0.6”
- Weight: 7.30oz / 206.95g
- Temperature Range: -40 to +85°C

Figure 6.11. HPS3524 power supply unit.

6.10 TRI-M IR104-V4 PC/104 Relay Board

A relay board is used to control the switching of electric circuits with a low-power signal. A picture of the board is found in Figure 6.12. In this project, the relay board is used to switch power on and off to control the eight solenoids. The module provides 20 independent relays in SPDT form to allow contacts with an input voltage of 3-24 VDC at 5A. The output relays are normally off unless a signal is received to "open" or turn on a relay. A 24V voltage is fed from the power supply unit to the relay module to be dispersed to the solenoids whenever a signal is received by the module from the connected Jetson Nano GPIO pin. The module additionally receives a supply voltage of 5V from the Jetson Nano for basic module operation. This relay board was scrapped from an older generation FSS, so the contacts might exhibit wear from long use at high voltages. Listed below are the specifications of the relay board [40]:

- Input Relay Type: 20 Opto-isolated
- Output Relay Type: 20 SPST
- Contact rating: 5A @ 30VDC
- Input Voltage: 3–24 V DC or AC
- Operating Temperature: -24 °C to 70 °C
- Mechanical Life: 70,000 min at rated loads
- Dimensions: 90 mm x 96 mm x 12.5 mm
- Weight: 127 g

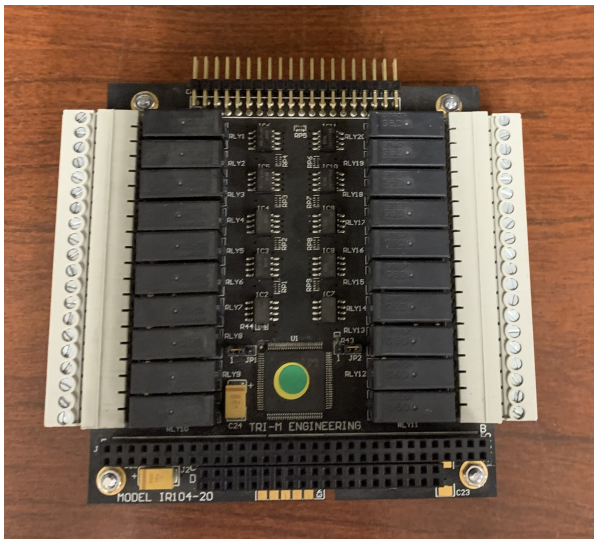

Figure 6.12. TRI-M IR104-V4 PC/104 relay board.

6.11 HTC VIVE 3D Tracker 3.0

The VIVE tracker is a sensor that provides high-precision positional tracking of the FSS to be integrated into virtual reality. A picture is included in Figure 6.13. The VIVE pairs with two Bluetooth HTC base stations set up on the edge of the granite table where the FSS floats and an HTC VR headset connected to a computer via HDMI, USB, and power. The whole system uses Steam VR to record a virtual reality environment in which the VIVE can be tracked with signals beamed from the base station and received by the headset. The VIVE is mounted with Velcro on a side support but can be placed anywhere on the FSS to be tracked if it is in view of at least one base station. The VIVE tracker itself is operated wirelessly and does not need to interact with the Jetson Nano or any power source aboard the FSS. The VIVE is charged separately via micro USB and uses a separate Bluetooth USB 2.0 to connect to the PC running Steam VR and recording the tracking data. Listed below are the specifications of the VIVE 3.0 tracker [41]:

- Input Voltage: -0.5 to 3.6 V, Supply voltage 3.3V
- Current: 4 – 20 mA
- Connection: Micro USB, pogo pin
- Optics: 270 degrees tracking field of view (FOV)

Figure 6.13. HTC VIVE 3D tracker.

6.12 Geekworm Wireless USB Router

The Geekworm wireless USB router is a solution for accessing the internet wirelessly on a Jetson Nano. It offers a dual-band 1200 Mbps WiFi and is compatible with the Nano's Ubuntu operating system. To set it up, a driver must be installed on the Nano, and then the router can be plugged into one of the four USB 3.0 ports on the Nano [42]. The router will enable wireless communication between the operator and the FSS, allowing the operator to send commands to monitor and control the thrusters and robotic arm. Overall, the Geekworm wireless USB router provides a convenient and effective way to enable wireless communication between the Jetson Nano and the operator, making it an ideal choice for the remote operation of the FSS. Figure 6.14 depicts the Geekworm wireless USB router and some of its following characteristics [42]:

- Internet Speed: 1200 Mbps
- Interface: USB 3.0
- Antenna Type: 5dBi SMA
- System Requirement: Ubuntu, Windows CP, Linux2.6

- Modulation: DBPSK, DQPSK, CCK, OFDM, WPA-PSK/WPS2-PSK
- Frequency: 2.4 GHz and 5 GHz (dual band)

Figure 6.14. Geekworm wireless USB router. Source: [42].

6.13 Kinova Gen 3 Ultra Lightweight Robotic Arm

The robotic arm is the primary payload of the FSS, pictured in Figure 6.15. The 7 DoF robotic manipulator consists of seven actuators at the seven joints. The actuator sensors provide torque, position, velocity, current (motor), voltage, and temperature (motor) of the arm. The seventh joint is kinematically redundant and, thus, the arm is capable of complex configurations and operations. Additionally, each actuator joint range is infinite but can be restricted by software limitations. An interface module is located on the wrist at the end of the arm to attach a chosen end-effector. An end-effector is a tool mounted on the end of robotic arm, which in this case is a gripper. At the arms place on top of the FSS, and is intended to be used for satellite arm-capturing experiments. It is easily manipulated with the control algorithm provided by Kinova, but its algorithm assumes the robot is mounted on a motionless surface. For use in space arm capturing experiments, the robotic arm must possess a more intricate control algorithm to handle the dynamic shift of the FSS vehicle every time the arm moves. This topic is further explored in a thesis by ENS Matthew Tungett, the Dynamic Modeling, and Simulation of a Floating Spacecraft Simulator Utilizing a Kinova 7DoF Robotic Arm [43]. Aboard the FSS, the arm is powered by one of the Li-ion batteries via a custom power cord, and the Ethernet outlet at the base of the arm is connected to the Jetson Nano to receive commands. The basic characteristics of the 7 DoF Kinova robotic arm are listed below [44].

- Weight: 8.2 kg
- Total Length (without gripper): 1.2 m
- Maximum transitional speed: 40 cm/s
- Supply Voltage: 18 – 31 VDC, 24 VDC nominal
- Nominal power: 36 W
- Material: Aluminum & Carbon Fiber
- Maximum reach: 0.902 m
- Software: KINOVA KORTEX
- Controller interfaces: USB 2.0, Micro USB, Ethernet, HDMI, Bluetooth, WiFi

Figure 6.15. Kinova Gen3 Ultra lightweight robot. Source: [45].

CHAPTER 7:
Major Pneumatic Components

This chapter describes the pneumatic components of the FSS, which play a crucial role in its frictionless motion. These components include the air tank, regulators, solenoid valves, and air bearings, all of which work together to provide the necessary pressurized air to maintain the FSS's air thrusters and air bearings.

7.1 Ninja SL_2 Air Tank

The 4500 psi (31 MPa) rated, 45 cubic inches (737.4 cm^3) Ninja SL_2 air tank positioned on the bottom plate supplies the air for the air bearing and air thruster systems. It can be considered the endurance limiting factor for the entire FSS. If the tank runs out of air, the air bearings that allow the FSS's flotation and the air thrusters that produce the FSS's intentional translational movement would be eliminated. The tank is connected to the primary regulator, the Ninja Ultralite Adjustable Tank Regulator, and can be found in Figure 7.1. The following list provides a summary of the air tank's characteristics.

- Volume: 45 in^3 (or 737.4 cm^3)
- Rated: 4500 psi (31 MPa)

Figure 7.1. 4500 psi air Tank

7.2 Ninja Ultralite Adjustable Tank Regulator

The air tank regulator, which comes attached to the 4500 psi air tank, has the ability to adjust the output pressure to 500, 650, or 800 psi (see Figure 7.2). For this project, 800 psi was the chosen output pressure. The regulators control the pressure from the air tank before passing it through the Fatty stabilizer air regulator to the air thruster and air bearing systems. In addition, the regulator is equipped with a pressurized air filler nozzle enabling the air tank to be refilled when necessary [46]. The characteristics of the Ninja Ultralite Adjustable Tank Regulator are summarized below.

- Weight: 3.75 oz (0.11 kg)
- Input Pressure: 4500 psi (31 MPa)
- Adjustable Output Pressure: 500, 650, 800 psi
- Includes SRT piston and mini fill valve.

Figure 7.2. Ninja ultralite adjustable tank regulator, which came attached to the air tank.Source: [46].

7.3 Fatty Stabilizer CO_2 Air Regulator

The FSS's pneumatic system includes a secondary regulator with an input pressure up to 4500 psi and an adjustable output pressure range between 0–400 psi (see Figure 7.3). The stabilizer, which receives an input of 800 psi from the adjustable tank regulator, reduces the pressure to 60 psi. This regulator then supplies compressed air at the appropriate pressure for the air thruster and bearing systems [47]. The input and output pressures of the air regulator are summarized below.

- Input Pressure: 0–4500 psi (31 MPa)
- Output Pressure: 0–400 psi (2.76 MPa)

Figure 7.3. Fatty Stabilizer CO_2 Air Regulator.

7.4 Gems Sensors Solenoid Valves

Gems Sensors & Controls provided the eight solenoid valves used in the air thruster systems (see Figure 7.4). These highly durable and corrosion-resistant components are capable of providing high flow and pressure while conserving power. These valves can be adjusted for either 2-way or 3-way airflow, but this research uses the 2-way airflow option. The solenoids are mounted to the middle plate of the FSS, on the same level as the reaction wheel. The air source is the bottom-level air tank, which provides gas to both the air bearings and the solenoids. The solenoid leads are connected to a relay board to provide 24V to all eight solenoids and control their on/off state [48].

- Voltage required: 24V
- Maximum Operating Pressure Differential (MOPD): 175 psi
- Power: 0.65 – 2.0 Watts
- Value Flow Coefficient (C_v): 0.018 – 0.070

Figure 7.4. Solenoid valve.

7.5 65mm Flat Round Air Bearings

The air bearings used to support the FSS's frictionless motion are provided by New Way (see Figure 7.5). These bearings have a 65 mm diameter with a 0.41 MPa (60 psi) input pressure, which allows each bearing to hold a load of 666 N (150 lbs). These air bearings are mounted to the base plate with a ball mounting screw. Compressed air is supplied through an air tank, passes through the two regulator stages, and then provided to each of the three air-bearing pucks [34]. The air bearing characteristics are outlined in the list below.

- Dimensions: 65 mm diameter, 20 mm height
- Pressure: 0.41– 0.552 MPa, Max: 0.689 MPa
- Ideal Load: 666 N
- Recommended fly height: 5 microns
- Flatness: 0.0005 mm
- Weight: 0.15 kg
- Maximum Speed: 50 m/s

Figure 7.5. New Way 65mm flat round air bearing.

The chart in Figure 7.6 indicates the lift generated by each of the three air bearings. Figure 7.6 outlines the ideal load and the recommended operating range for a single 65mm air bearing operating at 60 psi. By dividing the FSS's total weight of 900 N by three, each air bearing supports about 300 N. This means that each bearing has about 12.5 microns of lift, which is less than the ideal load and is not within the recommended operating range. Light air bearing loads immediately raise some concerns for the operation of the FSS, as too much lift can possibly cause unpredictable and inconsistent behavior stemming from the slight instability in the load. Fortunately, the majority of the FSS's experiments will involve its robotic arm and robotic capturing experiments, and the accuracy of the arm will not be affected by an instability error of a few microns. This research originally called for 50mm air bearings, but due to supply issues they could not be found, as mentioned in Chapter 4.

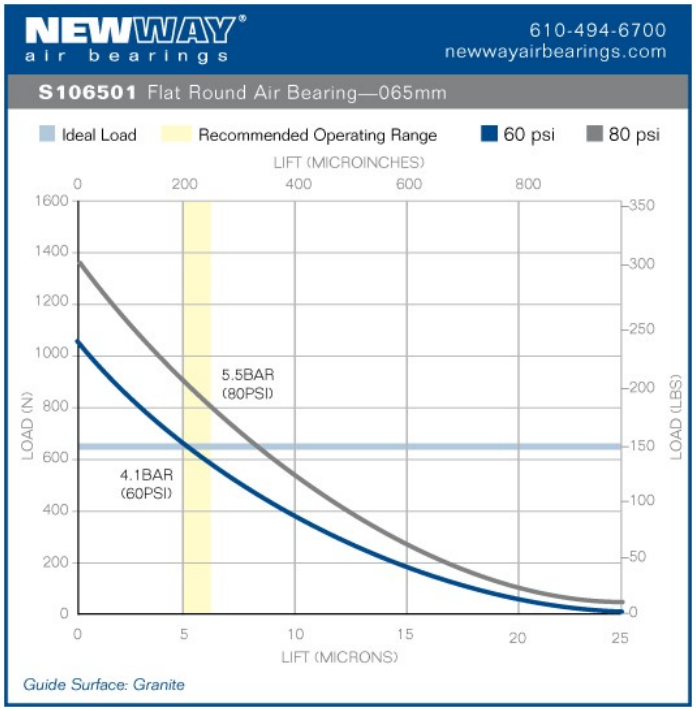

Figure 7.6. Lift performance for a 65mm flat round air bearing. Source: [34].

7.6 ProSense DPG1-5000 Digital Pressure Gauge

The installation of two digital pressure gauges in the airline after the second regulator stage provides readings of the air pressure to the solenoids and air bearings (see Figure 7.7). When the FSS system is supplied with air, the gauges should read 60 psi. By having real-time pressure readings, any pressure fluctuations or drops can be quickly detected, minimizing the risk of potential system failure. The DPG1 provides sensing up to 5000 psi with +/- 0.5% measurement accuracy and is operated by a simple two-button system [35].

- Scale: 0-500 psi
- Accuracy: 0.5
- Material: stainless steel
- Unit options: psi,mH2O, mmHg, mbar, kPa
- Connection: 1/4in male NPT
- Power source: AAA batteries

Figure 7.7. ProSense DPG1-5000 digital pressure gauge.

THIS PAGE INTENTIONALLY LEFT BLANK

CHAPTER 8:
Fabricated Components

Not all components of the FSS could have been ordered online. The air nozzles, metal plates, rods to hold the standoffs, and hardware mounts had to be custom designed. They were manufactured with the help of NPS's laboratories using either additive manufacturing or machining.

8.1 Additively Manufactured Nozzles

The nozzles to be utilized in the air thruster system were custom designed by previous researchers to be more efficient in spacecraft simulator experimental tests [49]. The nozzles utilized are supersonic with a higher specific impulse and lower propellant consumption, which extends the life of each run on the simulator. The blueprint design of the air nozzle in inches, though the CAD model was developed in metric units, is found in Figure 8.1 [49].

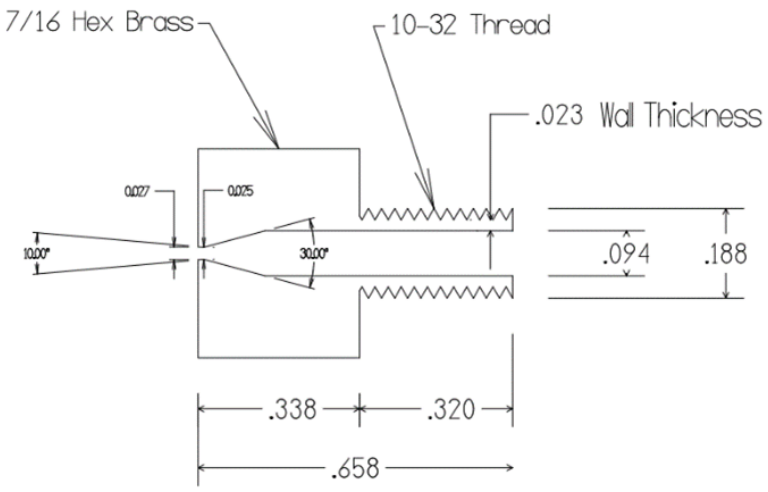

Figure 8.1. The mechanical drawing of the FSS's nozzles. Source: [49].

Prior to printing, this mechanical drawing was recreated in Siemens NX in the appropriate dimensions. We discussed whether or not the eight required air nozzles would be custom-

machined or additively manufactured. Due to the small size of the nozzle and in an effort to preserve the project's budget, the choice was made to additively manufacture the part using the resources available to the NPS Mechanical and Aerospace Engineering department. The EOS M 100, a powder bed fusion printer, was selected to print the nozzles. The material used in this printer was a titanium alloy (Ti64). A powder bed fusion printer can create intricate objects with high precision. It sinters powder particles layer-by-layer via a laser until the part is completed. The part is then evacuated from the remaining powder [50].

The CAD file needed to be slightly edited in preparation for the printing process. Powder bed printers notoriously have difficulty printing objects with sharp edges. To preserve the nozzle but not affect its build, fillets were added to the edges of the hex head. Figure 8.2 displays a snapshot of the finalized model.

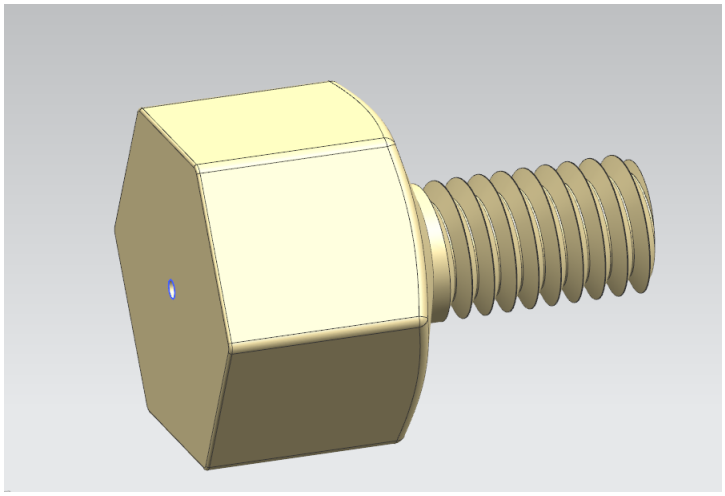

Figure 8.2. CAD model of nozzle in NX.

A test run with the EOS M 100 to print one nozzle was conducted before starting the official print. Some minor post-print machining was required on the hex face and the 10-32 threads to remove extra powder and smooth the surfaces. After the design was determined to be sufficient, the eight nozzles were printed with no issues.

A completed nozzle post-machining is displayed in Figure 8.3. At first, there was concern for the grainy texture on the external surface of the nozzle, as the same was mostly likely found on the internal surface, which would disrupt the air flow. However, whether or not

the nozzle produced its intended exit velocity was considered to be redundant; the nozzles only needed to be capable of producing reasonable movement of the FSS across the granite table. Later, when the FSS was set upon the granite table and a single thruster was fired, the thrust produced from the nozzle was deemed to be reasonable.

Figure 8.3. An AM nozzle after post-processing.

8.2 Additively Manufactured Supports

The supports to be screwed to the bottom plate of the FSS were designed specifically to be 3D printed. The "Fortus 450 mc" printer of the Space Systems Academic Group lab was used to develop the two side supports, two battery holders, and the two air tank supports. All the supports are made of ABS material. The Fortus printer is a fused disposition modeling (FDM) printer that is ideal for simple prototyping. FDM printers are the simplest type of additive manufacturing printer. They use a nozzle to extrude hot filament onto a build plate, layering the hot material, often ABS or PLA, to eventually build a part. The FSS's supports did not require advanced material properties such as high strength and density, so it was established FDM was the best method.

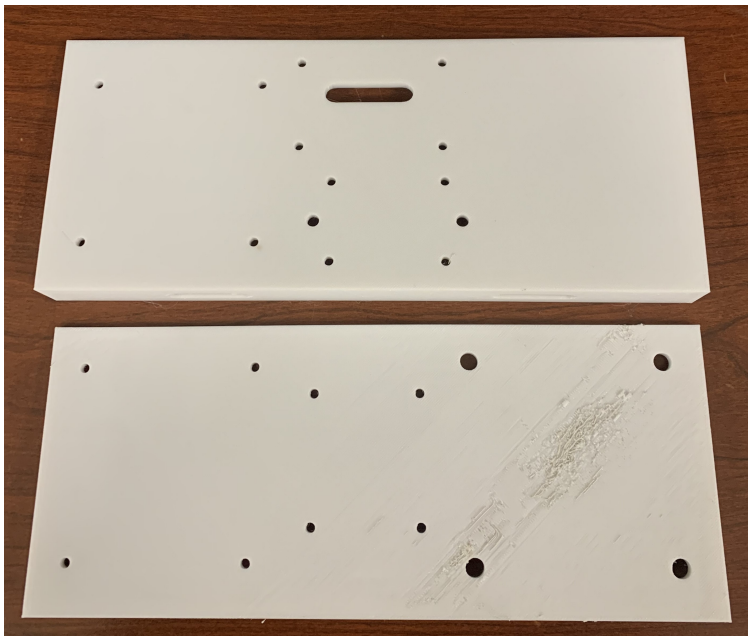

Figure 8.4. Both AM side supports after post-processing.

The side supports prop up the FSS's electric modules and provide easy access for both wiring and manipulation. Holes were designed into the side supports in which the modules could be easily secured by small hexagonal or cylindrical screws Figure 8.4 exhibits the two side supports.

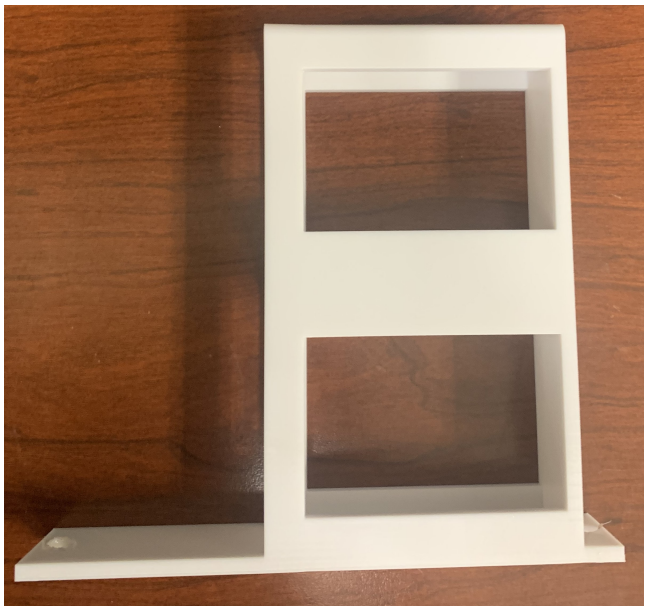

Figure 8.5. One of the two AM battery supports.

Figure 8.5 displays one of the battery supports that holds two batteries. The batteries are slid in horizontally and are not secured themselves, but fit snugly so it is unlikely they will slide out.

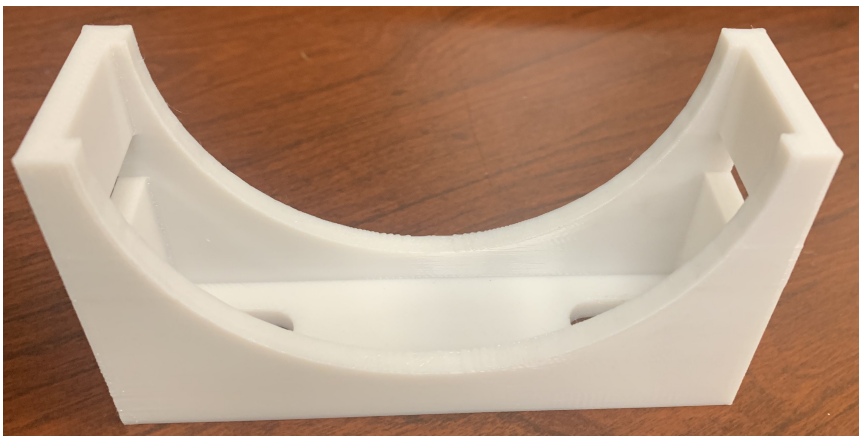

Figure 8.6. One of the two AM air tank supports.

The air tank supports, such as the one in Figure 8.6, were not designed to fit a specific tank size. The holes in the tank support itself allow for sliding left and right, while the holes

cut into the base plate enable both air tank supports to slide forward and back. Adjustable tank supports enable practically any sized tank to be used as long as it can fit between the middle and base plate, and it provides the 31 MPa output pressure required for the pneumatic system.

8.3 Metal Machining

The mounting plates and standoff rods to support the FSS components only had the option to be machined due their material selection and sheer size. The top, middle, and base plates consist of ½-inch thick 6061-T651 aluminum plates. All plates required various cuts and holes to secure components. A picture of the three plates is displayed in Figure 8.7 before construction began.

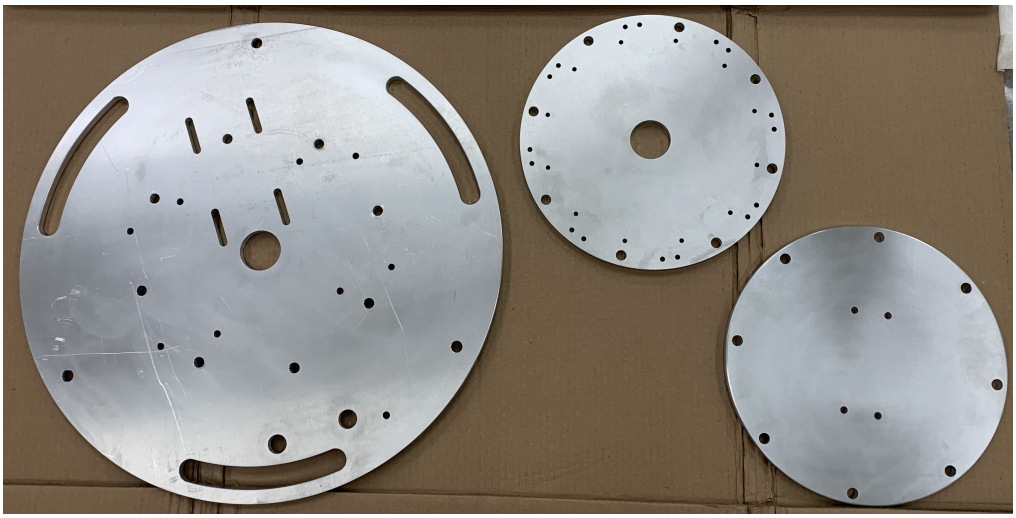

Figure 8.7. The base, middle, and top plates.

The eight standoff rods were cut from ¾-inch diameter 6061-T6511 aluminum into 7-inch lengths. The rods were machined with M8x30 threaded holes in each end to assist in securing the standoffs to the plates. One such rod is displayed in Figure 8.8.

Figure 8.8. A top view of a standoff.

Custom-designed air nozzles, metal plates, rods, and hardware mounts were required for the FSS project and were manufactured with the help of NPS's laboratories using either additive manufacturing or machining. The air nozzles were additively manufactured using a titanium alloy material and a powder bed fusion printer, while the supports were printed using a fused disposition modeling printer. The three aluminum 1/2-inch metal plates and the eight aluminum rods were cut in NPS's SSAG metal machine shop. The design of the nozzles, plates, and various supports were based on the specific requirements of the FSS, and their successful manufacture ensured the FSS's functionality.

THIS PAGE INTENTIONALLY LEFT BLANK

CHAPTER 9:
KiCad Electronic Schematic

A crucial aspect of the FSS's design is its electronic hardware and wiring. It is challenging to manage the wiring of a system and determine how each of the different components are interconnected. To simplify and record the progress of the FSS, an electric schematic of the full system was created in KiCad [51]. KiCad is an open-source software tool for electronic design automation, not only for creating schematics but also for designing printed circuit boards and testing electronic circuits [52]. For this thesis, the schematic was especially beneficial to keep track of how each module is connected down to each individual pin. The full KiCad schematic of the FSS is included in Appendix A for reference. This chapter splits the schematic into sections for a digestible explanation.

It is worth mentioning that not all connector interfaces on these electric modules are completely accurate. When properly presented, a significant amount of clutter is added to the diagram in places where there is no need to go into the intricate details. One such example is the relays on the relay module, which are represented only as screw terminals, not as a full 20-relay wiring diagram.

The Jetson Nano computer is the first hardware component to be discussed, as it serves as the onboard computer and control hub of the FSS. The electronic diagram of the Nano can be found in Figure 9.1, displaying only the main ports and pins utilized. The DC power jack port supplies +5V from the PSU's output terminal to charge the module and automatically power it on. Alternatively, an on/off switch disables the Auto-Power-On mode through pins 1, 2, 5, and 6 of the button header [37]. This optional step permits the Nano to turn on only when the switch is flipped, even when connected to power. An Ethernet cord will span from the Nano to the Ethernet port on the base of the robotic arm, allowing the Nano to send and receive data via this cord since the robotic arm cannot do this wirelessly. The external VIVE tracker is not attached to the Nano computer in any way. Instead, it connects wirelessly to an external PC for positional and rotational tracking. The only reason it is placed next to the Nano on the diagram is that it has a computer-related similarity.

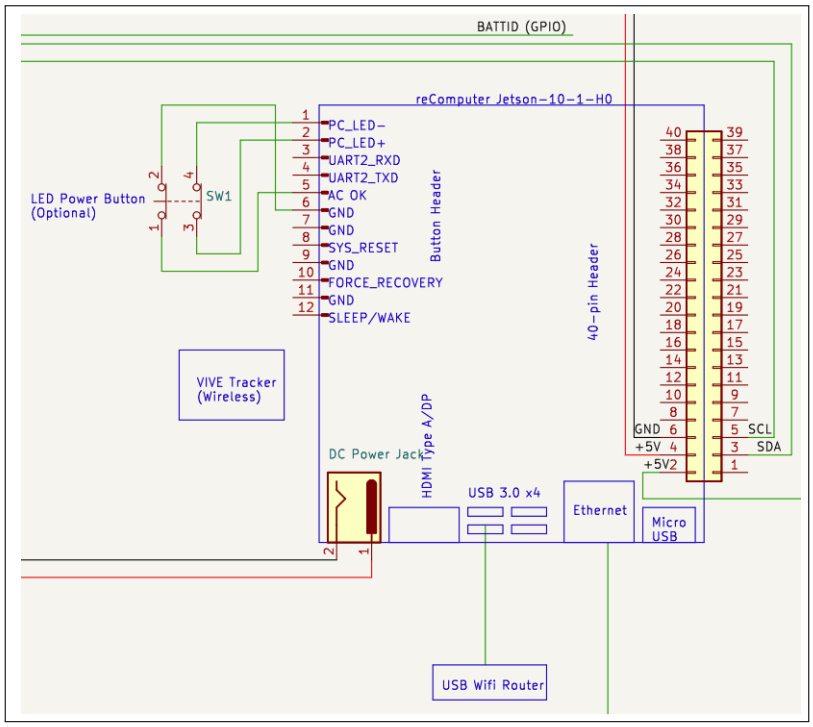

Figure 9.1. Snapshot of the Jetson Nano in KiCad.

The USB wifi router is then connected to one of the four USB 3.0 ports, allowing the Nano to connect to the internet wirelessly. This feature enables the Nano to be updated and accessed remotely, without any wires spanning from the FSS to the user. The remote access feature is vital as it allows the user to remote desktop into the Nano to write and run Python programs necessary for controlling Nano's actions. The 40-pin header is the primary component on the Nano used to interact with the subsystems of the FSS and requires the most programming to control. The 40-pin header will be utilized to control and monitor each connected module. Additionally, the high-precision AD/DA board's expansion header will be directly connected to the Nano's header, with the pin numbers remaining the same. Figure 9.2 shows a diagram of each pin and its function, which is the same header as displayed in Figure 9.1, but in a more detailed form.

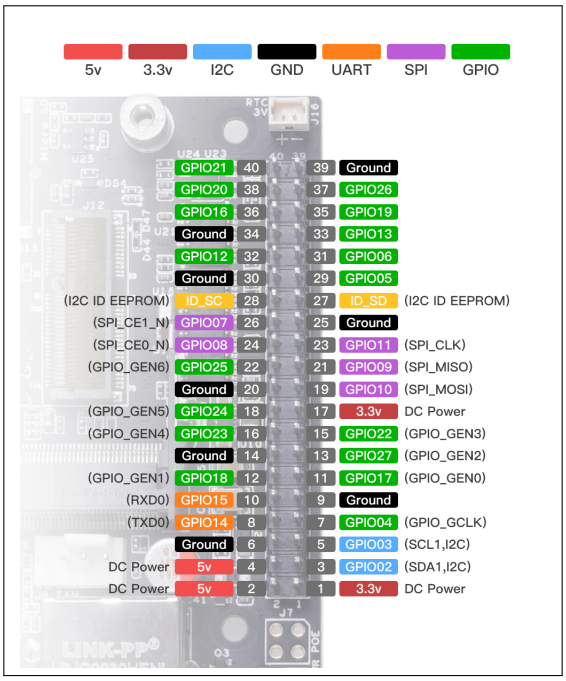

Figure 9.2. Pinout of the Jetson Nano's 40-pin header. Source: [53].

Pin 2 is routed to the signal conditioning board, while pins 4 and 6 are connected to the relay module as a source of power for their respective modules. Pins 3 and 5 are routed to the reaction wheel's battery module via SCL and SDA lines, as previously mentioned in Chapter 6. The GPIO pins, highlighted in green in Figure 9.2, are the primary pins used in this design and can be programmed to perform various functions based on their intended use. A "BATTID" wire spans from the reaction wheel's battery module to a GPIO pin, which will be utilized to monitor the remaining battery charge. The solenoids connected to the relay module will be controlled using eight GPIO pins. Additionally, the AD/DA board will be directly connected to the GPIO header through an expansion board, utilizing no more than eight GPIO pins to send torque commands to the reaction wheel. Although the specific GPIO pin numbers have not been assigned, there are 26 total GPIO pins available for use. All pins on the GPIO header will be connected using jumper cables.

In the diagram, we will discuss the power source for the Jetson Nano and the eight solenoids. Figure 9.3 shows the layout of the battery design, and we will use the Jetson Nano's battery module as an example to explain it. The battery module consists of an Inspired Energy

Li-ion battery, an Inspired Energy diode board, and attachable 7W2 D-sub connectors that come as a kit. The Li-ion battery is represented by a blue rectangle labeled with its battery specification number (DSPH2059HD34) and output voltage (28.8V). The battery connects to the system using a female 7W2 D-sub connector with the same pinout as shown in Chapter 6, Figure 6.3. This connector fits directly into a male 7W2 connector found on the ideal diode board, also represented as a blue rectangle with the individual part numbers and male and female 90-degree 7W2 connectors. The last 7W2 connector is used to connect one side to the female side of the ideal diode board, while the other side has male cup connectors.

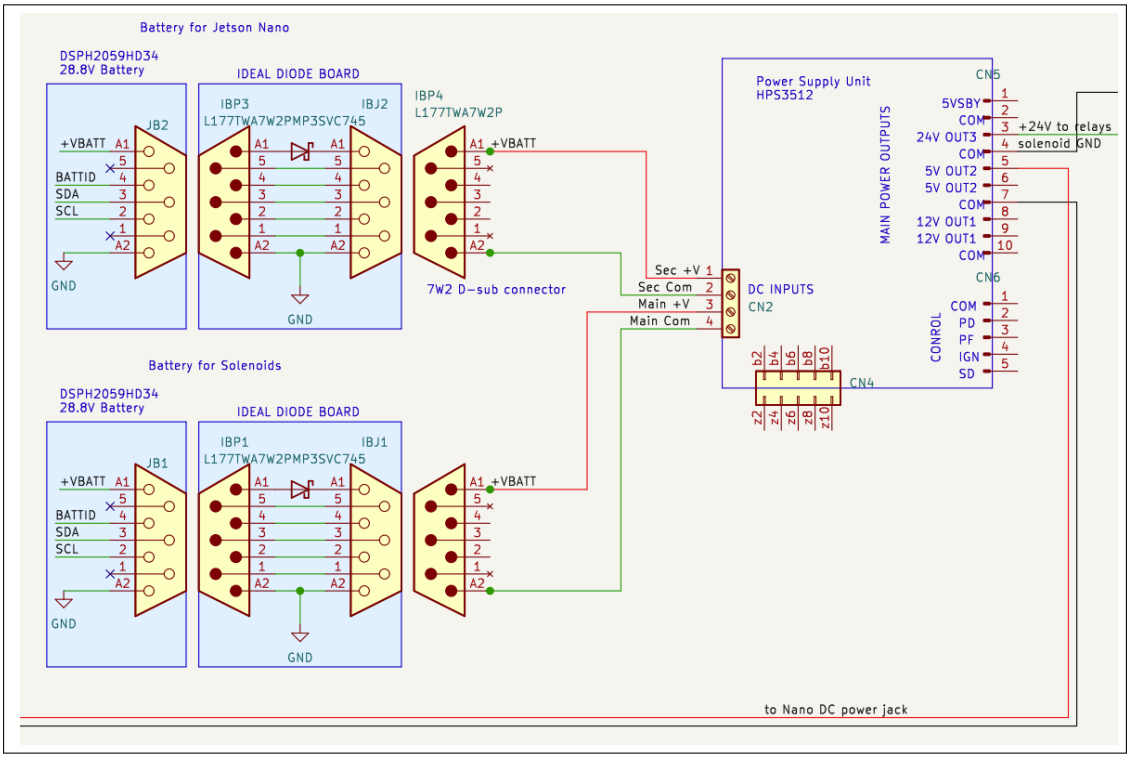

Figure 9.3. Snapshot of the Jetson Nano, solenoid batteries and the PSU in KiCad.

The two battery modules are wired with 20 AWG wires to the main and secondary source screw terminal (CN2) of the power supply unit. CN6 is the control terminal and CN5 is the main power output, with both connectors using plug-in pins. The control terminal is not utilized in this thesis but is included as there could be future applications if the efficiency of the PSU requires an increase. The 24V OUT3 (pin 3 of CN5) provides the +24V to the relay

module to operate the solenoids. COM (pin 4 of CN5) is utilized as a ground, connecting directly to the ground wire of the eight solenoids. No COM is offered on the relay board that provides +24V to the solenoids, which is why the solenoid's ground is connected to the PSU instead of the relay module. 5V OUT2 and COM (pin 6 and 7 of CN5, respectively) employ a 16AWG DC 5.5mm x 2.1 mm power cable that plugs directly into the Jetson Nanos power jack.

The schematic of the relay module and solenoids are depicted in Figure 9.4. The power supply unit provides 24 V to the relay module via CN1 and CN2. The module has 20 relays, with only eight used for the solenoids. Each relay has two screw terminals: the top one carries the +24 V source to the solenoids (green wire), while the bottom one connects to the solenoid wire (red wire). The solenoids are represented by a white rectangular box with a bow and are numbered 1-8, with A1 and A2 for +V and GND, respectively. The relay module can switch on and off the terminal containing the solenoid wire to control the thrusters. J1 is the female jumper pin header used to control the module. Pins A2-A9 correspond to the relays SD0-SD7, which are linked to each of the eight solenoids. These pins are connected via a jumper wire to eight GPIO pins on the Jetson Nano. The relay module requires 5V to operate, which is supplied by the Nano.

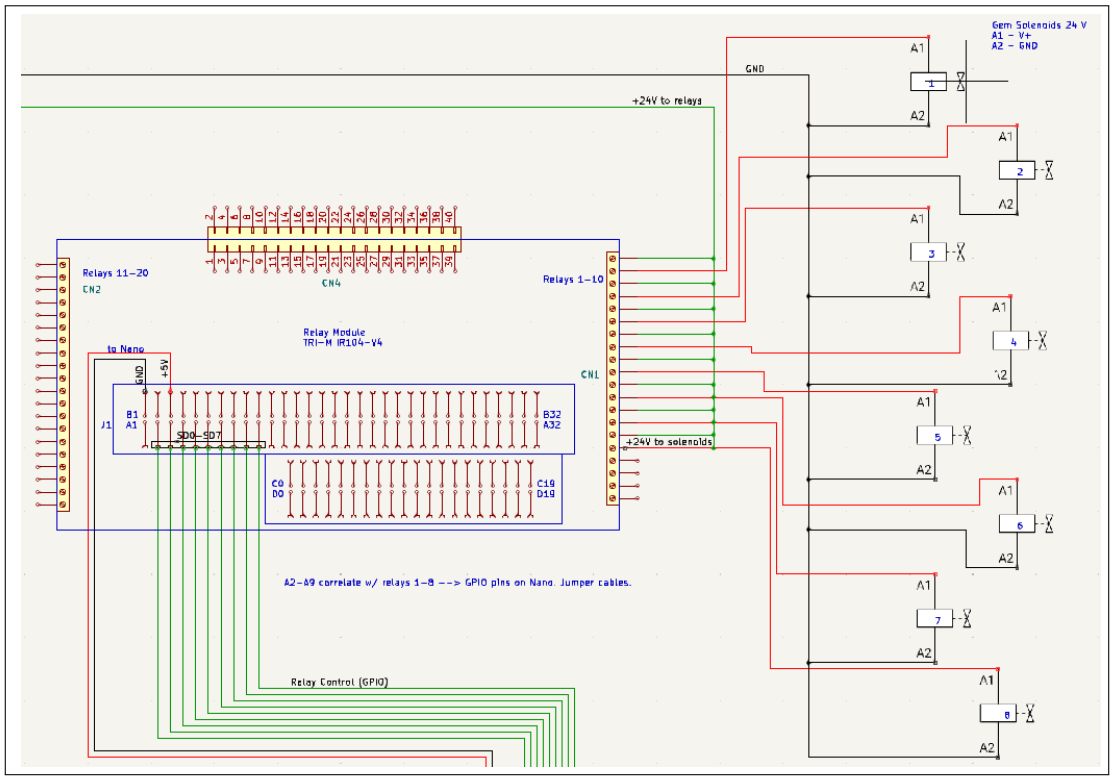

Figure 9.4. Snapshot of relay board and solenoids in KiCad.

The electronic schematic for the reaction wheel's battery, DC voltage regulator, and custom shunt board is illustrated in Figure 9.5. The battery module remains unchanged, except for the addition of SCL, SDA, and BATTID lines that are connected to pins 2, 3, and 4 of the Jetson Nano, respectively. Pin A1 of the battery module supplies +28.8V to the DC voltage regulator through a 20 AWG wire, while A2 provides ground. The regulator reduces the voltage to 18V, which exits the module through screw terminals and is soldered to the posts of the custom shunt board. The current then flows through various electronic components, each labeled with their respective part numbers, before exiting the shunt via a 20 AWG wire and connecting directly to the +18V and 18V RTN pins on the reaction wheel's harness.

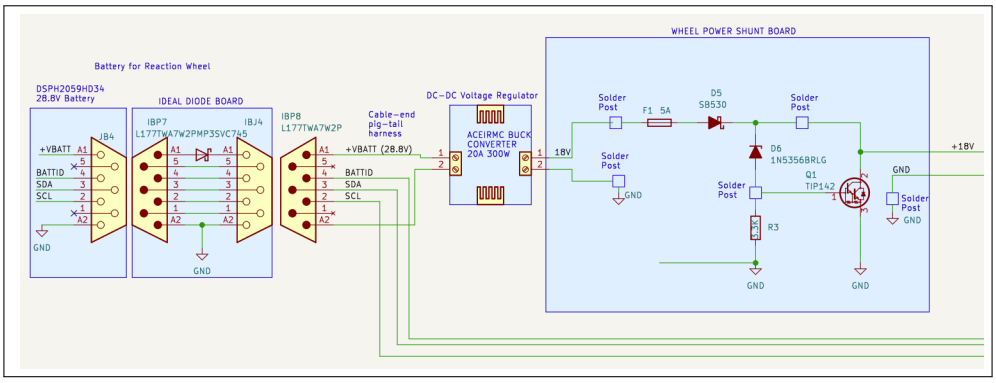

Figure 9.5. Snapshot of the reaction wheel's battery, voltage regulator, and shunt in KiCad.

The electrical connections for the reaction wheel are contained within the DB15 connector (DBHD15F), which is depicted in Figure 9.6. The corresponding pinout can be found in the diagram. The harness consists of two twisted pairs (pins 14/15 and 11/12) and one twisted quad (pins 5, 8, 9, and 10). Twisted cabling is utilized when a group of data-transmitting wires require protection against crosstalk, which is the unwanted noise generated by other nearby wires when current flows through the wire, creating a magnetic field. To eliminate crosstalk, wires can be twisted together to create a cancellation effect on the magnetic fields [54].

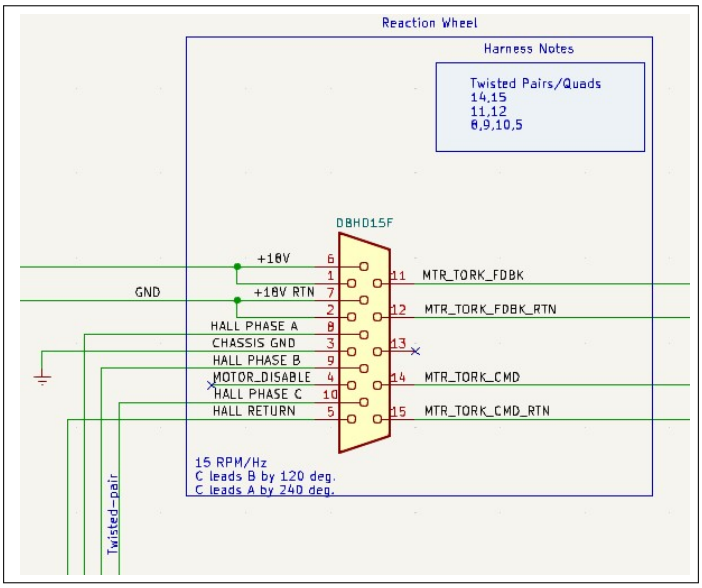

Figure 9.6. Snapshot of the reaction wheel in KiCad.

The twisted pairs contain the command and feedback torque signals. The command signals are wired to the signal conditioning board, while the feedback signals are routed directly to the AD/DA board for conversion to and from the analog signal output by the wheel. The twisted quad contains the hall phase outputs of the wheel, which are routed directly to the AD/DA board. The electronic schematic for the high-precision AD/DA board and custom signal conditioning board is established in Figure 9.7. The hall phases from the reaction wheel interface are attached to pins 5-8, while the feedback torque is connected to pins 12-13 on the screw terminal connector. The custom signal conditioning board does not include any connection interfaces as it is only in the initial stages of its design.

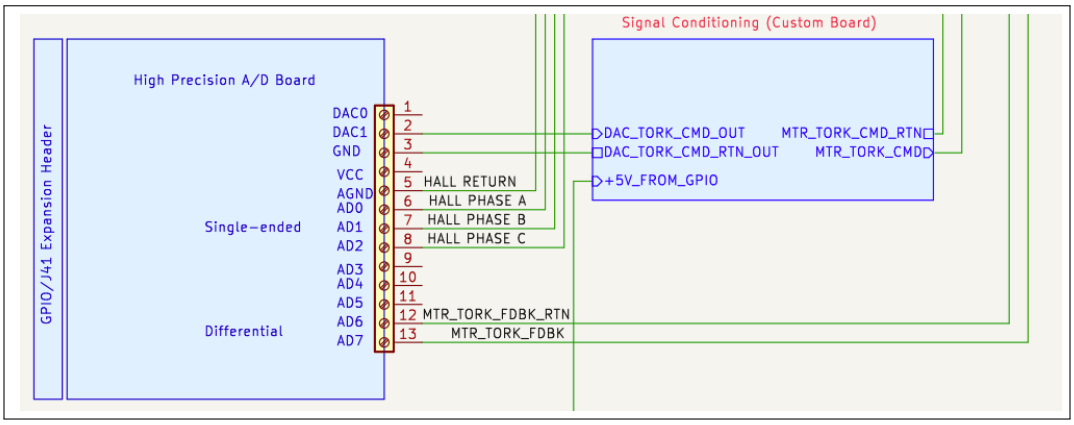

Figure 9.7. Snapshot of the high precision AD/DA board and signal conditioning board in KiCad.

The last electronic subsystem schematic involves the Kinova 7DoF robotic arm, displayed in Figure 9.8. The battery module is again the same as previous the previous modules; the only change is that banana plugs were soldered to the A1 and A2 cub terminals of the 7W2 D-sub connector. A custom power cord was built to span between the 0317 08 circular port at the arm's base to the battery module's banana plugs. Banana plugs allow a simple way to cut power from the robotic arm since an emergency off switch was unable to be implemented. The robotic arm's base also contains an Ethernet port in which the cord bridges to the Jetson Nano, as previously mentioned in this chapter.

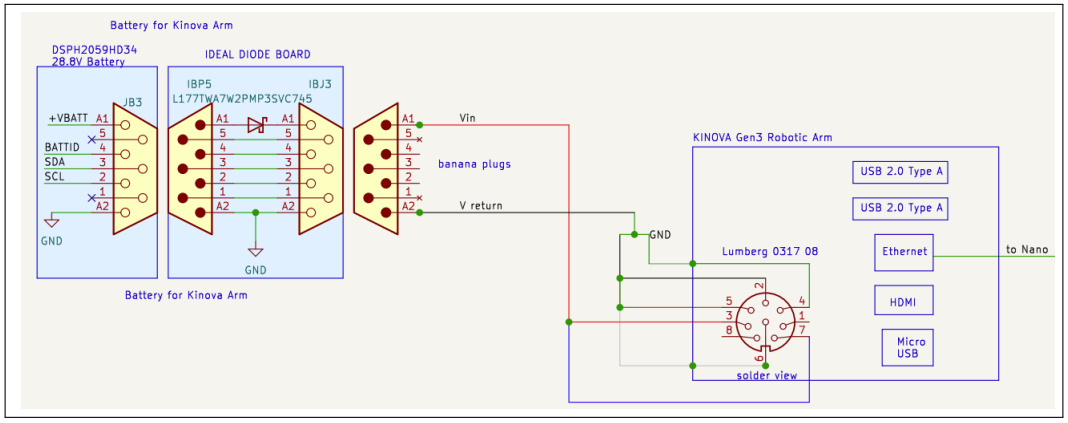

Figure 9.8. Snapshot of the robotic arm and its battery in KiCad.

In summary, the electric schematic software offered by KiCad provides a straightforward way to plan out and document a system's electronic hardware and wiring. Wiring and module pinouts are better visualized and can be referenced when understanding how the various electronic components work together to create an FSS. Assistance with shunt and signal board design was received from Ron Phelps of the SSAG laboratory.

CHAPTER 10:
Results and Discussion

This chapter provides insight into the constructed FSS product and experimentation to test the FSS's operational functions.

10.1 Finalized Construction

The final CAD design, along with the selection of components and numerous system diagrams describing the functioning of the FSS, enabled its successful construction. The bill of materials is included in Appendix B, and a construction manual is included in Appendix C. The manual details the specifics of how to put the FSS together and provides a reference guide for troubleshooting. The manual also serves as documentation for assembling the variety of FSS subsystems, which can be useful for future FSS assembly projects. Both the constructed FSS and the manual only include the components on-hand. There is no integration of the AD/DA board, signal conditioning board, or Wi-Fi router as those components have yet to arrive in the mail. Figure 10.1 displays a picture of the FFS base upon the FSS Developmental Test-Bed in the SRL.

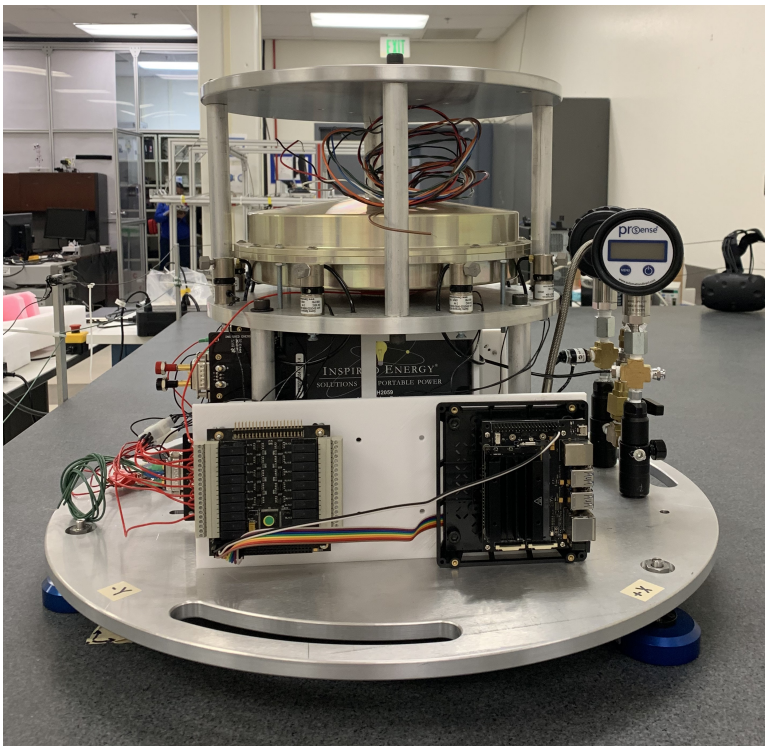

Figure 10.1. Snapshot of the constructed FSS base.

Figure 10.2 shows the complete FSS with the 7 DoF robotic arm mounted to the top.

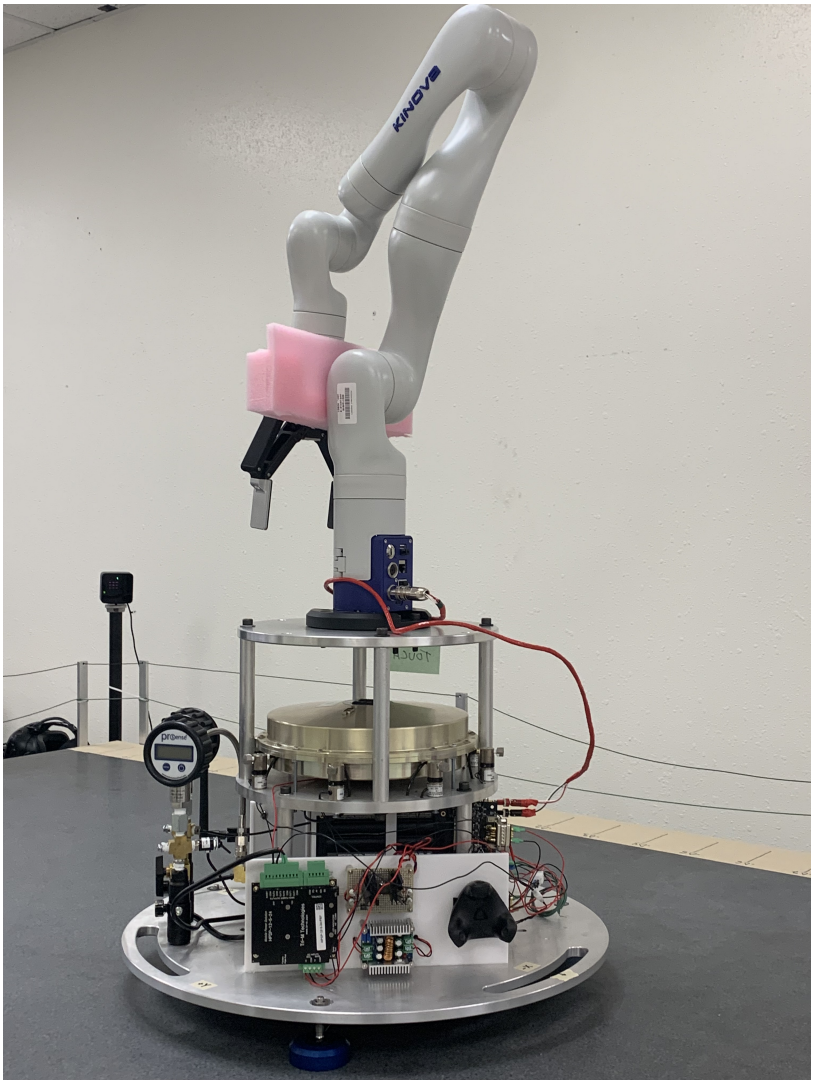

Figure 10.2. Snapshot of the fully constructed FSS.

10.2 Experimentation

With the FSS construction finished, experiments could be conducted to ensure the FSS functions as it should. Unfortunately, testing was severely limited to only the air bearings, thrusters, and robotic arm subsystems due to the absence of hardware and Li-ion battery chargers. Four total scenarios put the constructed FSS through testing on the completed subsystems. Two test scenarios were created to test the pneumatic system, and two test

scenarios were created to test the hardware-in-the-loop of the Robotic arm.

10.2.1 Test Scenarios

While the FSS was constructed, each component, including the electrical cords, was individually tested with the help of a multimeter and a voltmeter to ensure they functioned as promised in their respective user manuals. The pneumatic tests are graded on a pass/fail basis depending on if they perform their function properly, while the robotic arm maneuvers were graded in comparison to the predicted displacement and angular position of the FSS base on ENS Tungett's written control trajectory from his thesis [43].

Test Series 1: FSS Bus with no Robotic Arm Attachment

Test series 1 comprises a series of trials conducted on the FSS bus, a spacecraft component that lacks a robotic arm attachment. The first trial aims to observe whether the air bearings cause the FSS to float on the granite table with minimal friction interference. In the second trial, each of the eight thrusters is individually fired with the air bearings in operation, and the voltmeter provides the voltage required to activate the solenoids. The test series focuses on assessing the functionality of both the air bearings and the thrusters to identify and address any potential issues before the addition of the robotic arm.

Test Series 2: FSS Bus with Robotic Arm Attachment

Test series 2 repeats the same process as Test series 1, with the added robotic arm attachment. This series focuses to ensure the functionality of the air bearings and thrusters is not skewed with the added weight of a robotic arm. The robotic arm remains in a static position during this test.

Test Series 3: Arm Swing Maneuver

Test series 3 comprises three trials of the same maneuver. The arm starts from an initially extended pose, with an angular position of 315° about its first joint. Then it moves +90° to a final angular position of 45°. The thrusters are not fired in this test, but the air to the air bearings is flowing to allow near-frictionless motion. This test series focuses on measuring the displacement and angular position of the FSS's movement in the x and y axis as the arm

maneuvers compared to the calculated values from the control trajectory. A diagram from ENS Tungett's thesis to visualize the test series maneuver is presented in Figure 10.3.

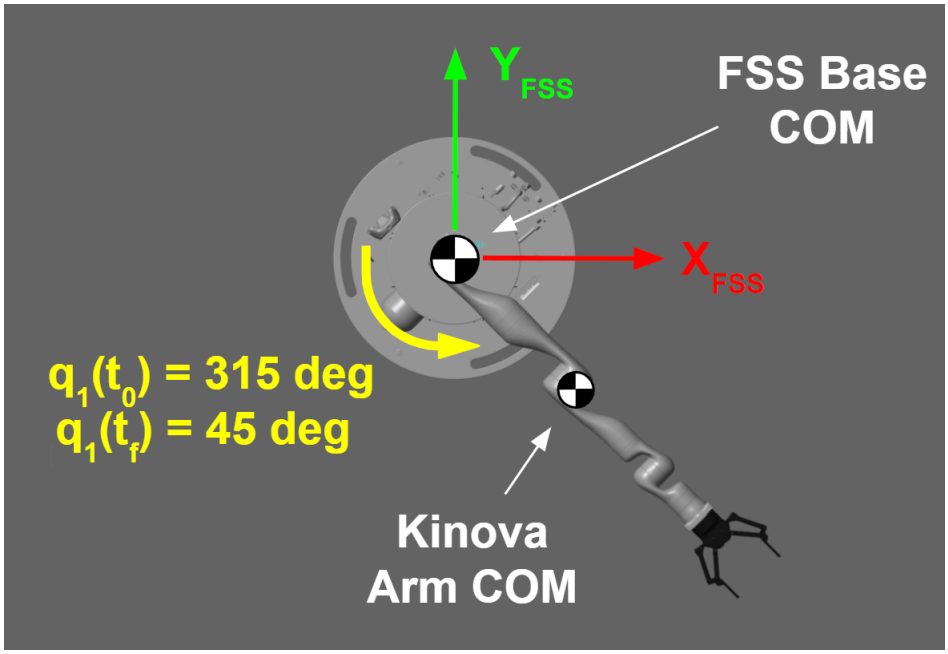

Figure 10.3. Visualization of test series 3. Source: [43].

Test Series 4: Arm Bend Maneuver

Test series 4 follows the arm from an initial zero pose (90° outward) and then moves to an extended pose (0° upward) parallel with the +z axis. The thrusters are again not fired in this test, but the air bearings are activated for near frictionless translational motion in the x and y directions. Measurements are recorded for the displacement and angular position of the FSS's movement. A diagram of the test series maneuver is presented in Figure 10.4 from ENS Tungett's thesis.

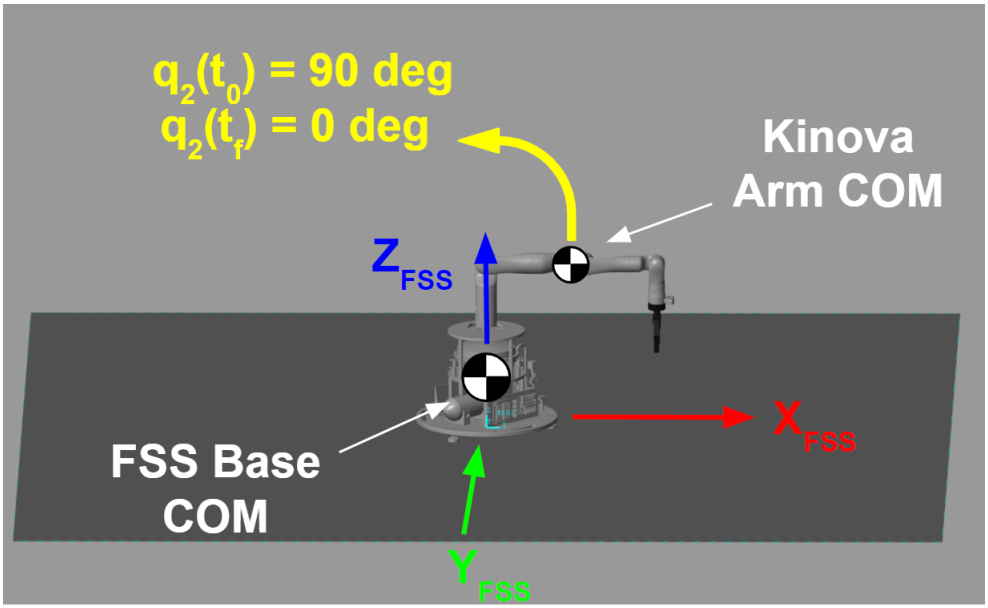

Figure 10.4. Visualization of test series 4. Source: [43].

10.3 Test Scenario Results

The VIVE tracker was intended to be used to track the position and rotation of the FSS against time, but technical difficulties at the time prevented the sensor from being used in this experimentation series. Instead, the position and angular position were manually calculated from a careful measurement scale on the granite table and overhead video footage of the maneuvers. Additionally, the robotic arm required a power cord and ethernet cable that extended beyond the granite test bed as a result of the incomplete Jetson Nano programming and uncharged batteries.

10.3.1 Test Series 1 Results

The results from Test series 1 are laid out below:

- Trial 1 Air Bearing Flotation: Pass
- Trial 2 Thruster Firing:
  - Thruster 1: Pass
  - Thruster 2: Pass

  - Thruster 3: Pass
  - Thruster 4: Pass
  - Thruster 5: Pass
  - Thruster 6: Pass
  - Thruster 7: Pass
  - Thruster 8: Pass

The air bearings supported the weight of the FSS base as predicted and supplied near-frictionless transitional motion in the x and y directions. A minute amount of friction was expected to occur due to an aged finish and imperfections in the granite table's surface. The expectation of the surface is the FSS, when free of exterior forces, should float in place, but when a slight exterior force is applied, the FSS shall move effortlessly in that direction. In this test series, there were noted imperfections in the table's surface, such as dust particles, which caused a cleaning of the surface before the next test series was conducted.

Each thruster was successfully fired. The thrusters were triggered individually for approximately two seconds. The displacement of the FSS base due to the thruster firing was not measured, but each thruster produced approximately the same displacement in the direction of the airflow.

10.3.2 Test Series 2 Results

The pass/fail results from Test Series 2 are presented below:

- Trial 1 Air Bearing Flotation: Pass
- Trial 2 Thruster Firing:
  - Thruster 1: Pass
  - Thruster 2: Pass
  - Thruster 3: Pass
  - Thruster 4: Pass
  - Thruster 5: Pass
  - Thruster 6: Pass
  - Thruster 7: Pass
  - Thruster 8: Pass

There was no visible change in the air bearing's performance due to extra weight once the robotic arm was attached. But, after cleaning and dusting the granite table, the FSS did exhibit smoother, closer to frictionless motion. The thrusters also did not exhibit a noticeable change in performance. Each thruster produced approximately the same displacement in the FSS.

10.3.3 Test Series 3 Results

During the three trials, the displacement and angular position of the FSS was recorded as the arm moved at an extended pose from 315° to 45°, a full + 90° maneuver. The y-axis displacement versus the x-axis was plotted to visualize and compare the calculated displacement predicted by ENS Tungett's control algorithm, and the measured displacement from the trials [43]. The same is done for the angular rotation of the FSS against time. The best resulting trial results my a slim margin are plotted in Figure 10.5.

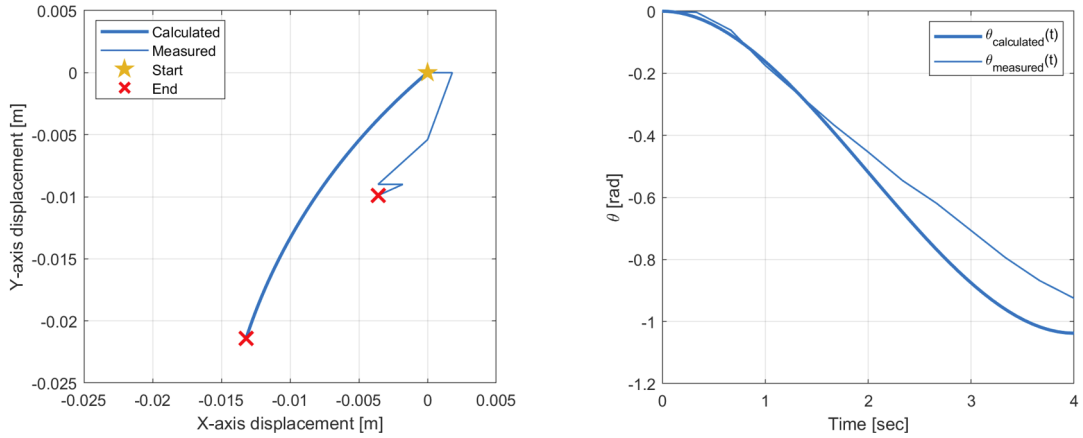

(a) x & y displacement. (b) Angular rotation vs time.

Figure 10.5. FSS test series 3 results.Source: [43].

Figure 10.5(a) appears to showcase a stark difference between the calculated and predicted FSS displacement. The calculated ending point is at [-0.013,-0.022], while the measured is at [-0.004,-0.01]. The FSS does not travel as far as predicted in both the x and y directions. But, the control simulation was developed on the assumption of a completely frictionless granite surface. The SRL's developmental granite table lacks the clean finish to be considered

frictionless and introduces a small amount of friction force on the air bearings. This force prevents the FSS from traveling far in a completely smooth motion. The table is also not precisely leveled, so there is a slight "downhill" direction. The jagged, short line of the measured displacement is only 0.009 meters off in the x direction, and 0.012 meters off in the y direction, a small disparity for the overall size of the FSS and insignificant as the focus of this test series was more to measure the rotation of the FSS base in response to the robotic arm maneuvering. The translation measured was very small and nearly outside the range of detection from the camera footage, which only has a spatial resolution of 0.1 mm per pixel.

Figure 10.5(b) demonstrates a close resemblance between the calculated and measured angular displacement. The arm was rotated 180° clockwise but due to the near-frictionless surface the FSS sits upon and conservation of angular momentum, the FSS itself rotates in the opposite direction. A torque was applied to the system in the +z direction, and in response, the base will experience an equal and opposite torque. Again, because the granite table is not completely frictionless, some momentum is lost. The angular rotation of the calculated scenario was -1.05 radians or approximately -60°. The angular rotation of the measured trial was -0.92 radians or approximately -53°. This represents a difference of 7°, an accepted level of agreement between calculated and measured results.

Figure 10.6 provides an overhead view of the FSS arm swing maneuver in its final extended pose.

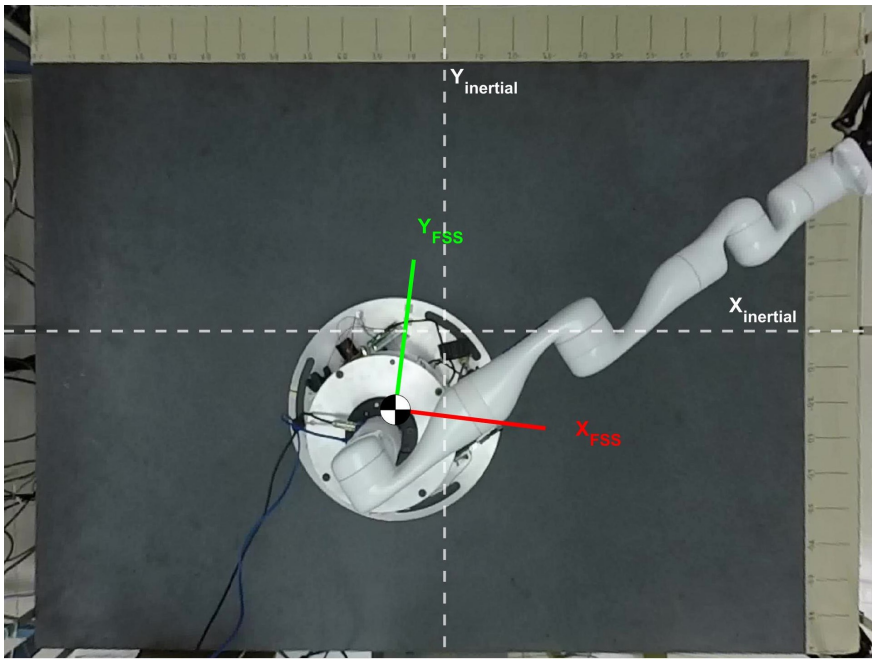

Figure 10.6. Overhead snapshot of test series 3 in final pose.

10.3.4 Test Series 4 Results

During the three trials, the displacement and angular position of the FSS was recorded as the arm moved from a zero pose to a vertically extended pose. To compare the calculated displacement predicted by ENS Tungett's control algorithm with the measured displacement from the trials, a graph was plotted showing the x and y displacement [43]. Similarly, a graph was plotted for the angular rotation of the FSS over time. The results from the most successful trial were plotted in Figure 10.7. Other trials produced similar results but with additional noise.

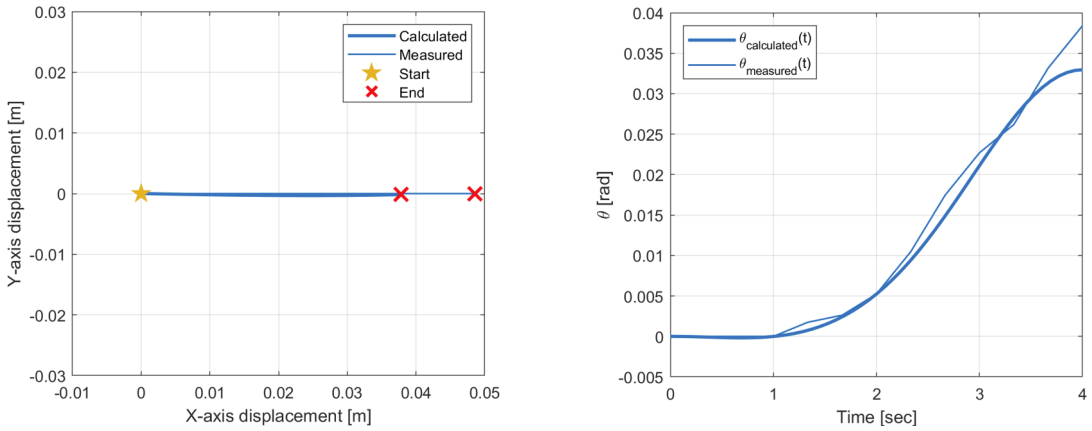

(a) x & y displacement.

(b) Angular displacement vs time.

Figure 10.7. FSS test series 4 results. Source: [43].

Figure 10.7(a) displays a similarity between the calculated and measured displacement. The final x coordinate of the calculated is approximately 0.038 meters, while the measurement is approximately 0.049 meters. There is practically no displacement in the y direction, as the robotic arm is moving normally to that axis. The disparity between the two displacement values in the x-axis can be derived from the jerky movement of the arm. Within the control simulation, all arm movement is completely smooth, but in reality, the arm lurches on movement initiation, causing supplementary movement to the FSS base. Nevertheless, the 0.011 meter error between the calculated and measured trajectory is within acceptable limits.

Figure 10.7(b) presents a close likeness between the calculated and measured angular displacements. The measured curve exhibits less of a fluid curve than the calculated, but that is to be expected in real-world test scenarios in comparison to computer simulations. The final calculated angular displacement was 0.0358 radians, approximately 2°, and the final measured was 0.033 radians, approximately 1.9°. The ideal scenario with a perfectly lined up center of mass of the FSS base and robotic arm would produce an angular displacement of zero degrees. But, the COM of the FSS base is not perfectly lined up on a single axis, so a slight torque from the arm's movement is induced on the FSS base, causing a slight rotation around the +z axis. The level of consistency between the calculated and measured angular displacement scenarios is exhibited in a 0.1° difference.

Figure 10.8 provides an overhead view of the FSS arm bend maneuver in its initial extended pose.

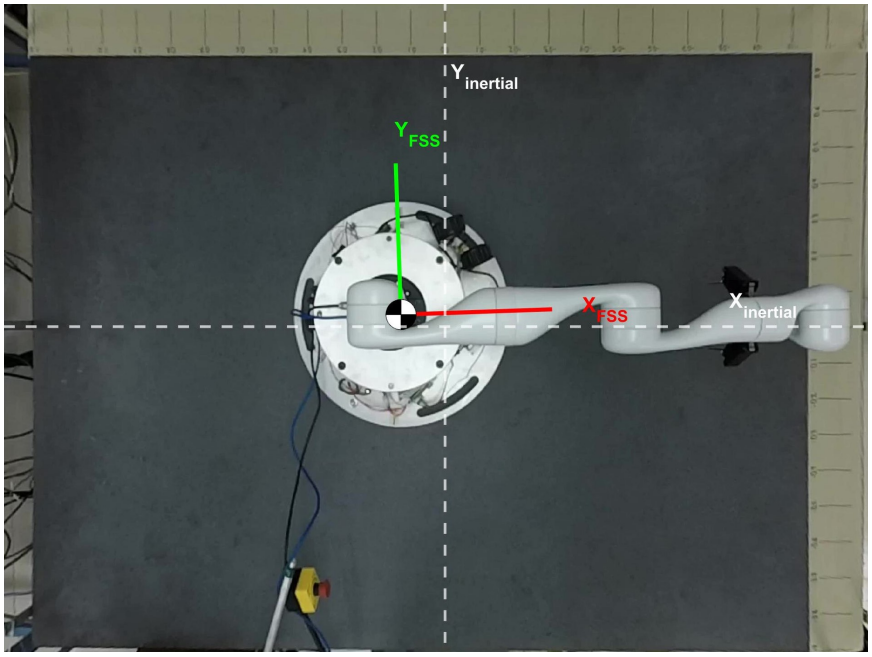

Figure 10.8. Overhead snapshot of test series 4 in initial pose, before maneuver.

In conclusion, the results of the four test series are positive and demonstrate progress toward achieving the goal of a fully completed, wireless FSS with a complementary control trajectory model. While the outcomes of the tests were acceptable, there is potential for further improvement in accuracy by relocating the FSS to the POSEIDYN testbed at the SRL, which provides a granite table with a superior near-frictionless finish compared to the developmental test bed used in the current test series. Such an upgrade may be necessary to validate the completed FSS's performance.

CHAPTER 11: Conclusion

11.1 Summary of Work

An understanding of how FSS subsystems typically function was achieved via a study of the initial FSS CAD design and through reverse engineering of both the initial design and previous FSS models. Unfortunately, there was not much prior documentation on the construction of the previous FSSs, so many design considerations were made just by analyzing what was visible in the working FSSs. While this was helpful for the pneumatic subsystems, it was no help for the electronic subsystems of this FSS, as each FSS is made with a different purpose in mind. The electronic components used in the initial CAD design provided a starting point, but all the of electronic subsystem design was completed via extensive hours of research. Once an understanding of how the FSS would generically function was established, research into FSS modifications of its optimization, which included component improvements and additions, was completed.

A final design was created by applying the knowledge attained from current FSSa and extensive research into each component . A supporting final CAD design was created in Siemens NX CAD software with system diagrams fabricated with KiCad and Magic Systems of Systems software. The chosen parts for the final FSS design were either provided by the SRL, ordered online, or fabricated in-house. The FSS was then constructed with the available parts to include the 7 DoF robotic arm. Pictures and detailed diagrams of its construction are included in an accompanying assembly guide to ensure future FSS productions can be less challenging.

The constructed FSS was placed through a testing series to test the functioning subsystems. Due to time constraints, not all subsystems of the FSS are functioning completely. Some complementary parts of the reaction wheel are still outstanding, so the wheel failed to operate by the end of this thesis. But, the air bearing, thruster, and robotic arm subsystems are functional and passed their respective testing series. Near frictionless motion from the air bearings was achieved, each of the eight thrusters were successfully fired, and the measured

displacement and rotation of the FSS base resulting from the robotic arm's movements closely resembled the predicted values from the complementary FSS control trajectory.

11.2 Future Work

11.2.1 Finishing the FSS Assembly

Although the design of the FSS is complete, several steps need to be taken before the spacecraft can become fully operational. In the future, the first step will be to set up and update the Jetson Nano and install the necessary WiFi router driver to allow wireless interaction with the Nano. Once this is done, the AD/DA board will need to be integrated into the reaction wheel's subsystem. Although the signal conditioning board has already been designed, it is necessary to order the remaining parts and construct the board. Once all of the components are received and the board is constructed, the construction manual will need to be updated to reflect the current build. By completing these steps, the FSS is a step closer to becoming fully operational.

11.2.2 Programming the Jetson Nano

Programming is the last step required to enable wireless control and monitoring of the FSS. To achieve this, a series of Python scripts will need to be developed to control the spacecraft's thrusters and reaction wheel, monitor the reaction wheel's battery level, and interface with the Kinova robotic arm. These scripts will need to be designed and tested to ensure that they operate seamlessly and reliably for FSS experiments. Once the programming is complete, the FSS spacecraft will be able to operate completely wirelessly, making it a more capable and effective platform for a range of robotic arm-capturing experiments aboard a floating spacecraft.

11.3 Research Significance

The significance of this research lies primarily in the implementation of a 7 DoF robotic arm onto an FSS. The SRL has previously designed FSSs, but none have been of this size nor have they included a 7 DoF robotic arm. The inclusion of this arm is significant as it allows for a broader range of motion and greater flexibility in the execution of experiments.

Through the integration of the FSS and 7 DoF robotic arm, this research presents a novel and innovative approach to space robotics experimentation, which has applications in areas such as multi-body robotic kinematics and dynamics, in-orbit servicing, and debris removal. The FSS is significant as it provides an opportunity to demonstrate the effectiveness of ground test facilities paired with spacecraft simulators as the foundation and future of robotic on-orbit servicing. Ultimately, this research has the potential to advance our understanding and capabilities in using robotic arms aboard spacecraft.

THIS PAGE INTENTIONALLY LEFT BLANK

APPENDIX A:
FSS KiCad Schematic

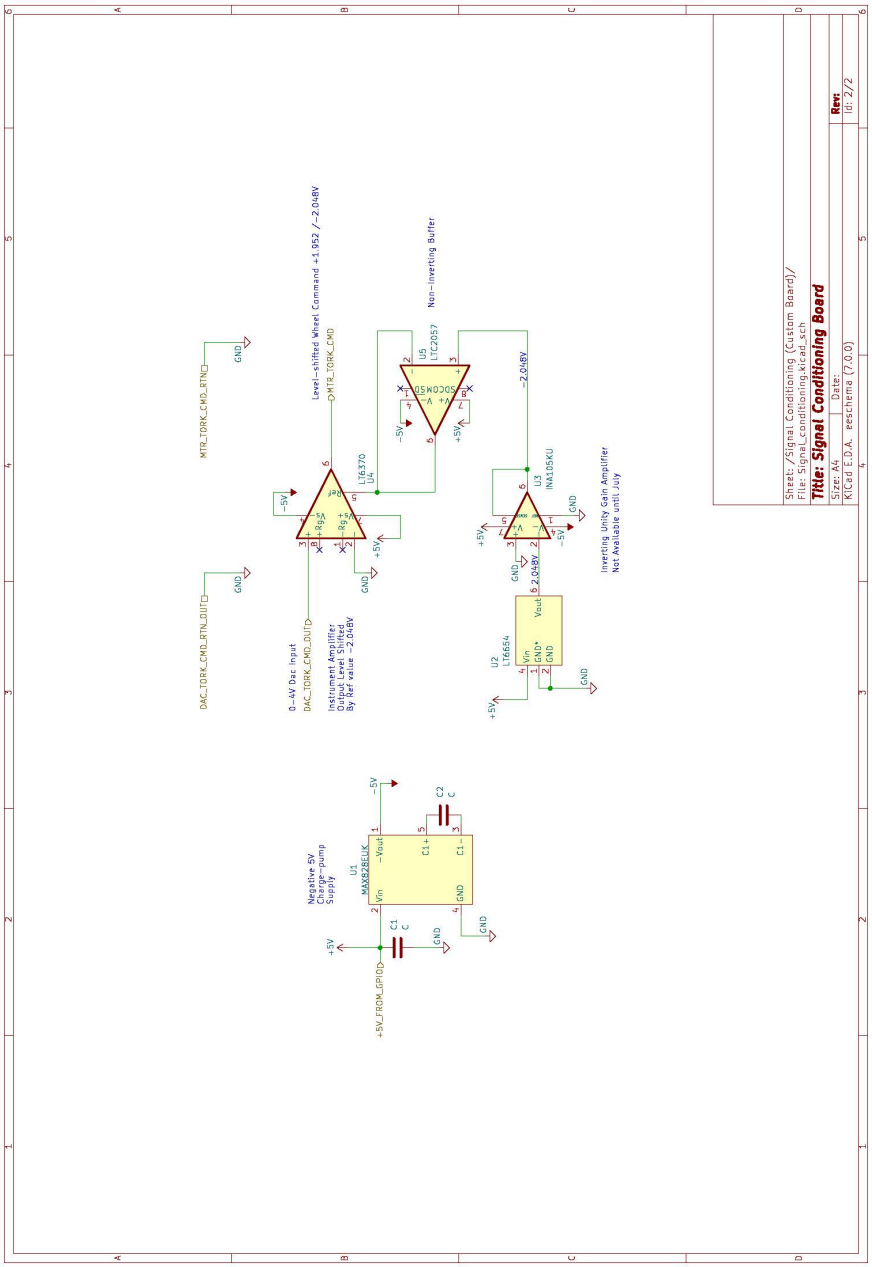

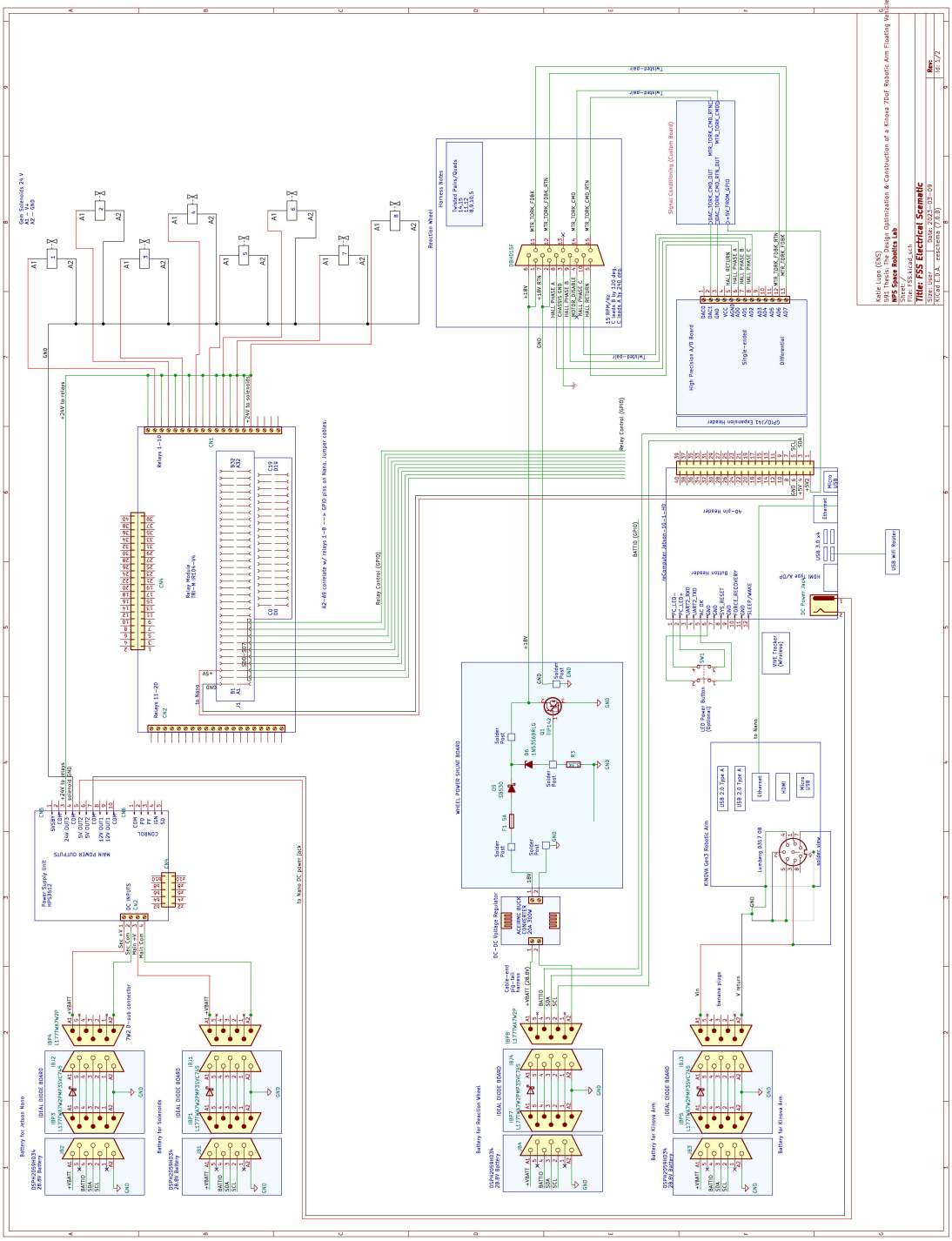

APPENDIX B:
FSS Bill of Materials

Type	Part #	Part	Brand	Quantity
Pneumatics	S105001	65mm Flat Round Air Bearing	New Way	3
	S8013B06	13mm Diameter / M10x.75 x 54mm lg Ball Mounting Screws Round End	New Way	3
	S8013S01	13mm Ball Retaining Clips	New Way	3
	5058K946	Aluminum Low-Pressure Barbed Tube Fitting for Air and Water, Adapter, 1/16" Tube, M5 x 0.80mm Male	Mcmaster	3
	DPG1-200	DPG1 Series Digital Pressure Gauges	Automation Direct	2
	62475K14	Air Directional Control Valve, with Hand Return, 1/8 NPT Male x 10-32 UNF Female	Mcmaster-Carr	1
	6543k72	Open-Flow Quick-Disconnect Hose Coupling for Air and Water, Quick-Disconnect 1/8" Plug x 1/8" NPTF Male | McMaster-Carr	Mcmaster-Carr	4
	6543k62	Open-Flow Quick-Disconnect Hose Coupling for Air and Water, Quick-Disconnect 1/8" Sleeve-Lock Socket x 1/8" NPTF Male | McMaster-Carr	Mcmaster-Carr	2
	5232T347	Precision Extreme-Pressure Steel Pipe Fitting, Reducing Adapter, 1/4 NPT Female x 1/8 NPT Male | McMaster-Carr	Mcmaster-Carr	2
	50745K14	Brass High-Pressure Barbed Tube Adapter, for Air and Water, for 1/16" Tube ID x 1/8 NPT Male | McMaster-Carr	Mcmaster-Carr	3
	50785K232	High-Pressure Brass Pipe Fitting, Cross Conne	Mcmaster-Carr	3
	4118T111	Panel-Mount On/Off Valve, Brass Body, Straig	Mcmaster-Carr	1
	50785K35	High-Pressure Brass Pipe Fitting, 90 Degree E	Mcmaster-Carr	1
	5230T312	Precision Extreme-Pressure Steel Pipe Fitting,	Mcmaster-Carr	5
	NINJAREG45KUL	Ninja Ultralite Adjustable Tank Regulator - 45	Ninja Paintball	1
	FITT042N	10-32 tapered thread barb to 1/16 ID tube	Palmers Pursuit Shop	9
	FITT017	1/8 NPT Female TEE	Palmers Pursuit Shop	2
	PPSP015	Fatty Stabilizer CO2 Air Pneumatic Regulator Up to 4500 psi input Adjustable 1-400 psi output	Palmers Pursuit Shop	2
	FITT066	1/8 NPT Push Button Bleeder Valve	Palmers Pursuit Shop	2
	012_056 NPTAB	Custom air nozzle	-	8
	5463K43	Plastic Barbed Tube Fitting for Air and Water, Tight-Seal, Tee Connector, for 1/16" Tube ID (Sold in pk of 10)	Mcmaster-Carr	4
	HOSE-SS-MESH-12	12" Flexible metal tubing	Mcmaster-Carr	1
	HOSE-SS-MESH-8	8.5" Flexible metal tubing	Mcmaster-Carr	1
	-	Ninja SL2 Air Tank (4500 psi, 45 in3)	Ninja Paintball	1
	PPSP983	Aluminum .825x14 Threads to female 1/8 NPT	Palmers Pursuit Shop	3
	1A-157-01	Plastic tubing	Freelin-wade	500ft

Electronics	0322 08	Lumberg - 0322 08 - Connector	RS Americas	1
	PH2059HD34	P-Series Battery: 28.8V 3.4Ah	Inspired Energy	4
	EB429	Ideal Diode board for P Series batteries	Inspired Energy	4
	699014	Flying Lead convertion kit	Inspired Energy	4
	699012	P-Series Backshell for 699013 (Male) and 619	Inspired Energy	4
	PH1000	1-Bay, P-series, Charger/Calibrator	Inspired Energy	1
	713-102110417	Development Boards & Kits - ARM NVIDIA Jetson Nano Development Kit-B01	Mouser Electronics	1
	HPS3524	TRI-M HPSP PC/104 Power Supply Out 12V, 5	Tri-M Technologies	1
	-	HTC VIVE Virtual Reality System Tracker 3.0	HTC Corperation	1
	-	Reaction Wheel	Ball Aerospace	1
	FA-T220-51E-ND	Heatsink	Digi-Key	1
	-	Step Down Module Adjustable DC 6-40V to 1.2-36V Voltage Regulator Buck Converter	Aceirmc	1
	11010	Raspberry Pi High-Precision AD/DA Expansion Board	Waveshare	1
	1N5355B-TP	Diode Zener 18V 5W DO15	Digi-Key	1
	IR104	PC/104 Industrial Relay Module	Tri-M Technologies	1
	-	Jetson Nano WiFi Adapter Dual Band Wireless USB 3.0 Adapter 5GHz and 2.4GHz 1200Mbps Network Card	Geekworm	1
	-	3FT 12V DC Power Cable	Amazon	1
	-	Braided Ground Strap Tinned Copper Flat Sleeving Expandable Metal Sheath Screening Signal Wire Cable Shielded	Amazon	1
	-	12mm Chassis Switch Metal Button Switch with 22inchs Extension Cable	Amazon	1
	-	Wire Male to Female Breadboard Jumper Wires 11.8 inch 120pcs	Amazon	1
	-	Gen3 Ultra lightweight robot 7 DoF	Kinova	1
	2F-140	Adaptive Robot Gripper	Robotiq	1
	SB530	Schottky Diode	Mouser Electronics	1
	1N5356BRLG	Zener Diode	RS Americas	1
	TIP142	Darlington Transistor	STMicroelectronics	1
	INA105KU	Inverting Unity Gain Amplifier	Mouser Electronics	1
	MAX828EUK	Switching Voltage Regulators Switched-Capac	Mouser Electronics	1
	LTC2057	Low Noise Zero-Drift Operational Amplifier	Analog Devices	1
	LT6370	Low Noise Instrumentation Amplifier	Analog Devices	1
Structural	P312T6	1/2" thick 6061-T651 Aluminum Plate 24in x 24in	Metals Depot	2
	P534	3/4" (.750) thick T304 Stainless Steel Plate - Dull Mill Finish, 24in x 24in	Metals Depot	1
	R334	3/4 inch Dia. 6061-T6511 Aluminum Round-Cut to size 3ft	Metals Depot	2

APPENDIX C:
FSS Assembly Guide

Step 1:

Create the following 3D printed parts using an FDM printer (Fortus printer at the Space Systems Academic Group Lab).

- air tank supports – 2x (Fig. 1)
- battery holders – 2x (Fig. 2)
- side supports – 2x (Fig. 3)

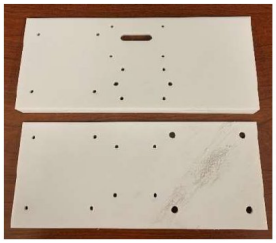

Fig. 1

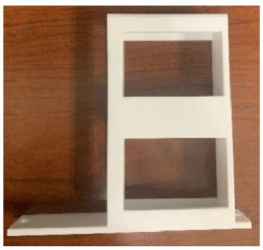

Fig. 2

Fig. 3

Step 2:

Print 8x air nozzles on a powder bed printer with titanium alloy (Ti64). Figs. 4 & 5 contain pictures of a nozzle.

Fig. 4

Fig. 5

Step 3:

Utilize a machine shop to create:

- bottom plate – 1x (Fig. 6 left)
- middle plate – 1x (Fig. 6 middle)
- top plate – 1x (Fig. 6 right)
- standoffs – 8x (Fig. 7)

Fig. 6

Fig. 7

Step 4:

First, acquire all items in Fig. 8 below.

- 65 mm (or 50 mm) flat round air bearings – 3x
- ball mounting screws –3x
- ball retainers (and small screws) –3x
- 10-32 tapered thread barb to 1/16 ID tubes –3x

Take the ball mounting screw and place the spherical end into its place in the top center of the air bearings. Place the black ball retainer on top of the ball screw in a way that the sphere is still free to rotate but cannot be separated from the air bearing. Use the three small screws to secure the ball retainer in place. Configuration should appear as in Fig. 9.

Take the threaded barb and apply a small amount of Teflon tape to its threads in a clockwise direction, and then screw into the 10-32 threaded hole on the side of the air bearing as in Fig. 9.

Fig. 8

Fig. 9

Step 5:

First, acquire all items in Fig. 10 below.

- EMPTY Ninja SL2 Air Tank (4500 psi, 45 in3) – 1x
- Ninja Ultralite Adjustable Tank Regulator 4500 PSI (may already be connected to tank) –1x
- Aluminum .825x14 Threads to female 1/8 NPT – 1x
- 12" Flexible metal tubing – 1x
- Open-Flow Quick-Disconnect Hose Coupling for Air and Water, Quick-Disconnect 1/8" Plug x 1/8" NPTF Male –2x
- Open-Flow Quick-Disconnect Hose Coupling for Air and Water, Quick-Disconnect 1/8" Sleeve-Lock Socket x 1/8" NPTF Female – x2 (OR replacement Threaded Brass Pipe Straight Connector, 1/8 NPTF Female + Quick-Disconnect 1/8" Sleeve-Lock Socket x 1/8" NPTF Male)—1x
- Panel-Mount On/Off Valve, Brass Body, Straight, 1/8 NPT Female x 1/8 NPT Male – 1x
- High-Pressure Brass Pipe Fitting, 90 Degree Elbow Connector, 1/8 NPT Female – 1x
- Precision Extreme-Pressure Steel Pipe Fitting, Straight Connector, 1/8 NPT – 3x
- 1/8 NPT Female TEE – 1x

Fig. 10

Apply Teflon tape to all threads except the black connecter (Aluminum .825x14 Threads to female 1/8 NPT) screwed directly to the regulator on the tank. Configure the connections on the side of the hose closest to the air tank as in Figure 11. Screw all pieces together; using a wrench when necessary.

Fig. 11

On the other side of the hose, configure the pieces as in Fig. 12, and connect.

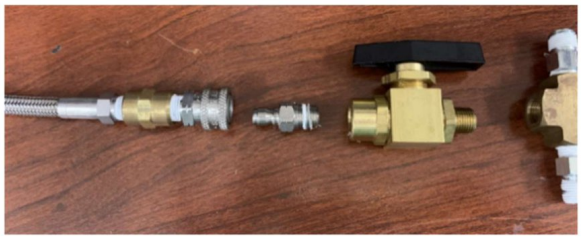

Fig. 12

Once connected, the assembly should appear as in Fig. 13.

Fig. 13

Step 6:

To attach a tank filler hose (which is optional), gather the parts:

- Open-Flow Quick-Disconnect Hose Coupling for Air and Water, Quick-Disconnect 1/8" Plug x 1/8" NPTF Male –2x
- 1/8 NPT Female TEE – 1x
- 8.5" Flexible metal tubing—1x
- Open-Flow Quick-Disconnect Hose Coupling for Air and Water, Quick-Disconnect 1/8" Sleeve-Lock Socket x 1/8" NPTF Female – 2x
    a. (OR replacement Threaded Brass Pipe Straight Connector, 1/8 NPTF Female + Quick-Disconnect 1/8" Sleeve-Lock Socket x 1/8" NPTF Male)

Set up the hose configurations as they appear in Fig. 14 & Fig. 15.

Fig. 14

Fig. 15

The fully assembles hose is pictured in Fig. 16.

Fig. 16

One end of the hose is connected to the tank regulator as in Fig. 17. Set assembly aside for the moment.

Fig. 17

Step 7:

Gather the parts to fit together as in the layout in Fig. 18. Apply Teflon tape to all appropriate areas.

- Air Directional Control Valve, with Hand Return, 1/8 NPT Male x 10-32 UNF Female –1x
- DPG1 Series Digital Pressure Gauges –2x
- Precision Extreme-Pressure Steel Pipe Fitting, Reducing Adapter, 1/4 NPT Female x 1/8 NPT Male – 2x
- Brass High-Pressure Barbed Tube Adapter, for Air and Water, for 1/16" Tube ID x 1/8 NPT Male –1x
- High-Pressure Brass Pipe Fitting, Cross Connector, 1/8 NPT Female – 2x
- Precision Extreme-Pressure Steel Pipe Fitting, Straight Connector, 1/8 NPT Male – 2x
- Fatty Stabilizer CO2 Air Pneumatic Regulator Up to 4500 psi input Adjustable 1-400 psi output – 2x
- 1/8 NPT Push Button Bleeder Valve –2x
- Aluminum .825x14 Threads to female 1/8 NPT –2x

Fig. 18

The configuration on the left side of Fig. 19 is for the solenoid values. A closer glance at the parts screwed together is provided. Ensure that the miniature pressure gauge on the fatty stabilizer is facing the opposite direction of the high-pressure barbed tube adapter.

Fig. 19

The right side of the assembly in Fig. 20 is for the air bearings. The air directional control value is used to shut the air supply to the air bearings on and off. Screw in the small barbed tube adapter that came with the control valve kit, adding a small amount of Teflon tape.

Fig. 20

Screw all pieces together, using a wrench when necessary. Ensure the stabilizer's small pressure sensor is facing away from the control value, as seen in Fig. 21.

Fig. 21

Screw the two digital pressure gauges to the top of each assembly. The right-side air-bearing assembly should appear similar to Fig. 22, with the left-side solenoid assembly appearing similar to Fig. 23.

Fig. 22

Fig. 23

Step 8:

Acquire the following parts of pictures Fig. 24:

- 10-32 tapered thread barb to 1/16 ID tube –8x
- Gems Sensors: 2-Way sub-miniature solenoid valve – 8x
- 3D printed nozzles from Step X – 8x

Apply Teflon tape to the threaded barbs and the nozzles and screw them into the threaded hole labeled “IN”. Screw the nozzles into the hole labeled “OUT”. Fig. 25 displays an assembled solenoid.

Fig. 24

Fig. 25

Step 9:

Acquire the following pieces:

- Base plate
- Standoffs – 4x
- Battery supports – 2x
- Assembled air bearings – 3x
- Assembled pieces with fatty stabilizers from step X.
- M8 bolts – 8x
- M8 nuts – 4x
- M8 washers – 4x

Fig. 26 provides a map that outlines where each piece is attached to the base plate.

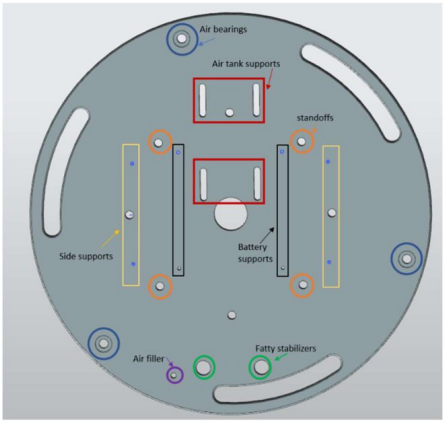

Fig. 26

Begin with the three air bearings, screwing them tightly to their places outlines with blue circles on the map in Fig. 27. It will be helpful in future steps to orient the bearings so that the threaded barbs on their side are facing inward to the plate.

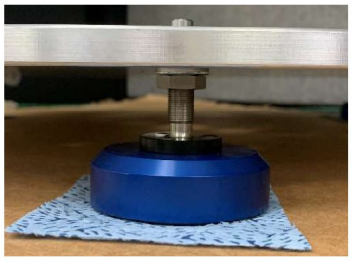

Fig. 27

Once the base plate is supported by the three air bearings, attach the four standoffs, two battery holders, and two air tank holders as so provided by the map. The metal standoffs are attached to the bottom plate using only a bolt and washer since there are already M8 threads machined into the rods. When finished the configuration should appear as in Fig. 28.

Fig. 28

Screw the assembly from step 5 to the fatty stabilizer assembly from step 8. Ensure the threads are all screwed in tightly, and the fatty stabilizers are parallel to each other and upright. This will allow them to be placed snuggly in the holes outlined in green in Fig. 26. Fig. 29 displays how the final configuration of the assemblies appears.

Fig. 29

Step 9:

Acquire the following parts in Fig. 30:

- Three-way tube connector – 5x
- Polyurethane Tubing
  - ~1-inch cuts – 4x
  - ~10-inch cuts – 4x

Fig. 30

First, assemble a circle using the four pieces of short plastic tubing and the four connectors as in Fig. 31. This will help supply the air bearings with pressurized air.

Fig. 31

Attach three of the long plastic tubes to the threaded barbs on the side of the air bearings under the base plate. Attach each other end of the tubing to a connector on the circle assembly just created. One of the connectors should remain free. Pull up the tubing connected to the air bearings through the hole in the middle of the base plate as in Fig. 32.

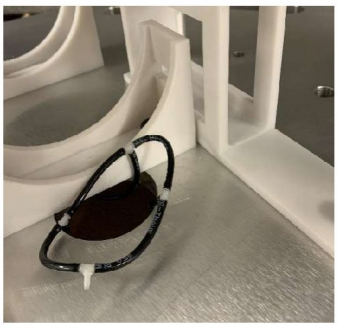

Fig. 32

Ensure all tube connections are still tight and not touching the ground under the plate. Take the last plastic tube and connect one end to the remaining three-way connector on the circle, and the other end to the threaded barb on the control valve from step 7. Fig. 33 displays the connection.

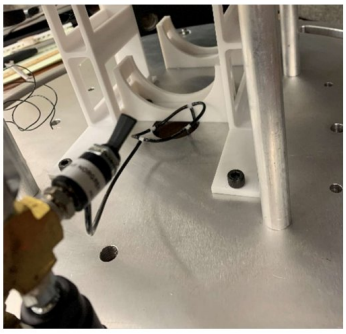

Fig. 33

Step 10:

Acquire the following pieces:

- Middle plate
- Standoffs – 4x
- Assembled solenoids –8x
- M8 bolts –8x
- M8 washers – 4x
- 10-32 x 1 inch screws – 8x

Fig. 34 provides a map that outlines where each piece is attached to the middle plate. Follow the map to attach the middle plate to the standoffs from the base plate, and attach new standoffs to be used between the middle and top plates.

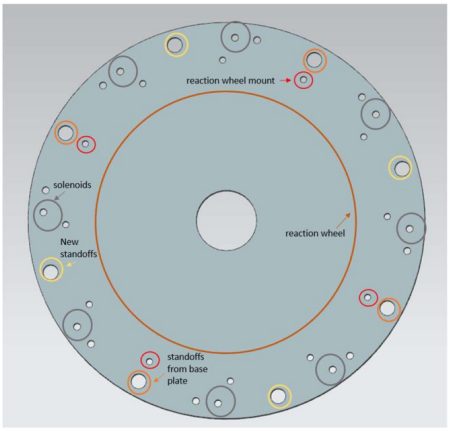

Fig. 34

Attach the solenoids to the middle plate with the 10-32x1 inch screws. Space out the solenoids around the plate as equally as possible, with the nozzle facing perpendicular to the edge of the plate. Fig. 35 is an example.

Fig. 35

The assembly with all the standoffs and solenoids secured appears in Fig. 36.

Fig. 36

Step 11:

Acquire the following pieces:

- Tape
- Three-way tube connector –1x
- Six-way tube connector – 2x
- Polyurethane Tubing
    - ~1.5-inch cut – 2x
    - ~3-inch cut – 1x
        - ~10-inch cut –9x

Create the assembly shown in Fig. 37 with the three tube connectors and the 1.5-inch & 3-inch cut tubes. Secure the circle to the bottom of the middle plate as in Fig. 38.

Fig. 37

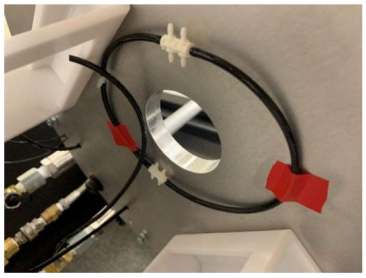

Fig. 38

Use the 10-inch tubes to create connections between each solenoid and each open connector on the circular tube assembly under the middle plate. Slide the tubing through the small holes next to the solenoids in the middle plate to provide room to place the reaction wheel. The bottom of the middle plate is pictured for reference in Fig. 39.

Fig. 39

Connect one end of the circle assembly to the threaded barb as in Fig. 40 using the last 10-inch tube. This connects the air source to each thruster.

Fig. 40

Step 12:

Acquire the following pieces:

- Reaction wheel
- 10-32 x 3-inch screws – 4x
- 10-32 nuts – 8x
- Top plate
- M8 bolts – 4x
- M8 washer – 4x

Secure the reaction wheel to the middle plate. There are a variety of ways to secure the wheel to the middle plate, and this way uses the 10-32 x 3-inch screws with a nut to support the reaction wheel's weight and a nut under the middle plate to secure the screw in place. Fig. 41 displays how the screws and nuts are utilized to secure the wheel.

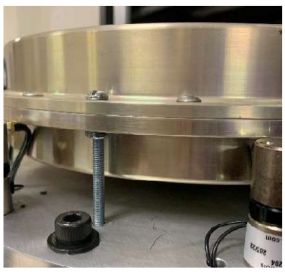

Fig. 41

Place the top plate upon the top of the standoff and secure it with M8 bolts and washers as in Fig. 42.

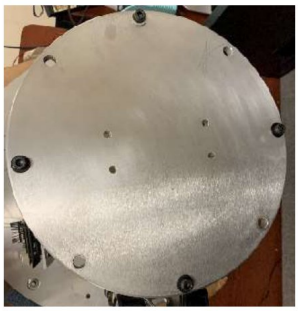

Fig. 42

Step 13:

The Kinova arm does not come with a power cord that plugs into a portable battery, so one must be handmade. The Kinova Robotic Arm user manual provides details on the cord.

Acquire the following pieces:

- Lumberg connector kit
- 20 AWG electrical wire ~ 1 meter – 6x
- Electrical tape
- Copper shielding wire ~ 1 meter
- Banana plug male – 2x
- Banana plug jack – 2x
- Large solder cup connectors from Ideal Diode pack – 2x

The lumber connector is provided de-assembled in Fig. 43.

Fig. 43

Following the pinout map provided in the Kinova manual and Fig. 44, solder the 6 wires to the connector cups as in Fig. 45. Note that the view provided in Fig. 44 is the plug view; the solder view is the mirror image. Make sure to keep track of which wire by labeling with color, tape, or Sharpie.

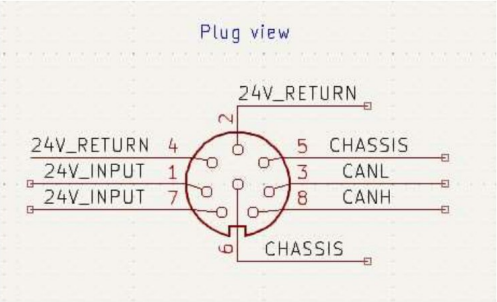

Fig. 44

Fig. 45

Assemble the Lumberg connector using the directions provided by the kit around the newly soldered wires. Electric tape and shrink wrap can be applied to avoid shorts wherever needed. Wrap the exposed wires in the copper shielding, taping both ends to secure them in place, as in Fig. 46.

Fig. 46

Wrap the whole cord in electrical tape as in Fig. 47.

Fig. 47

The power cord is intended to be connected to the battery via banana plugs. The ends of the wires are stripped, and the wires providing 24 V input (red and blue wires) are soldered to the red banana plug. The wires provide 24 V return and the chassis wires are soldered to the black plug as in Fig. 48.

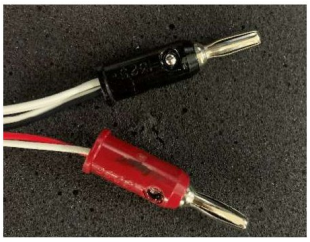

Fig. 48

Wrap more electrical tape around the cord where it fit to prevent shorting. Fig. 49 are the ends of the finished power cord.

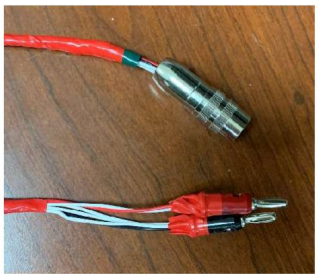

Fig. 49

Solder the two banana plug jacks to the cup connectors as in Fig. 50. These slide into an idea diode board, pictured in Fig. 51.

Fig. 50

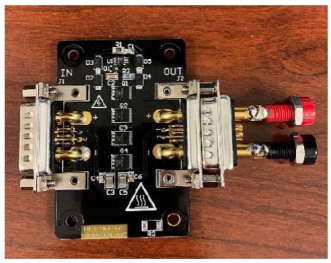

Fig. 51

The ideal diode board is pushed into the battery allocated for the Kinova arm and slid into a battery holder, as in Fig. 52.

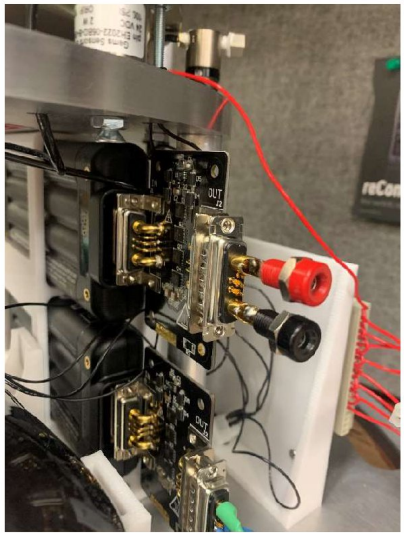

Fig. 52

It is essential to test the cord with a multimeter and voltmeter to ensure the cord works properly before plugging it into the arm.

Step 14:

Acquire the following pieces:

- Relay board
- Jetson Nano
- Left side support
- Jumper cables 30cm –x10
- 20 AWG wire
    - 1.5 cm (red or white) cut—7x
    - 25 cm cut (red) – 4x
    - 10 cm cut (red) – 4x
    - 45 cm cut (red) – 1x
- Heat shrink tubing
- M8 bolts – 2x
- M8 nuts – 2x
- Plastic quick disconnect 2x3 (preferably 1x4 or 2x2) connectors (male & female pair) – 1x
    - crimp metal tips –9x

Start with the 1.5 cm pieces of wire and bend them into an arch as in Fig. 53. The first end arch should be placed in the first screw port on the first relay, skip a single screw port, and then end in the first port of the second relay. Repeat so the relay board looks like Fig. 54. But simply, connect all the first ports of each relay. These ports will all be supplied with a +24V wire from the PSU to power the solenoids.

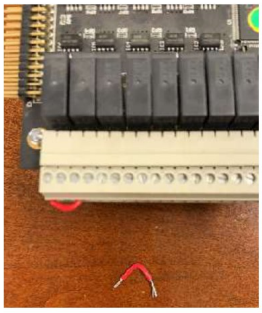

Fig. 53

Fig. 54

Once finished, attached the relay board and jetson nano to the side support with the appropriate hole. Use the small screw standoffs connected to the board corners to put some space between them and the plastic side support. Fig. 55 provides their orientation. *Note: The space in the middle is for the AD/DA conversion board if needed. At this point in the build, the board has not arrived and will be attached at a later date.

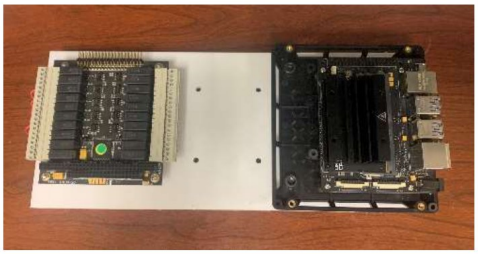

Fig. 55

Line up the side support with the holes provided in the base plate, and use the M8 bolts and nuts to secure the assembly. Fig. 56 displays the side support assembly bolted to the base plate.

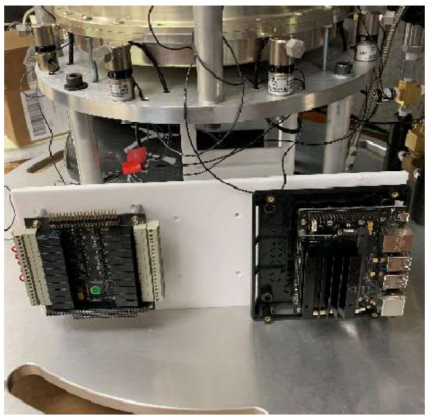

Fig. 56

Acquire the remaining pieces of red wire and strip them ~1cm at one end. Slide a metal crimp wire connector tip on the exposed part, and secure it with heat shrink tubing. Fig. 57 is an example of one such end. Repeat on all remaining wires. Strip 0.5 cm off the other end of all the wires.

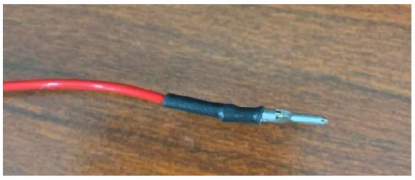

Fig. 57

The metal tips slide and secure themselves into the plastic quick-disconnect connectors. Gather the 25 cm cut wires together and fit them to one side of a quick connector. Do the same with 10 cm wires. Fig. 58 is the result.

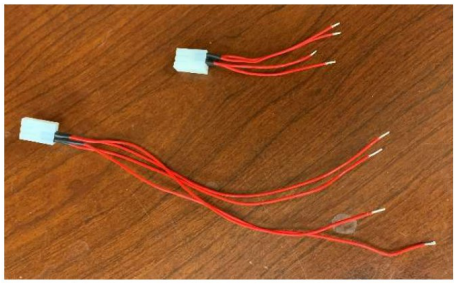

Fig. 58

Fig. 59 is the 45 cm wire. Place the stripped end of the wire into the top slot of the first relay. The other end of this wire will be connected to the +24V slot of the PSU.

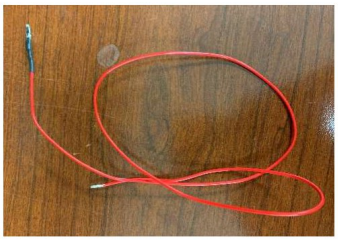

Fig. 59

Spread the remaining stripped ends of the wires into the open slots on the relay's screw terminals. Each wire will coordinate with a separate solenoid. The connector with the shorter wires is used for the solenoids closest to the relay board. Fig. 60 is the finished result.

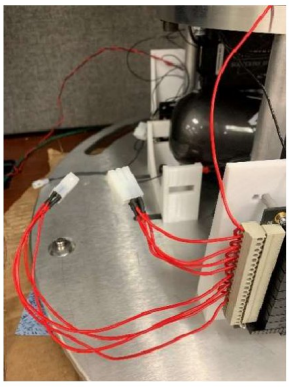

Fig. 60

Attach 8 jumper cables to Pins A2-A9, and two more to B1 & B3 on the J1 connector of the relay. See attached Fig. 61.

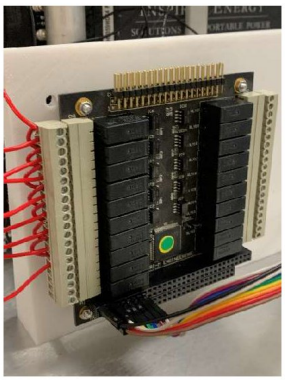

Fig. 61

Attach the other ends of the jumper cables attached to B1 & B3 to pins 4 & 6 of the Jetson Nano. The other eight jumper cables can be tucked away because the GPIO pins have not been assigned yet. See Fig. 62 are the jumpers attached to pins 4&6.

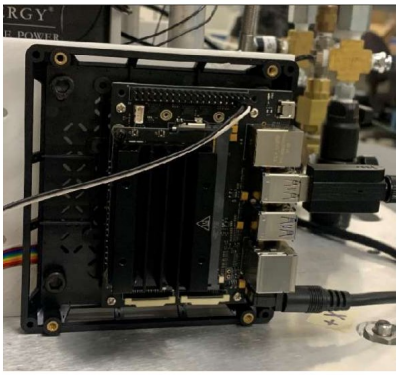

Fig. 62

Step 15:

Acquire the following pieces:

- Power supply unit (PSU)
- Shunt
- DC-DC voltage regulator
- Vive Tracker
- Right side support
- Velcro
- M8 bolts – 2x
- M8 nuts – 2x

Attach the PSU, shunt, and voltage regulator to the side support with screws. Attach the VIVE tracker with Velcro. Fig. 63 is the finished product.

*Note: The PSU unit was later rotated 90 degrees counterclockwise to provide room for the pin connectors that came with the set.

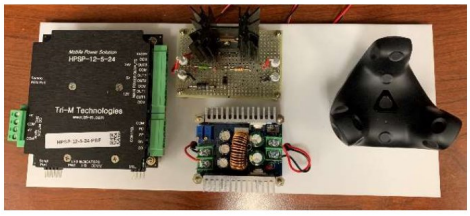

Fig. 63

Line up the side support with the holes provided in the base plate, and use the M8 bolts and nuts to secure the assembly. Fig. 64 displays the side support assembly bolted to the base plate.

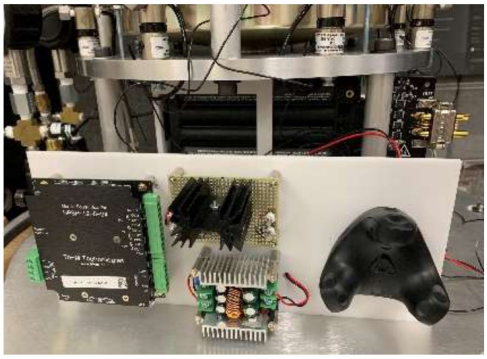

Fig. 64

Step 16:

Acquire the following pieces:

- 20 AWG wire
  - 10 cm cut (black) – 3x
  - 30 cm (black) – 1x
- Plastic quick disconnect 2x3 (preferably 1x4 or 2x2) connectors (male & female pair) – 1x
  - crimp metal tips –10x
- plastic quick disconnect single port (male-female pair) – 1x
- Heat shrink tubing

Gather one wire from each solenoid (it doesn't matter which of the two is already connected) and group them into two groups of four. Strip 1 cm off the ends of the wires, add crimp connectors and then secure into a quick connector. Fig. 65 supplies an example of one of the black-wired connectors. The quick connectors with the black wire from the solenoids snap together with the connectors from the relay board. Test to ensure the connectors line up correctly, but disconnect them when finished.

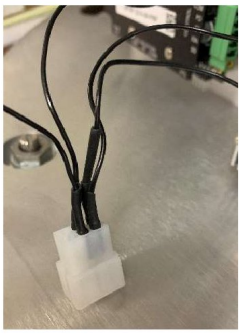

Fig. 65

The other, untouched black wires from the solenoids will be connected to the ground, and have to be consolidated to one wire. One option to accomplish this is to strip the ends of the wires and twist them together in groups of four. Strip 1 cm off all ends of the black AWG wires and connect them all by twisting them together and applying heat shrink tubing. Tape also aids the process. When consolidated to a final wire, attach the female side of the single port plastic quick disconnect. Fig. 66 supplies a picture of the assembly.

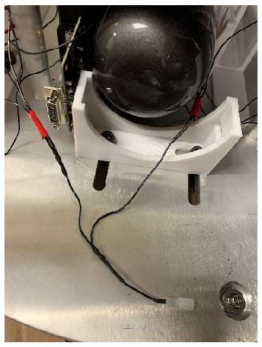

Fig. 66

Acquire the 30 cm black wire and connect a male side of the single port quick connector. The other end is connected to the PSU's "OUT3" which will provide +24V. Fig. 67 displays the black wire connected to the PSU. Test to see that the single port connectors fit together, but then leave disconnected.

Fig. 67

Step 17:

Acquire the following pieces:

- 20 AWG wire
  - 40 cm black – 2x
  - 40 cm red – 2x
- Large solder cup connectors from ideal diode pack – 2x
- Ideal diode – 2x
- DC power jack (for jetson nano)
- Shrink wrap

For the PSU battery connection: strip ends of red and black wire and solder to the respective positive and negative sides of the ideal diode connectors. Apply shrink wrap to the cup terminals to keep wires from shorting. The connector should appear as in Fig. 68.

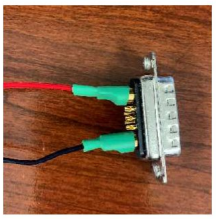

Fig. 68

Screw the other end of the red and black wires into the +V and COM terminals on the DC input connector on the PSU, as in Fig 69.

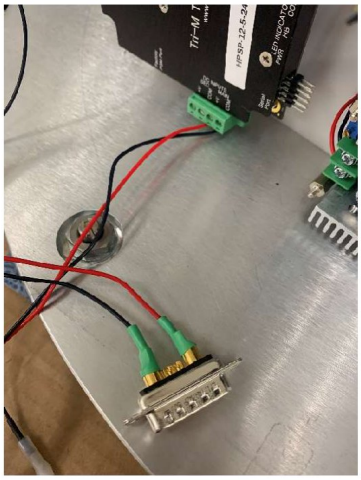

Fig. 69

Push the finished ideal diode connector into the ideal diode board, and push to connect to the PSU's allocated battery. Fig. 70 displays the battery, ideal diode, and wiring for the PSU.

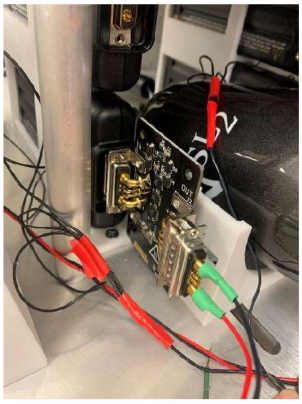

Fig. 70

Repeat the process for the Jetson Nano's allocated battery. Strip the wires and solder to the cup terminals. Take the other end of the red and black wires into the +V and COM terminals on the secondary DC input connector on the PSU. Push the ideal diode connector into the ideal diode, and then push it into the Jetson Nano's battery. Fig. 71 displays the battery with its respective connections.

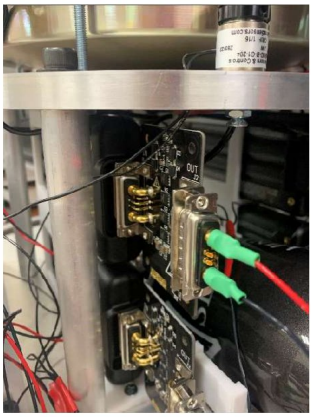

Fig. 71

Find the DC power jack intended for the Jetson Nano, and apply quick disconnect connectors (from the PSU pack) to the exposed end of the wires. Plug the red wire into a +5V OUT terminal, and the black into a COM terminal. The other end of the power cord can remain disconnected for now. Fig. 72 displays the PSU after all wiring is complete.

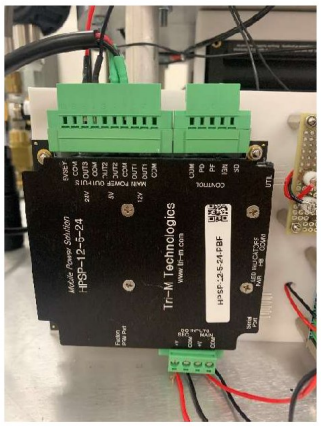

Fig. 72

Step 18:

Acquire the following pieces:

- 20 AWG wire
  - 30 cm green –3x
  - 50 cm red –1x
  - 50 cm black –1x
- Large solder cup connectors from ideal diode pack – 1x
- Ideal diode – x1
- Shrink wrap

Using the battery's terminal diagram in Fig. 73, solder three green wires to cups 2,3, and 4 on the ideal diode connector. When finished, it should appear as in Fig. 74.

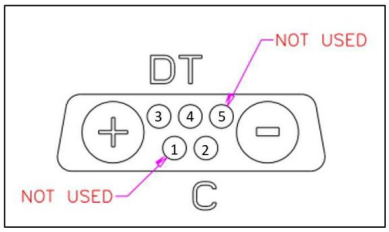

Fig. 73

Fig. 74

Take the red and black wire and screw it into the respective voltage regulator terminals, if not done already. Strip and then solder the other ends of the wire to the large cup terminals. The finished product should appear as in Fig. 75.

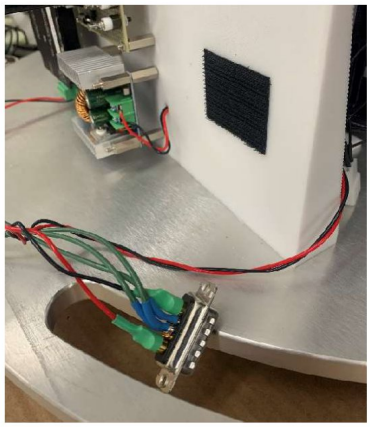

Fig. 75

Plug the finished connector into its ideal diode, and then push the ideal diode into the battery reserved for the reaction wheel. At this point, all wiring for the available parts of the FSS is completed. The installation of the AD/DA board and the signal conditioning board will be integrated at a later date.

Step 19:

Acquire the following pieces:

- M8 bolts – 4x
- M8 nuts – 4x
- Kinova robotic arm

Carefully, place the base of the robotic arm over the FSS's top plate to line up the bolt holes. Use four M8 bolts and nuts to secure the arm in place. I would recommend at least three people to help mount the arm. One to carry the base of the robot, one to prevent the arm from flopping over, and one to line up and bolt the arm's base into place. The base is pictured in Fig. 76.

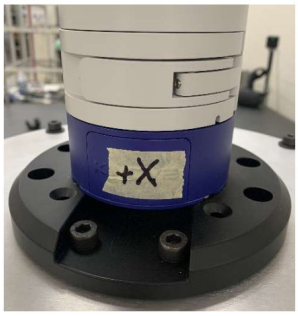

Fig. 76

Once finished, the final design should appear as in Fig. 77.

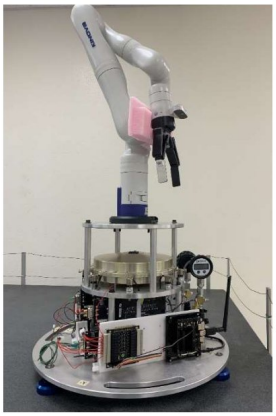

Fig. 77

Step 20:

Make the following final connections:

- Ground connection for solenoids, pictured Fig. 78.
- Power connections for solenoids 1-4, pictured Fig. 79, and solenoids 5-8, pictured Fig. 80.
- Power connection to battery for Kinova Arm, Fig. 81.
- Power connection to the robot base. Fig. 82.
- Jetson Nano power jack, Fig. 83.

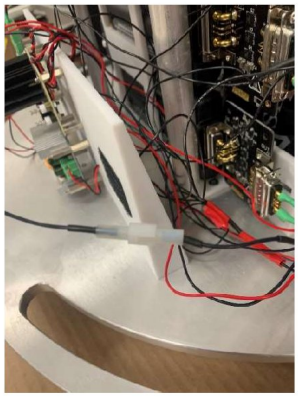

Fig. 78

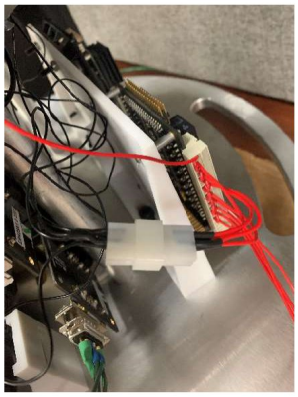

Fig. 79

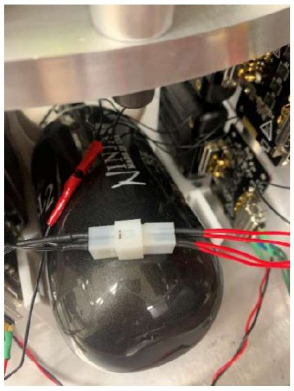

Fig. 80

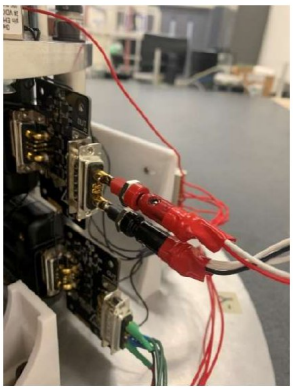

Fig. 81

Fig. 82

Fig. 83

With all connections complete, Fig. 84 pictures the final design.

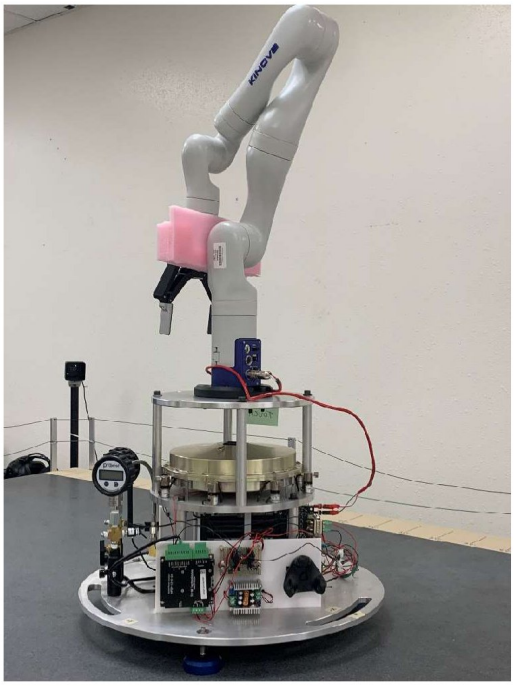

Fig. 84

To operate air bearings:

- Disconnect the empty air tank and fill it with the compressor to a max of 4500 psi.
- Slowly open the panel mount in/out valve to a ninety angle to allow airflow from the air tank to the system. Fig. 85 displays the open valve.
- The air directional control valve is flipped down to open airflow to the air bearings to "turn them on". Fig. 86 displays the open valve.

Fig. 85

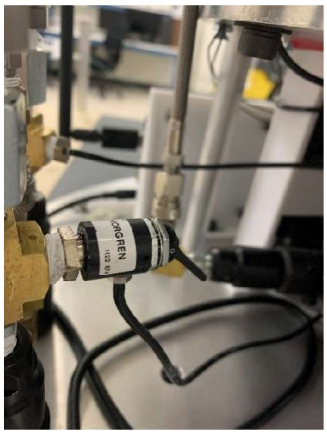

Fig. 86

THIS PAGE INTENTIONALLY LEFT BLANK

List of References

[1] M. Wilde, C. Casey, and M. Romano, "Historical survey of kinematic and dynamic spacecraft simulators for laboratory experimentation of on-orbit proximity maneuvers," *Progess in Aerospace Sciences*, vol. 110, no. 0376, Oct. 2019 [Online]. doi: 10.1016/j.paerosci.2019.100552.

[2] M. Wilde, S. K. Choon, and M. Romano, "Kinematic and dynamic spacecraft maneuver simulators for verification and validation of space robotic systems," in *American Institute of Aeronautics and Astronautics Scitech 2020 Forum*, 2020 [Online]. Available: https://arc.aiaa.org/doi/10.2514/6.2020-1919

[3] M. Wilde, "ORION Spacecraft Robotics Lab at Florida Institute of Technology," FIT, 2018 [Online]. Available: https://community.rti.com/project/orion-spacecraft-robotics-lab-florida-institute-technology

[4] J. Schwartz, M. Peck, and C. Hall, "Historical review of air-bearing spacecraft simulators," *Journal of Guidance, Control, and Dynamics*, vol. 26, no. 4, July 2003 [Online]. doi: https://arc.aiaa.org/doi/10.2514/2.5085.

[5] J. D. J. Virgili-Llop, R. Zappulla and M. Romano, "Laboratory experiments of resident space object capture by a spacecraft–manipulator system," *Aerospace Science and Technology*, vol. 71, no. 530-545, Dec. 2017 [Online]. doi: 10.1016/j.ast.2017.09.043.

[6] H. Lavelle, "Crew readies free-flying robots, prepares sample returns, and transfers cargo," NASA, 2022 [Online]. Available: https://blogs.nasa.gov/spacestation/tag/astrobee/

[7] D. Bolles, "NASA sounding rockets," Dec. 14 2022 [Online]. Available: https://science.nasa.gov/heliophysics/programs/sounding-rockets

[8] European Space Agency, "European Space Agency drop towers," 2018 [Online]. Available: https://www.esa.int/Science_Exploration/Human_and_Robotic_Exploration/Research/Drop_towers

[9] European Space Agency, "European space parabolic flights," 2017 [Online]. Available: https://www.esa.int/Science_Exploration/Human_and_Robotic_Exploration/Research/Parabolic_flights

[10] European Space Agency, "Refreshing the Neutral Buoyancy Facility," Nov. 17, 2022 [Online]. Available: https://www.esa.int/About_Us/EAC/Refreshing_the_Neutral_Buoyancy_Facility

[11] D. Akin, C. Hanner, and N. Bolatto, "Design and development of an EVA assistance roving vehicle for Artemis and beyond," in *50th International Conference on Environmental Systems*, 2021 [Online]. Available: https://ttu-ir.tdl.org/handle/2346/87097

[12] L. Hutchinson, "Swimming with spacemen: training for spacewalks at NASA's giant pool," Mar. 4, 2013 [Online]. Available: https://arstechnica.com/science/2013/03/swimming-with-spacemen/

[13] C. Hall and M. Peck, "Historical review of air-bearing spacecraft simulators," *Journal of Guidance, Control, and Dynamics*, vol. 26, no. 4, July 2003 [Online]. doi: https://doi.org/10.2514/2.5085.

[14] M. Romano and J. Hudson, "Spacecraft robotics lab facilities," Naval Postgraduate School, Apr. 18, 2022 [Online]. Available: https://nps.edu/web/srl/facilities

[15] "JPL's Formation Control Testbed (FCT)," NASA, 2015 [Online]. Available: https://scienceandtechnology.jpl.nasa.gov/formation-control-testbed-fct

[16] UK Research and Innovation: Science and Technology Facilities Council, "Air bearing systems," Mar. 13, 2015 [Online]. Available: https://www.ukspacefacilities.stfc.ac.uk/Pages/University-of-Surrey

[17] "Johnson Space Center: Active Response Gravity Offload System," 2015 [Online]. Available: https://www.nasa.gov/centers/johnson/engineering/integrated_environments/active_response_gravity/

[18] G. L. Cave, "Development and control of robotic arms for the naval postgraduate school planar autonomous docking simulator (NPADS)," M.S. thesis, Dept. of Aeronautics and Astronautics, Monterey, CA, USA, 2002 [Online]. Available: https://apps.dtic.mil/sti/citations/ADA411173

[19] A. Ellery, "Space robotics: part 2: space-based manipulators," *International Journal of Advanced Robotic Systems*, vol. 1, no. 3, Jan. 2004 [Online]. doi:10.5772/5814.

[20] C. Sallaberger, "Canadian space robotic activities," *Acta Astronautica*, vol. 41, no. 4-10, Aug. 1997 [Online]. doi: 10.1016/S0094-5765(98)00082-4.

[21] D. King, "Space servicing: past, present and future," in *Proceeding of the 6th International Symposium on Artificial Intelligence and Robotics Automation in Space*, 2001 [Online]. Available: https://www.academia.edu/33688716/SPACE_SERVICING_PAST_PRESENT_AND_FUTURE

[22] European Space Agency, "ESA's european robotic arm," Accessed Mar. 18, 2023 [Online]. Available: https://www.esa.int/Science_Exploration/Human_and_Robotic_Exploration/International_Space_Station/European_Robotic_Arm

[23] C. Dennehy and J. Carpenter, "A Summary of the rendezvous, proximity operations, docking, and indocking (RPODU) lessons Learned from the Defense Advanced Research Project Agency (DARPA) Orbital Express (OE) demonstration system mission," NASA, Apr 25, 2011.

[24] J. Brill, "OSAM-1 mission: On-orbit Servicing, Assembly, and Manufacturing 1," NASA Goddard NExIS, Mar. 3, 2022 [Online]. Available: https://nexis.gsfc.nasa.gov/OSAM-1.html

[25] V. Lloyd, "NASA's Robotic OSAM-1 mission completes its critical design review," NASAs Goddard Space Flight Center, Dec 14, 2022 [Online]. Available: https://www.nasa.gov/feature/goddard/2022/nasa-s-robotic-osam-1-mission-completes-its-critical-design-review

[26] DARPA Outreach, "Darpa's robotic in-space mechanic aces tests, on track for launch," Nov. 11, 2022 [Online]. Available: https://www.darpa.mil/news-events/2022-11-08#:~:text=RSGS%20is%20intended%20to%20remain,or%20emerging%20challenges%20in%20GEO

[27] S. D. I. Software, *Siemens NX*, NX 1980, Planto, TX, USA, 2021. Available: https://plm.sw.siemens.com/en-US/nx/

[28] A. Caon, B. Francesco, and A. Francesoni, "Development and test of a robotic arm for experiments on close proximity operations," *Acta Astronautica*, vol. 195, pp. 287–294, June 2022.

[29] Inspired Energy, *EB429 ideal diode specification*,DS429 Rev 1.0, 2018 [Online]. Available: https://www.inspired-energy.com/images/product_data_sheets/DS429Rev1.0.pdf

[30] Predictable Designs, "How to pick the right voltage regulator(s) for your design," Accessed Apr. 2, 2023 [Online]. Available: https://predictabledesigns.com/how-to-pick-the-right-voltage-regulators-for-your-design/

[31] Amazon, "ACEIRMC 20A 300W CC CV step down module adjustable DC 6-40V to 1.2-36V voltage regulator buck converter constant current power supply module," Accessed Apr. 2, 2023 [Online]. Available: https://www.amazon.com/Aceirmc-Converter-Adjustable-Regulator-Protection

[32] *Reaction wheel interface control drawing*, 1st ed., Ball Aerospace., Boulder, CA, USA, 2000, pp. 1–9.

[33] Waveshare, *High-precision AD/DA board*, 2015 [Online]. Available: https://www.waveshare.com/wiki/High-Precision_AD/DA_Board

[34] New Way, "65mm flat round air bearing," Jan. 14, 2019 [Online]. Available: https://www.newwayairbearings.com/catalog/product/65mm-flat-round-air-bearings/

[35] ProSense, "ProSense DPG1 digital pressure gauge," Mar. 6, 2020 [Online]. Available: https://www.automationdirect.com/adc/overview/catalog/pneumatic-components/pneumatic-pressure-gauges/digital-pressure-gauges

[36] D. Systèmes, *Magic System of Systems Architect*, 3.0, Vélizy-Villacoublay, FR, 2021. Available: https://www.3ds.com/products-services/catia/products/catia-magic/magic-systems-of-systems-architect/

[37] Seeed Studio, "NVIDIA reComputer Jetson-10-1-H0." Available: https://files.seeedstudio.com/wiki/reComputer-Jetson-Nano/reComputer-Jetson-10-1-H0-datasheet.pdf

[38] Inspired Energy, *PH2059HD34 rechargeable smart lithium ion battery pack specification*, DSPH2059HD34, 2022 [Online]. Available: https://www.inspired-energy.com/images/product_data_sheets/PH2059HD34_spec_v3.0.pdf

[39] Tri-M Technologies, *HPS3512 manual*, HPS3512 V3-MAN, 2009 [Online]. Available: https://www.tri-m.com/products/trim/files/manual/hps3512_man.pdf

[40] Tri-M Technologies, *R104-V4 user guide*, IR104-V4, 2009 [Online]. Available: https://www.tri-m.com/products/trim/files/manual/ir104_man.pdf

[41] HTC Corporation, "*HTC VIVE tracker (2018) developer guidelines ver. 1.0*, vive-trackerv3, 2018 [online]." Available: https://dl.vive.com/Tracker/Guideline/HTC_Vive_Tracker(2018)_Developer+Guidelines_v1.0.pdf

[42] Geekworm, "Geekworm NVIDIA Jetson Nano dual band wireless USB 3.0 WiFi adapter 5GHz+2.4GHz 1200M." Available: https://geekworm.com/products/geekworm-nvidia-jetson-nano-dual-band-wireless-usb-3-0-adapter-5ghz-2-4ghz-1200m

[43] M. Tungett, "Dynamic modeling and simulation of a floating spacecraft simulator utilizing a Kinova 7DoF robotic arm," unpublished.

[44] Kinova, "Discover the possibilities: Gen3 ultra lightweight robot," Jan. 25, 2022 [Online]. Available: https://www.kinovarobotics.com/product/gen3-robots

[45] Kinova, "*KINOVA Gen3 ultra lightweight robot 7 DoF spherical technical specifications*,r07, 2022 [online]." Available: https://www.kinovarobotics.com/uploads/User-Guide-Gen3-R07.pdf

[46] Ninja Paintball, "Ninja ultralite adjustable tank regulator - 4500 psi," Sep. 25, 2018 [Online]. Available: https://www.ninjapaintball.com/regulators

[47] Palmers Pursuit Shop, "Fatty stabilizer co2 air pneumatic regulator up to 4500 psi input adjustable 0-400 psi output," May. 4, 2017 [Online]. Available: https://palmerspursuit.com/products/fatty-stabilizer-finish-nickel

[48] Gem Sensors, "Solenoid valves e series – subminiature gas," Feb. 25, 2021 [Online]. Available: www.GemSenors.com

[49] C. Lugini, "Thrust system for laboratory spacecraft simulators of autonomous docking," Naval Postgraduate School, Sapienza Universita di Roma, 2007.

[50] Dassault Systems, "3d printing - addative process," Aug. 13, 2018 [Online]. Available: https://make.3dexperience.3ds.com/processes/powder-bed-fusion

[51] J. Charras, *KiCad*, ver. 7.0, Davis, CA, USA, 2023. Available: https://www.kicad.org/

[52] KiCad, "KiCad EDA: A cross platform and open source electronics design automation suite," 2022. Available: https://www.kicad.org/

[53] Seeed Studio, "GPIO and grove for reComputer Jetson," 2020. Available: https://wiki.seeedstudio.com/reComputer_Jetson_Series_GPIO_Grove/

[54] Cisco Press, "CCNA: network media types," 2023. Available: https://www.ciscopress.com/articles/article.asp?p=31276

THIS PAGE INTENTIONALLY LEFT BLANK

Initial Distribution List

1. Dudley Knox Library
   Naval Postgraduate School
   Monterey, California

2. Defense Technical Information Center
   Ft. Belvoir, Virginia